DEFENCE S&T TECHNICAL BULLETIN

VOL. 14 NUM. 2 YEAR 2021 ISSN 1985-6571

CONTENTS

Ministry of Defence
Malaysia

SCIENCE & TECHNOLOGY RESEARCH INSTITUTE FOR DEFENCE (STRIDE)

AIMS AND SCOPE

The Defence S&T Technical Bulletin is the official journal of the Science & Technology Research Institute for Defence (STRIDE). The journal, which is indexed in, among others, Scopus, Index Corpenicus, ProQuest and EBSCO, contains manuscripts on research findings in various fields of defence science & technology. The primary purpose of this journal is to act as a channel for the publication of defence-based research work undertaken by researchers both within and outside the country.

WRITING FOR THE DEFENCE S&T TECHNICAL BULLETIN

Contributions to the journal should be based on original research in areas related to defence science & technology. All contributions should be in English.

PUBLICATION

The editors' decision with regard to publication of any item is final. A manuscript is accepted on the understanding that it is an original piece of work that has not been accepted for publication elsewhere.

PRESENTATION OF MANUSCRIPTS

The format of the manuscript is as follows:

a) Page size A4
b) MS Word format
c) Single space
d) Justified
e) In Times New Roman, 11-point font
f) Should not exceed 20 pages, including references
g) Texts in charts and tables should be in 10-point font.

Please e-mail the manuscript to:

1) Gs. Dr. Dinesh Sathyamoorthy (dinesh.sathyamoorthy@stride.gov.my)
2) Dr. Mahdi bin Che Isa (mahdi.cheisa@stride.gov.my)

The next edition of the journal (Vol. 15, Num. 1) is expected to be published in April 2022. The due date for submissions is 12 January 2022. **It is strongly iterated that authors are solely responsible for taking the necessary steps to ensure that the submitted manuscripts do not contain confidential or sensitive material.**

The template of the manuscript is as follows:

TITLE OF MANUSCRIPT

Name(s) of author(s)

Affiliation(s)

Email:

ABSTRACT

Contents of abstract.

Keywords: *Keyword 1; keyword 2; keyword 3; keyword 4; keyword 5.*

1. TOPIC 1

Paragraph 1.

Paragraph 2.

1.1 Sub Topic 1

Paragraph 1.

Paragraph 2.

2. TOPIC 2

Paragraph 1.

Paragraph 2.

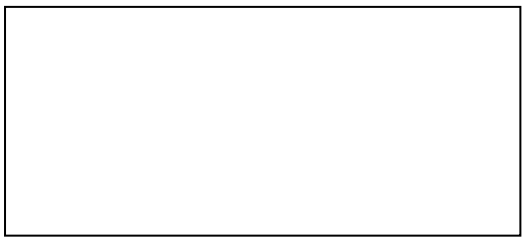

Figure 1: Title of figure.

Table 1: Title of table.

Content	Content	Content
Content	Content	Content
Content	Content	Content
Content	Content	Content

Equation 1 (1)
Equation 2 (2)

REFERENCES

Long lists of notes of bibliographical references are generally not required. The method of citing references in the text is 'name date' style, e.g. 'Hanis (1993) claimed that...', or '…including the lack of interoperability (Bohara *et al.*, 2003)'. End references should be in alphabetical order. The following reference style is to be adhered to:

Books

Serra, J. (1982). *Image Analysis and Mathematical Morphology*. Academic Press, London.

Book Chapters

Goodchild, M.F. & Quattrochi, D.A. (1997). Scale, multiscaling, remote sensing and GIS. *In* Quattrochi, D.A. & Goodchild, M.F. (Eds.), *Scale in Remote Sensing and GIS*. Lewis Publishers, Boca Raton, Florida, pp. 1-11.

Journals / Serials

Jang, B.K. & Chin, R.T. (1990). Analysis of thinning algorithms using mathematical morphology. *IEEE T. Pattern Anal.*, **12**: 541-550.

Online Sources

GTOPO30 (1996). *GTOPO30: Global 30 Arc Second Elevation Data Set*. Available online at: http://edcwww.cr.usgs.gov/landdaac/gtopo30/gtopo30.html (Last access date: 1 June 2009).

Unpublished Materials (e.g. theses, reports and documents)

Wood, J. (1996). *The Geomorphological Characterization of Digital Elevation Models*. PhD Thesis, Department of Geography, University of Leicester, Leicester.

VIBRATION ANALYSIS OF FLEXIBLE COUPLING FOR ENGINE AND GEARBOX OF NAVAL SHIP PROPULSION SYSTEM

Yogeswaran Sinnasamy*, Noor Aishah Sa'at & Khairul Anuar Ahmad

Science & Technology Research Institute for Defence (STRIDE), Ministry of Defence, Malaysia

*Email: yoges.sinnasamy@stride.gov.my

ABSTRACT

In reciprocating-rotating machines, flexible couplings are widely used in many applications, such as diesel engines and gearboxes. Vibration monitoring is highly capable of detecting any abnormalities in flexible couplings before failure occurs. In this paper, vibration measurement was performed at sea on the flexible coupling for a marine diesel engine and gearbox to predict the vibration spectra at various motor speeds and running hours. The vibration spectra captured for both the engine and gearbox at various speeds were analysed based on different running hours, with the measurements found to have high level of accuracy. Based on the procedure developed in this experimental work, condition monitoring (CM) for flexible couplings for marine diesel engine and gearbox systems can be developed in the future.

Keywords: *Flexible coupling; diesel engine; gearbox; vibration spectra; motor speed.*

1. INTRODUCTION

Couplings are machine parts that perform the connection between two consecutive elements of a kinematic chain. The coupling element transmits the torque between rigid coupling components that are situated concentrically one inside the other. Couplings are widely used in naval and merchant ships to support main and auxiliary propulsion systems. In rotating machineries, these couplings are subject to unbalanced forces generated in machines (Mihaela & Silviu, 2014).

Vibration is one of the most common parameters that are used for monitoring the health condition of equipment and certain types of machineries based on movement of associated components and supporting bases as per operational requirements. Condition monitoring (CM) of bearing faults is typically implemented using experimental based vibration analysis data (Desavale *et al.*, 2013; Vishwakarma *et al*., 2017; Malla & Panigrahi, 2019). Vishwakarma *et al*. (2017) and Malla & Panigrahi (2019) demonstrated the various types of common rotating machinery faults that can be detected using vibration analysis.

CM is defined as the continuous evaluation of the health of a plant and its equipment throughout its service life. It is important to be able to detect faults while they are still developing. This is called incipient failure detection (Li *et al*., 2012; Elamin, 2013; Shi *et al*., 2020). Meanwhile, failure is the termination of the ability to perform the required function, and fault is defined as a situation that exists after a failure (Elamin *et al*., 2010). Incipient detection of diesel engine failures provides a safe operating environment and thus, it is becoming increasingly important to use comprehensive CM schemes for continuous assessment of the combustion and mechanical conditions of reciprocating machineries (Gu *et al*., 2006).

Coupling is a power transmission device that transmits mechanical power from the driver to driven equipment. Coupling transmits power, accommodates misalignment, compensates end float, dampens vibration, gives overload protection, insulates driver-driven units and tunes a system out of a torsional critical mode. A flexible coupling subjected to torque, misalignment and speed reacts on the

connected equipment (Sweta & Tuljapure, 2015). The coupling element transmits the torque between rigid coupling components that are situated concentrically one inside the other. Couplings are widely used in naval and merchant ships to support main and auxiliary propulsion systems. In rotating machineries, these couplings are subject to unbalanced forces generated in machines (Mihaela & Silviu, 2014).

According to Sweta & Tuljapure (2015), one of the most common problems encountered in flexible coupling operation is caused by excessive radial and axial vibration. It is primarily caused by resonance, which occurs when the excitation frequencies are equivalent to the system's natural frequencies. Improper installation including poor alignment is another cause of vibration problem. For example, whenever a gasket that prevents oil leaking inside the coupling is dislocated from the original location, this will force leaking of lubricant oil that is basically for the purpose of reducing higher friction inside the coupling. In fact, knocking sounds and wobbling coming from coupling are some of indications showing that the coupling needs to be overhauled (Sinnasamy *et al.*, 2020).

In this paper, vibration measurement is performed at sea on the flexible couple for a marine diesel engine and gearbox to predict the vibration spectra at various motor speeds and running hours. It is expected that the findings of this study will allow for a CM procedure to be developed for flexible couplings for marine diesel engine and gearbox systems.

2. LITERATURE REVIEW

Due to the high speed of some rotating machinery, such as ship propulsion systems, the need for a better understanding of the vibration phenomena is becoming a necessity for practical engineers for the purpose of troubleshooting. Most rotating equipment consists of a driver and driven machine coupled through a mechanical coupling. The mechanical coupling is used mainly to transmit torque from the driver to the driven machine. Due to current trends in the design of rotating machinery towards higher speeds and lower vibration, manufacturers are tending to produce machines that operate closer to lateral critical speeds than has previously been necessary (Pallavi, 2014).

Consequently, the effect of coupling upon higher speeds and misalignment on vibration amplitudes of such machines is becoming an increasingly important consideration for rotor-bearing systems. The vibration in rotating machinery is mostly caused by unbalance, misalignment, mechanical looseness and other malfunctions (Salem *et al*., 2012). However, the perfect alignment between the driving and driven machines cannot be attained in the real world. In order to ensure that the rotor of a piece of rotating machinery is sufficiently designed to withstand the stresses and strains of the operating environment, the coupling chosen to join the driving and driven mechanisms must be properly selected. Operating the ship outside the critical speed or resonance zone would eventually play an important factor in safeguarding ship and crew safety. In addition to transmitting torque from the driver to the driven pieces of machinery, the coupling must also compensate for all possible unintentional vibrations apart from misalignment of the rotating devices (Sweta & Tuljapure, 2015).

Other machineries of the propulsion system, such as gearbox, plummer block, shaft bearing and stern tube, would be affected as well due to transmission of vibration from the engine along the shafting line. Besides these machineries, flexible coupling, which connects the diesel engine and gearbox, will be affected as well. Some of the internal components of the flexible coupling, such as oil ring, experience wear and tear symptoms and end up with dislocation from the original grove or position. Indirectly, this critical speed and subsequent scenario makes the oil inside the coupling leak out slowly, and eventually events such as wobbling and knocking sounds start to appear during engine operation. The detection and prevention of critical speed at an early stage could save the ship propulsion system from catastrophic failure, especially the flexible coupling. After the coupling is installed in the diesel shaft, the characteristics of the rubber parts of the coupling will be affected due to high temperature under operation, aging and alternating torque, which can even lead to severe damage. As shown in Figure 1, oil leaking marks that come out from the internal portion of the elastic

coupling due to erosion and microcracks occur on the surface of the rubber component of an elastic coupling, which will cause the coupling torsional stiffness to change inevitably (Li *et al*., 2016).

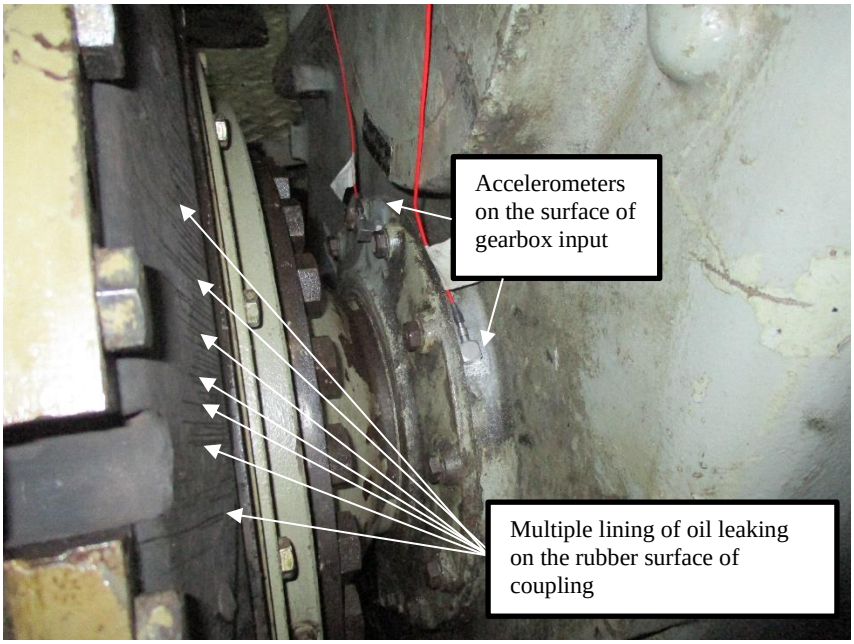

Figure 1: Flexible coupling on a Royal Malaysian Navy (RMN) ship.

Shamin & Pallavi (2014) developed a theoretical model of a complete motor flexible-coupling-rotor system using component mode synthesis. A general system of equation of motion was derived for a system under misalignment and unbalanced condition. The derived equations indicated that the forcing frequency due to shaft misalignment were even multiple frequencies of the motor rotational speed. They extended the experimental investigation of unbalance using a fast Fourier transform (FFT) analyser and its unique vibration spectrum for different types of couplings, such as jaw, flexible flange and rigid couplings. They reported that unbalance related faults showed dominant peak at 1×. For experimental identification of unbalance, an experimental setup was constructed and frequency spectrums were acquired for the couplings. The experimental results were found to be in close agreement with results available in the literature.

3. METHODOLOGY

3.1 Measurement Locations

A sketch of the flexible coupling was initially developed to represent the actual system. It consists of two masses and a shaft that is fixed at its end, as illustrated in Figure 2. The figure shows the measurement locations and directions on a 2D sketch of the ship's power transmission system. In this system, the main diesel engine and gearbox is connected by a rotating shaft. There were five measurement locations, consisting of: two accelerometers on the main diesel engine that were mounted at two different directions, axial and vertical; as well as three accelerometers on the input of that gearbox that were mounted at three different directions, axial, horizontal and vertical. Fibre optic measurement cables with length of 30 m were used in this measurement.

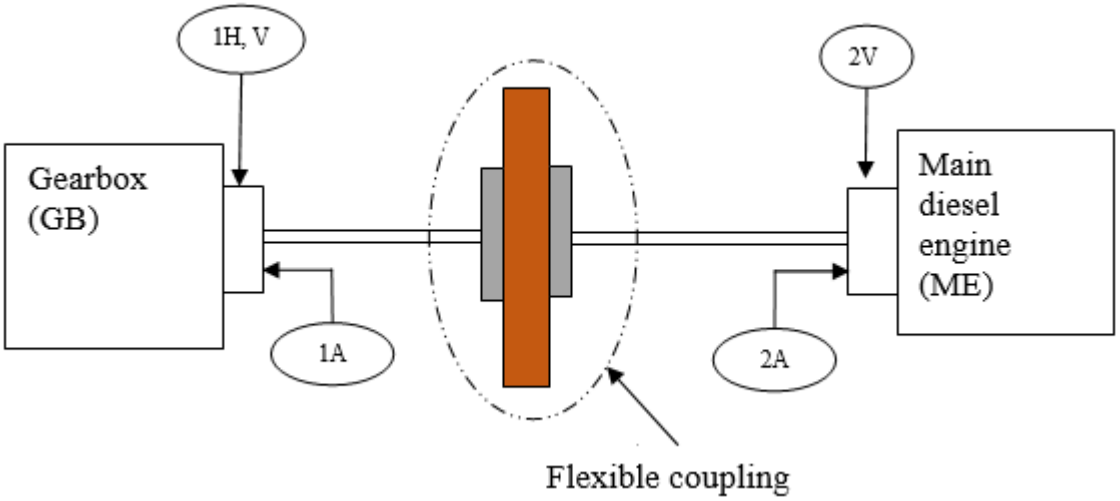

Figure 2: The five measurement points determined on the actual physical system.

In total, two measurement points at its three-dimensional axes were determined, as illustrated in Figure 2, where the measurement points are labelled as 1 and 2, in which the letters *A*, *H* and *V* represent axial, horizontal and vertical axes respectively. Detailed descriptions of each measurement points are as follows:

a) 1*A* : Axial measurement point towards the direction of the *x*-axis
b) 1*H* : Horizontal measurement point towards the direction of the *y*-axis
c) 1*V* : Vertical measurement point towards the direction of the *z*-axis
d) 2*A* : Axial measurement point towards the direction of the *x*-axis
e) 2*V* : Vertical measurement point towards the direction of the *z*-axis

3.2 Measurement Procedure

Figure 3 shows the locations of the accelerometers, and their directions on the marine diesel engine and gearbox. Between these two parts of the rotor dynamic system, there is a unit of flexible coupling. First, the rotor dynamic is run for a few minutes to settle down all minor vibrations. The shaft is visually checked for any misalignment and unbalance. The two-dial gauge method is used to check for proper alignment and balancing.

Figures 3 also show photos that were captured during accelerometer mounting and cable lay. All the accelerometers were installed using super glue as it was too easy to remove and suitable for this kind of measurement. This technique was used for temporary installation because the engine and gearbox surfaces are not adequately prepared for stud mounting.

A temporary work station was set up outside the engine room, as shown in Figure 4. This work station consisted of a Toughbook (for data recording and analysis) and SCADAS (for data acquisition). Normally two to three days are needed to set up the whole temporary work station, which could be conducted while ship is harboured at jetty. Once the set up was completed, the measurement at sea was conducted.

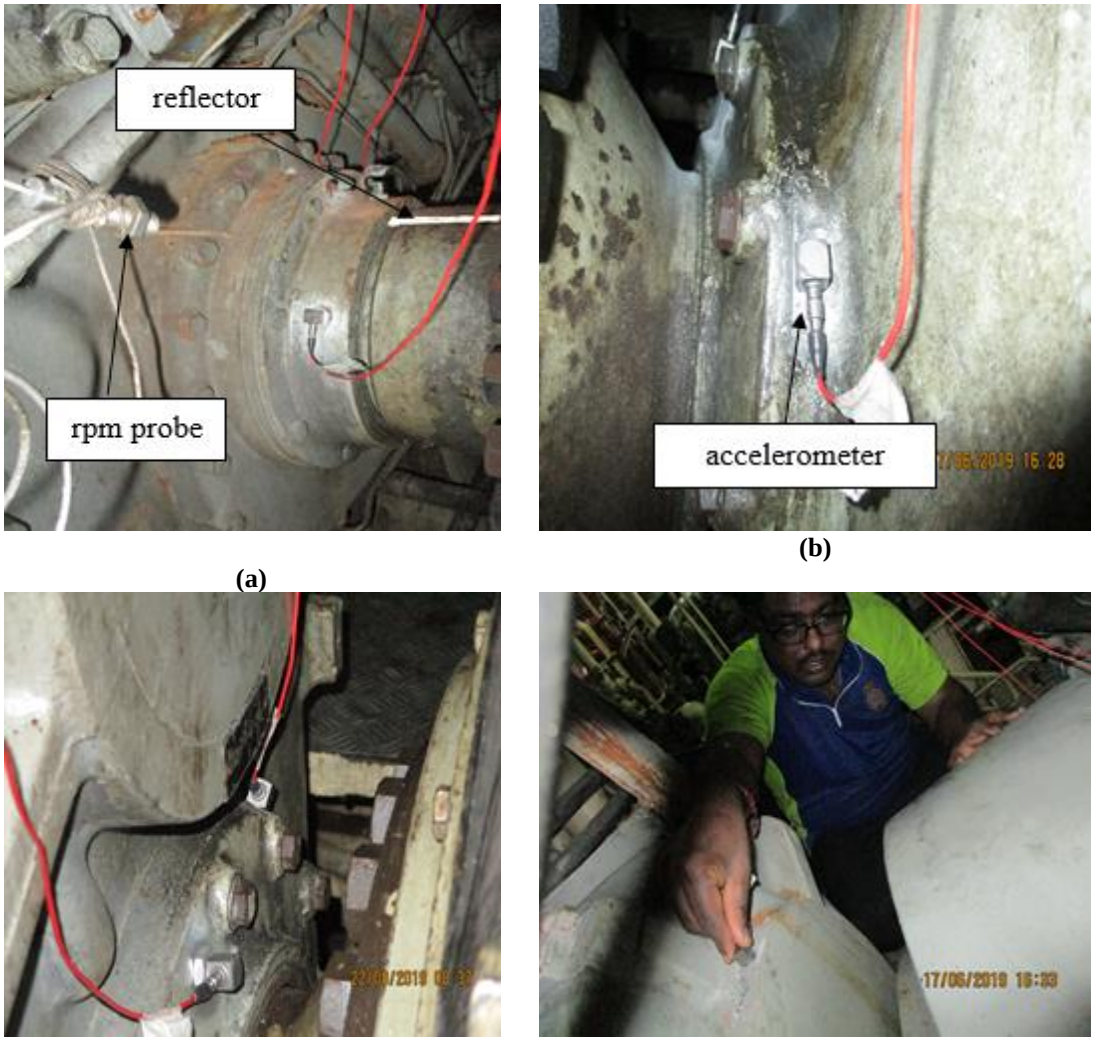

(a) **(b)**

(c) **(d)**

Figure 3: Sensor mounting and cable lay out in progress.

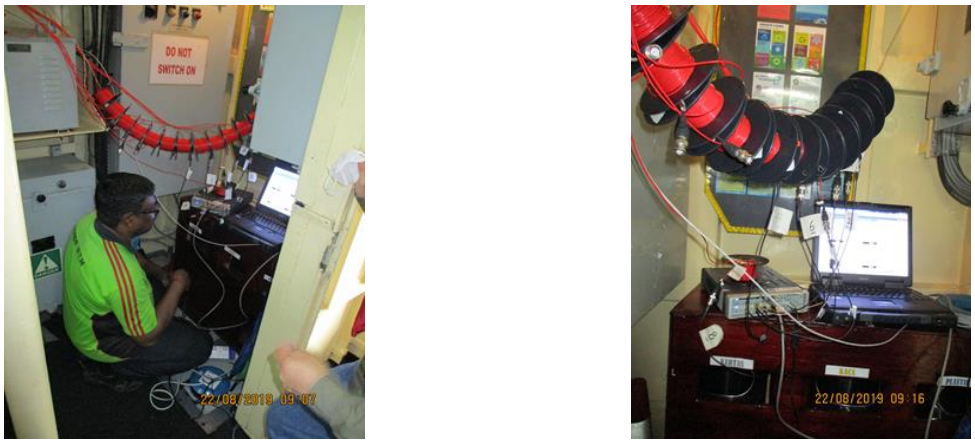

(a) **(b)**

Figure 4: Setting up temporarily workstation.

The measurements were performed for the well-balanced rotor systems at both the drive end (DE) of the engine and housing of the gearbox, with vibration signals recorded for seven revolutions (engine revolutions in rpm). The measurement was started at 500 rpm, which is considered as the minimum engine revolution. At this speed, the vibration data was recorded for at least 10 min, which consisted of three runs. Once the measurement at minimum speed was completed, the engine revolution was increased to 700 rpm. Once again, the vibration data at this speed was recorded for at least 10 min and three runs as previously. This step was repeated at 900, 1,100, 1,300 and subsequently until engine revolution reached 1,700 rpm. During the vibration measurement, rpm was also recorded using a rpm probe that was connected to the SCADAS, as shown in Figure 3(a).

Table 1 shows the running rpm and fundamental frequencies that were obtained by dividing the rpm values by 60 min, as shown in the following equation:

$$fundamental\ frequency, f = \frac{shaft\ rpm}{60} \quad (1)$$

Table 1: Calculated fundamental frequencies using Equation 1.

Shaft speed (rpm)	Calculated fundamental frequency (Hz)
500.0	8.33
700.0	11.67
900.0	15.00
1100.0	18.33
1300.0	21.67
1500.0	25.00
1700.0	28.33

Table 2 shows the measurement matrix for this study, which covers five different running hours. The list of different running hours also included running hours just after minor and first top overhauls, which was the routine maintenance of engine instructed by original equipment manufacturer (OEM) of the engine. At each running hour, vibration measurement was conducted at seven different engine revolutions, starting from the minimum revolution until it reached maximum, which could be considered as high-speed level rotation.

Table 2: Measurement matrix.

Engine revolution (rpm)	Running hours (hour: minute)				
	2,305:09	**3,506:11**	**4,453:45**	**5,885:56**	**6,764:34**
500	*Section 1* - Runs 1, 2, 3	*Section 2* - Runs 1, 2, 3	*Section 3* - Runs 1, 2, 3	*Section 4* - Runs 1, 2, 3	*Section 5* - Runs 1, 2, 3
700	*Section 1* - Runs 4, 5, 6	*Section 2* - Runs 4, 5, 6	*Section 3* - Runs 4, 5, 6	*Section 4* - Runs 4, 5, 6	*Section 5* - Runs 4, 5, 6
900	*Section 1* - Runs 7, 8, 9	*Section 2* - Runs 7, 8, 9	*Section 3* - Runs 7, 8, 9	*Section 4* - Runs 7, 8, 9	*Section 5* - Runs 7, 8, 9
1100	*Section 1* - Runs 10, 11, 12	*Section 2* - Runs 10, 11, 12	*Section 3* - Runs 10, 11, 12	*Section 4* - Runs 10, 11, 12	*Section 5* - Runs 10, 11, 12
1300	*Section 1* - Runs 13, 14, 15	*Section 2* - Runs 13, 14, 15	*Section 3* - Runs 13, 14, 15	*Section 4* - Runs 13, 14, 15	*Section 5* - Runs 13, 14, 15
1500	*Section 1* - Runs 16, 17, 18	*Section 2*- Runs 16, 17, 18	*Section 3* - Runs 16, 17, 18	*Section 4* - Runs 16, 17, 18	*Section 5* - Runs 16, 17, 18
1700	*Section 1* - Runs 19, 20, 21	*Section 2* - Runs 19, 20, 21	*Section 3* - Runs 19, 20, 21	*Section 4* - Runs 19, 20, 21	*Section 5* – Runs 19, 20, 21

4. RESULTS AND DISCUSSION

Figure 5(a) shows the vibration spectrum in frequency domain for up to 6,400 Hz. The spectrum is zoomed to a smaller scale as shown in Figure 5(b). The next step is the identification process of the amplitude values at the fundamental or running frequencies at the five different locations. For example, Figure 6 was recorded at revolution of 1,100 rpm and 4,453:45 running hours. The fundamental frequency is 19.38 Hz and acceleration are 0.0691 m/s^2 by referring to the intersection point on the *y*-axis. By utilising this method, other amplitude values at various revolutions and running hours were obtained to form vibration trends shown in Figures 7-11. Each pattern in the figure shows the trending of vibration amplitude at different running hours, including the one after top overhaul.

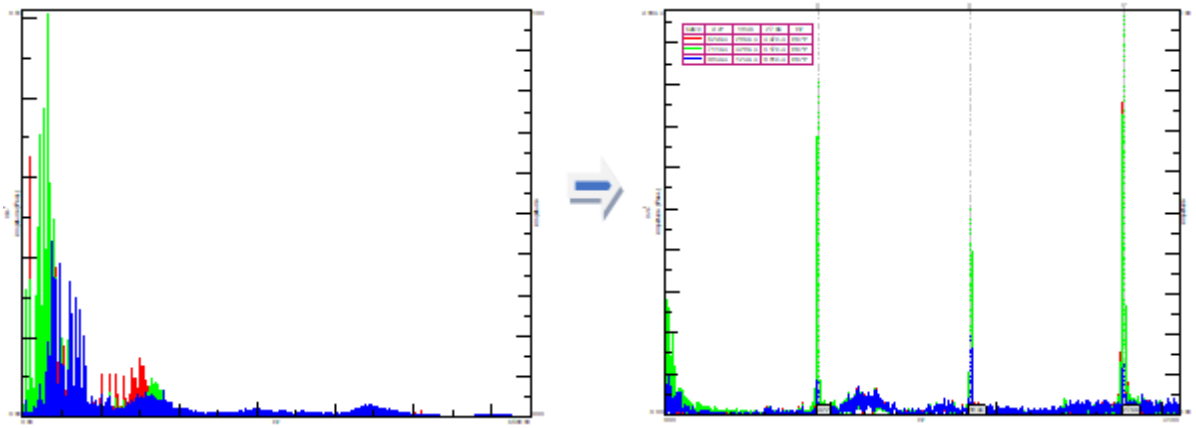

Figure 5: (a) Vibration spectrum in the frequency domain. (b) Enlarged view of the frequency spectrum.

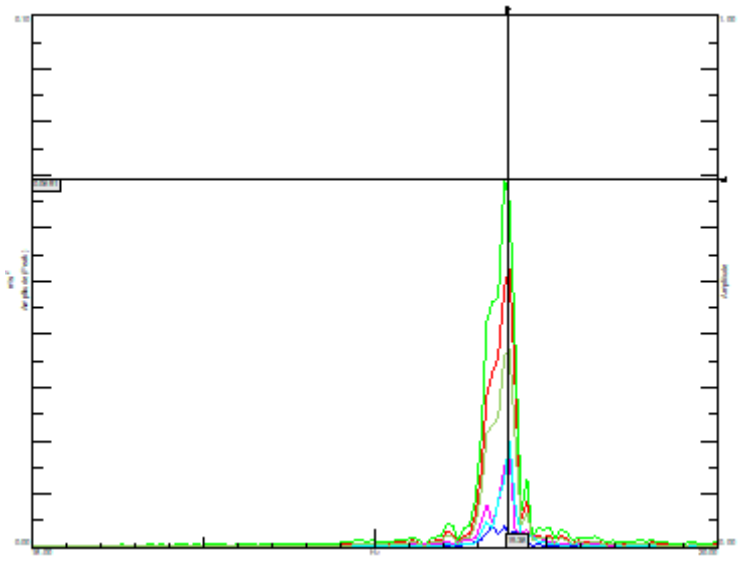

“ ”	Location 1	“ ”	Location 3	“ ”	Location 5
“ ”	Location 2	“ ”	Location 4		

Figure 6: Identifying vibration amplitudes at different locations for revolution of 1,100 rpm and 4,453:45 running hours.

Figure 6 shows the vibration amplitudes at Location 1, which was on the surface of driving end of the engine in the vertical direction at different engine revolutions. Based on this figure, it is found that the vibration amplitudes increased from the minimum revolution until it reached the maximum revolution. This pattern of vibration trending is almost similar for all conditions of running hours.

In addition, based on the vibration trending pattern for Location 1, we observed that whenever the running hours increased, the vibration amplitudes also increased consistently, except during 2,305:09 and 3,506:11 running hours. It showed that lower increment of running hours contributed to less effect on vibration amplitude changes due to mild existence of misalignment condition. Meanwhile, at this location, the highest value of vibration amplitude was 40.10 m/s^2. Basically, the engine running hours starts from zero once the engine has completed major overhaul for every 12,000 running hours. This maintenance practice is based on the engine's periodic maintenance manual. From our experimental study, due to unavailability of the ship, we could not start vibration measurement at approximately 1,000 or less than 2,000 running hours. We could only start our first measurement at 2,305:09 running hours. At this early stage, we assumed that the alignment of the shafting line was still within the acceptable condition.

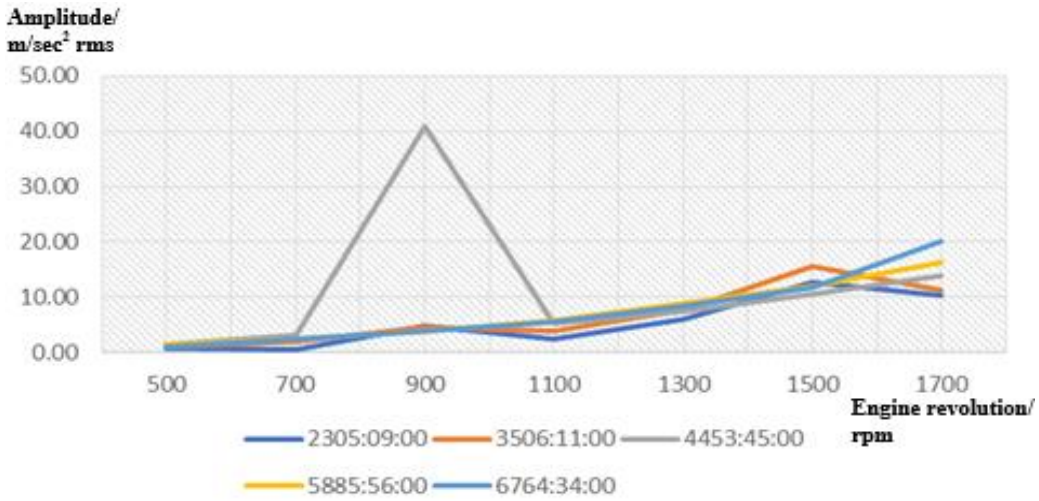

Figure 7: Comparison of measured vibration amplitudes at Location 1.

Figure 8 shows the vibration amplitudes at Location 2, which was on the surface of the driving end of the engine in the axial direction. Almost a similar trending pattern as per Location 1 was observed at Location 2, even though both were measured in different directions. This similarity shows that the locations of measurement that are very close to each other do not contribute to any major changes in the vibration trending. These can be observed based on the amplitudes measured at different revolutions and running hours in this study. In terms of highest value of vibration amplitude at Location 2, it was found that the highest value was 0.26 m/s^2 which was recorded during 6,764:34 running hours at 1,700 rpm. This value is considered to be very low in comparison with the value found at Location 1. This shows that the vibration in the vertical direction, which was Location 1, was obviously very high in comparison with the axial direction, which was Location 2 for the diesel engine.

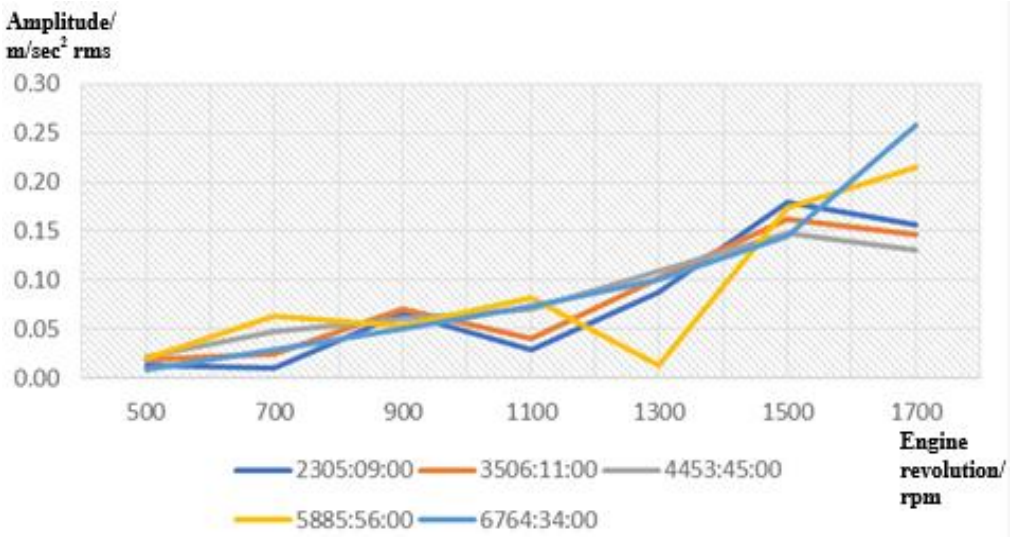

Figure 8: Comparison of measured vibration amplitudes at Location 2.

Figures 9 - 11 show the trending of vibration amplitudes at Locations 3 - 5 on the gearbox housing, which was near the input bearing. In comparison with Figures 7 and 8, these three figures show obvious differences in terms of measured vibration amplitudes and their trending with different engine revolutions.

Figure 9 shows the vibration amplitudes at Location 3, which was located on the surface of the gearbox housing in the vertical direction. This is considered as the driven side of the flexible coupling. Based on this figure, lower range of vibration was found trending at revolutions between 500 and 1,100 rpm at all levels of running hours.

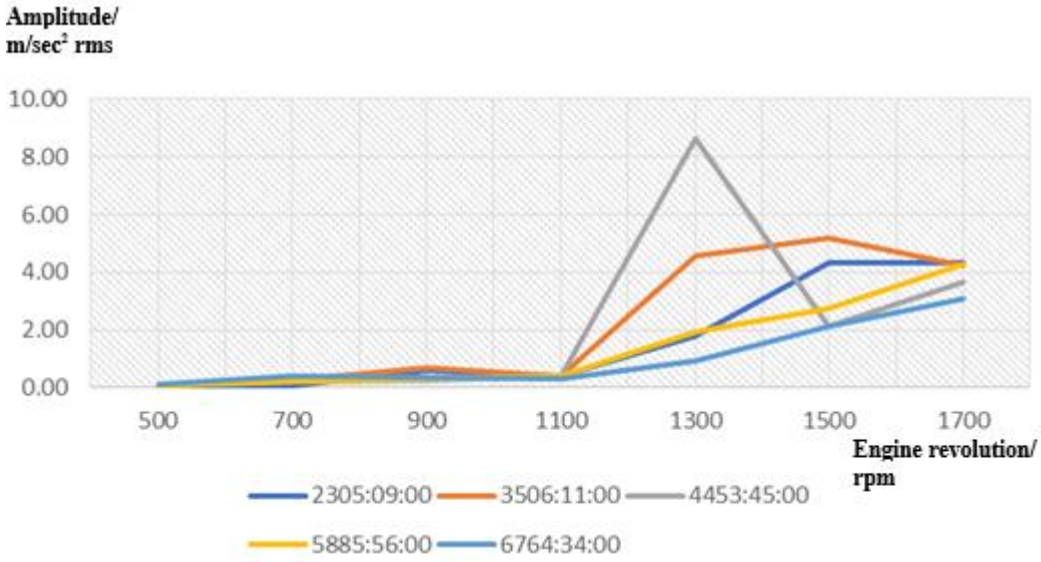

Figure 9: Comparison of measured vibration amplitudes at Location 3.

As shown in the figure, at revolutions of 1,300 rpm and above, inconsistent conditions were observed in terms of vibration trending. The highest value found for this location was 8.50 m/s^2, which was recorded during 4,453:45 running hours at 1,300 rpm. This value suddenly dropped to a lower amplitude value once the revolution increased to 1,500 rpm. This abnormal condition could be due to the existence of critical speed or resonance of the rotor dynamic system. An almost similar condition was observed at running hour of 3,506:11, but the measured amplitude was slightly lower than at running hour of 4,453:45 once the revolution increased to 1,500 rpm. Meanwhile, at running hours besides 3,506:11 and 4,453:45, the vibration amplitudes changes were consistent with increasing revolutions and running hours.

Figure 10 shows the vibration amplitudes at Location 4, which was located on the surface of the gearbox housing in the axial direction. At this location, the vibration amplitude trending was almost same for the different running hours during lower range of revolutions, except at running hours of 5,885:56 and 6,764:34. At 6,764:34 running hours, we observed that the vibration trending was inconsistent, with the highest amplitude of 25.10 m/s^2 recorded at 900 rpm.

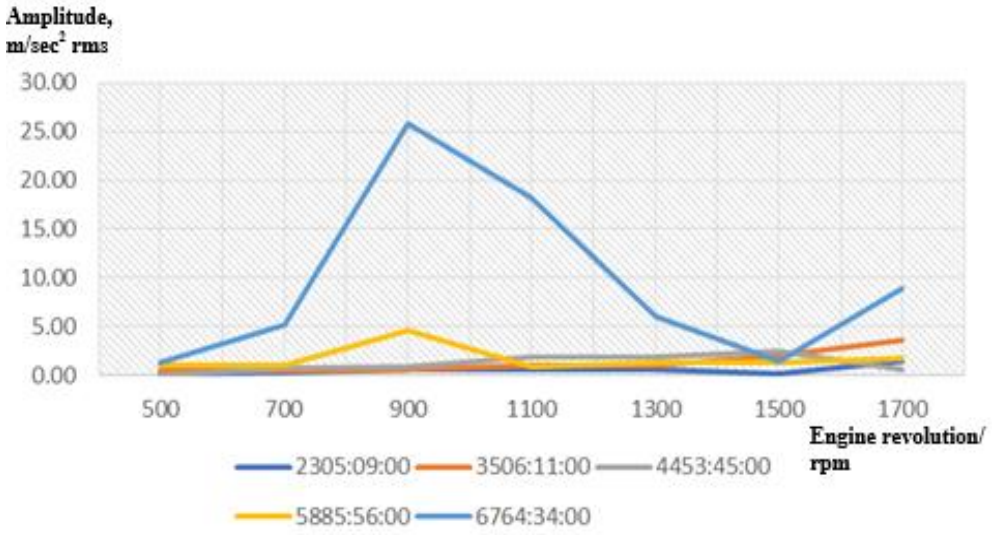

Figure 10: Comparison of measured vibration amplitudes at Location 4.

Figure 11 shows the vibration amplitudes at Location 5, which was located on the surface of the gearbox housing in the transverse direction. At lower range of revolutions, which was between 500 and 1,300 rpm, it was found that the vibration amplitudes were not consistent and showed signs of increment at lower rate after 900 rpm. In addition, at all engine revolutions, the vibration amplitudes increased drastically when the revolution was increased gradually from 1,300 to 1,500 rpm. The same pattern of consistent increment of vibration amplitudes were also observed when the revolution was increased from 1,500 to 1,700 rpm. The highest vibration amplitude of 13.50 m/s^2 was recorded at of 4,453:45 running hours and 1,700 rpm, which was far larger than the other engine revolutions at the same location. For the three locations on the gearbox, it was found out that Location 4 in the axial direction recorded the highest vibration amplitude.

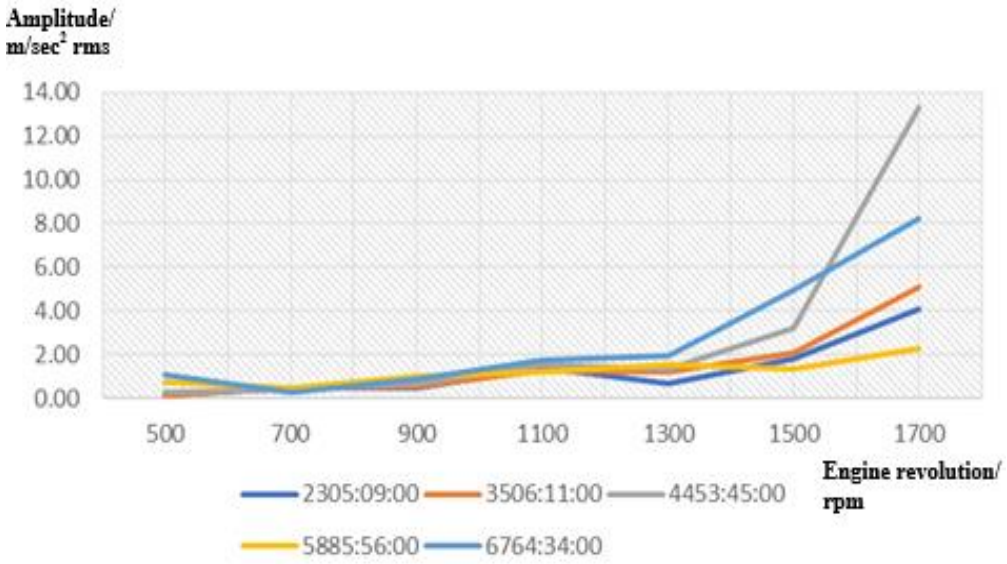

Figure 11: Comparison of measured vibration amplitudes at Location 5.

5. CONCLUSION

Based on this study, we can conclude that the resonance or critical speed symptom generated increments in terms of accelerations at different revolutions based on running hours. This shows that the presence of resonance along the ship propulsion shafting line, consisting of heavy machineries, such as diesel engine and gearbox, would contribute certain levels of vibrations at both sides of the driving and driven ends. Both these ends are connected using flexible coupling, which is subject to transmitted power and compensates for some degree of misalignment due to torsional vibration.

In this study, vibration measurement was utilised to detect the locations on a rotor dynamic system that recorded the highest levels of vibrations. We found that Location 1, which was in vertical direction on the surface of diesel engine, recorded the highest vibration amplitude. This finding could be supported by the fact that some of internal events inside the engine, such as continuous firing or explosion of air-fuel mixture, produced extremely high temperature combustion and higher impact on the engine body or cylinder block due to the upward-downward movements of pistons.

In previous studies, it was found that severe misalignment and torsional vibration could damage the flexible coupling, which connects the diesel engine and gearbox. In the long run, internal components of the coupling, such as gears and gaskets would fail miserably due to wear and tear, and contribute to catastrophic failure if it is not rectified it at an early stage.

Therefore, identifying failure symptoms at an early stage could benefit users and subsequently prevent catastrophic failures. Eventually, a CM programme could be utilised in detecting symptoms relating to coupling failure and give early warning or alarm to users. This would save time and money, as well as being important for the safety of operators because in certain cases, there is possibility for the coupling to fail horribly and fly off from the connection, which could cause injuries to nearby operators.

ACKNOWLEDGEMENT

We would like to express our sincere gratitude to the Royal Malaysian Navy (RMN) for their helpful support for this study. This work was also supported by the Science and Technology Research Institute for Defence (STRIDE) under the research project entitled *Condition Based Monitoring (CBM).*

REFERENCES

Desavale, R.G., Venkatachalam, R. & Chavan, S.P. (2013). Antifriction bearings damage analysis using experimental data based models. *ASME J. Tribology*, **135**: 041105.

Elamin, F. (2013). *Fault Detection and Diagnosis in Heavy Duty Diesel Engines Using Acoustic Emission.* PhD thesis, The University of Huddersfield, Huddersfield, UK.

Elamin, F., Gu, F. & Ball, A. (2010). Diesel engine injector faults detection using acoustic emissions technique. *Modern Appl. Sci.,* **4**: 3-13.

Grega, R., Homišin, J., Krajňák, J. & Urbanský, M. (2016). Analysis of the impact of flexible couplings on gearbox vibrations. *Sci. J. Silesian Univ. Tech.,* **91**: 43-50.

Gu, F., Yesilyurt, I., Li, Y., Harris, G. & Ball, A. (2006). An investigation of the effects of measurement noise in the use of instantaneous angular speed for machine diagnosis. *Mech. Syst. Signal Proc.,* **20**: 1444-1460.

Li, W.Y., Chai, Z.Y., Wang, M.Q., Hu, X.H. & Guo, Y.B. (2016). Online identification and verification of the elastic coupling torsional stiffness. *Shock Vibration.,* **Vol. 2016**: 2016432.

Li, Z., Yan, X., Guo, Z., Zhang, Y., Yuan, C. & Peng, Z. (2012). Condition monitoring and fault diagnosis for marine diesel engines using information fusion techniques. *Electron. Electr. Eng.,* **123**: 109-112.

Malla, C. & Panigrahi, I (2019). Review of condition monitoring of rolling element bearing using vibration analysis and other techniques. *J. Vib. Eng. Tech*, **7**: 407-414.

Mihaela, U. & Silviu, B. (2014). consideration about elastic coupling. *Appl. Mech. Mater.,* **657**:760-764.

Nistane, V.M. & Harsha, S.P. (2016). Failure evaluation of ball bearing for prognostics. *Procedia Tech.*, **23**: 179-186.

Pallavi, K. (2014). Experimental study to identify the vibration signature of bent shaft. *International J. Eng. Res. Tech.*,**3**: 214-216.

Salem, M.A., Diwakar, G. & Satyanarayana, M.R.S. (2012). Detection of Unbalance in Rotating Machines Using Shaft Deflection Measurement during Its Operation. *IOSR J. Mech. Civil Eng.,* **3**: 8-20.

Shamim, P. & Pallavi, K. (2014). Experimental study to identify the effect of type of coupling on unbalance using frequency spectrum analysis. *IOSR J. Mech. Civil Eng.*, **11**: 13-16.

Shi, H., Guo, J., Bai. X., Guo, L., Liu, Z. & Sun, J. (2020). Gearbox incipient fault detection based on deep recursive dynamic principal component analysis. *IEEE Access*, **8**: 57646-57660.

Shweta, S.P., & Tuljapure, S.B. (2015). Causes of coupling failures and preventive actions. *Int. J. Res. Appl. Sci. Eng. Tech.,* **3**: 412 – 415

Sinnasamy, Y., Sa'at, N.A., Nain, H. & Ahmad, K.A. (2020). Vibration analysis of flexible coupling by considering shaft misalignment. *Defence S&T Tech. Bull*., **13**: 227-239.

Vishwakarma, M., Purohit,R, Harshlata, V. & Rajputa, P. (2017). Vibration analysis & condition monitoring for rotating machines: A review. *Mater. Today Proc.*, **4**: 2659-2664.

EVALUATION OF INTERNAL BUTTERFLY VALVE LEAKAGE BY ACOUSTIC EMISSION

Ismail Mustapha[1,2*], Mohamad Hanif Md Saad[1], Mohd Zaki Nuawi[1], Suhairy Sani[1,2], Shukri Mohd[2] & Siti Fatahiyah Mohamad[3]

[1 \]Department of Mechanical and Materials Engineering, Faculty of Engineering and Built Environment, Universiti Kebangsaan Malaysia (UKM), Malaysia
[2]Industrial Technology Division, Malaysian Nuclear Agency, Malaysia
[3]Radiation Processing Technology Division, Malaysian Nuclear Agency, Malaysia

[*]Email: ismail@nm.gov.my

ABSTRACT

Internal leakage due to damage of the valve seal is one of the most common butterfly valve problems. When the valve operates for a long time, this often results in sealing as well as exposure to high temperature and pressure. This study applies the acoustic emission technique to detect internal butterfly valve failure since it can measure leakage at exceptionally low frequencies. The 4-inch butterfly valve has been used for the simulation of the pipe system in the experiment. Low-frequency sensors are employed to measure the signal generated by the valve leakage. The results of the experiment reveal that the butterfly valve's frequency range with a low-frequency transducer is 15-30 kHz. The AE signal characteristic is capable of analysing the waveform, power spectrum density (PSD), Fast Fourier transform (FFT) and continuous wavelet transform (CWT) for each leakage mode.

Keywords: *Butterfly valve; acoustic emission; gas leakage; fast fourier transform (FFT); continuous wavelet transform (CWT).*

1. INTRODUCTION

Butterfly valves are usually preferable for their low cost and less space requirement. The butterfly valve's function is to control, isolate and monitor the flow of fluids. It involves rapid operation and low-pressure drop. It only takes a quarter turn to make a closed position open. A butterfly valve regulates fluid flow through a circular pipe or tube. It is simply a circular disc with a pivot axis flowing right to the steering material (Shashi Menon 2015). In a piping system, valves are used to isolate pipe parts for maintenance purposes, allow fluids to flow from one location to another or stop fluid flow, protect pipes from damage and prevent fluid loss. Valve leakage can occur from seat or seal damage. This can result from erosion of the sealing surface due to non-drying and non-anti-corrosive treatment. Faulty design is another reason as well as sphere damage. This can be caused by non-standard installation or welding. Valve leakage can also occur from loosely closed valves since dirt, debris or any other obstructions can attach to it, affecting its process efficiency (Ren *et al*., 2018; Bin Zhu *et al*., 2019). Valve leakage can be classified into two types: external leakage (Chan *et al*., 2019), which poses potential environmental and safety hazards (Mostafapour & Davoudi, 2013), and internal leakage where the leakage remains in the piping system, posing potential safety hazards to the system (Li *et al*., 2017).

Various methods of pipeline condition monitoring have been proposed to detect valve defects such as vibration and noise measurements (Shashi Menon 2015). The methodologies for detecting leakage in the pipeline system can be categorised as either hardware-based or software-based systems (Li *et al*., 2014). This includes fibre optics (Zhou *et al*., 2008), visual inspection, hydrocarbon distributed sensor

cables (Sandberg *et al*., 1988), electromagnetic cables (Duong *et al*., 2020) and acoustic emission (Rondeau *et al*., 2018).

Recently, acoustic emission has proven to be effective for valve leakage detection due to high sensitivity of AE sensors which can instantly identify any abnormal state in the pipeline without shutting down the entire system (Song & Li 2018). Acoustic emission is recognised as effective for valve leakage detection due to the advanced data acquisition and processing speed that are capable of handling a vast amount of signals (Quy *et al*., 2019). The AE sensors provide enough sensitivity within its operating frequency range, typically 20 to 1,200 kHz, to instantly identify any abnormal state in the pipeline without shutting down the entire system (Song & Li 2018).

The development and implementation of proper and reliable leakage detection methods, which is the acoustic emission (AE) technique, are crucial to circumvent inefficient processes (Toufique Hasan *et al*., 2015). However, further information and data are required to attain a reliable system that can determine the location and size of leakage. Previously accomplished research had only focused on the relationship between AE parameters and flow rate (Zhu *et al*., 2014). This paper presents the relationship between AE parameters and the different pressures, further examining the acoustic leak signal's characteristics due to gas leakage of the butterfly valve in the frequency domain.

The aim of this research is to estimate the butterfly valve's internal leakage through different AE signal parameters. The AE parameters include power spectral density, root mean square and frequency domain. The gaps in the butterfly valve manipulate and stimulate different internal leakages in the pipelines. The wavelet (transform) is also presented to identify the frequency for small leakage in the valve. The research focuses on gas flow in the valve where the signal is generated at the wall, and the sensor detects the passive signal.

2. INTERNAL LEAKAGE ACOUSTIC EMISSION

Internal leaks occur in the butterfly valve due to seal failure and partial valve closure. Acoustic emissions are the best way to identify gas passing through the valve for failure detection (Yan *et al*., 2015). This is because small changes in the signal will demonstrate the significant of leakage. Figure 1 illustrates the configuration of measuring the leakage using the acoustic emission of a butterfly valve. This is the best configuration of the sensor arrangement for the butterfly valve because the detection is nearest to the disc where high stress occurs (Thampi, 2015). The pressure is measured at the inlet and outlet when the valve releases the fluid based on the percentage of the gap to simulate the small leakage. The butterfly valve's main components are the stem, body and disc which control the flow. In order to identify the leakage, measurements should be taken at the outlet (Kaewwaewnoi *et al*., 2005). Therefore, the small opening on the valve disc simulates the leakage and measures the pressure as a different pressure within the inlet and outlet (Lin & Schohl, 2004; Al-lababidi *et al*., 2009).

The pressure difference is calculated by the relative ratio of upstream-to-downstream pressure ratio (Kim *et al*., 2019). The pressure difference is defined as:

$$P_\tau = \frac{P_1}{P_2} \tag{1}$$

where P_1 is the pressure upstream and P_2 is the pressure downstream of the butterfly valve.

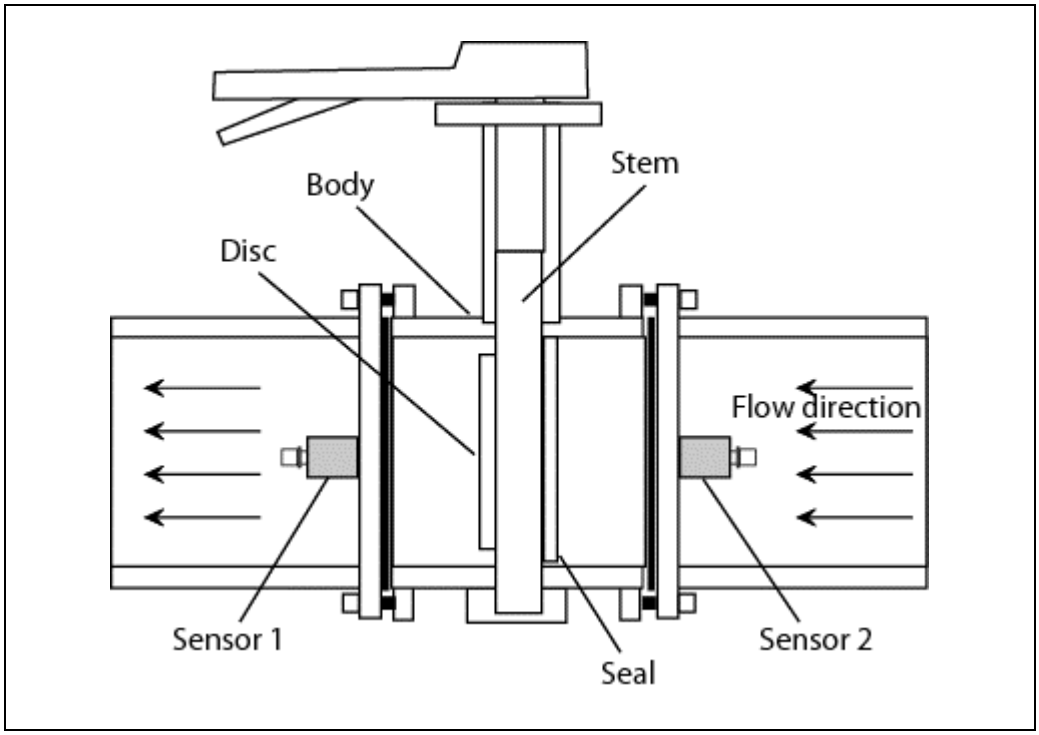

Figure 1: Valve configuration setting of AE sensor.

3. EXPERIMENTAL SETUP

A pipe system was designed using a 4-inch diameter butterfly valve. The 4-inch butterfly valve was connected to the middle of the pipeline to balance the input and output pressures. The high precision pressure gauge (WIKA CPG1500) was installed at a different location to monitor the experiment's pressure. Two low frequency transducers at range 5 to 30 kHz were also installed to detect small flow changes based on the stress wave variation, ranging from 5 to 60 kHz.

The Micro-II of Digital AE Systems monitors the internal signal from the valve leakage at frequency ranges of 5 to 250 kHz, which can be detected using the sensor's different sensitivities. The pipeline system was integrated with two different AE software to perform further analyses. The AEwin software was used for data collection in the continuous monitoring of leakage conditions at the butterfly valve until the pressure dropped to 50 kPa. The data obtained was processed and analysed using the NOESIS Ver.9 software.

Before the actual experiment was accomplished, the sensor's location was determined and calibrated to obtain the frequency's primary data range for the internal leakage. Three different sensors were used at three different locations with highly detectable frequency. The R1.5 sensor was fixed at the flange during the full experimental setup. Figure 2 presents the schematic diagram of the experimental setup.

At the beginning of the experiment, the butterfly valve was completely closed, and the gas was gradually released to the pipeline system to achieve a maximum of 700 kPa pressure, as indicated by the pressure gauge. The control pressure valve is the open graded control with the gaps of 1 to 3 percent, which can simultaneously reduce the internal pressure. The AEwin software generated and recorded data of the waveform, power spectrum density and the FFT of the designed gap. The collected data was analysed using the NOESIS software and presented as waveform, PSD, FFT and CWT.

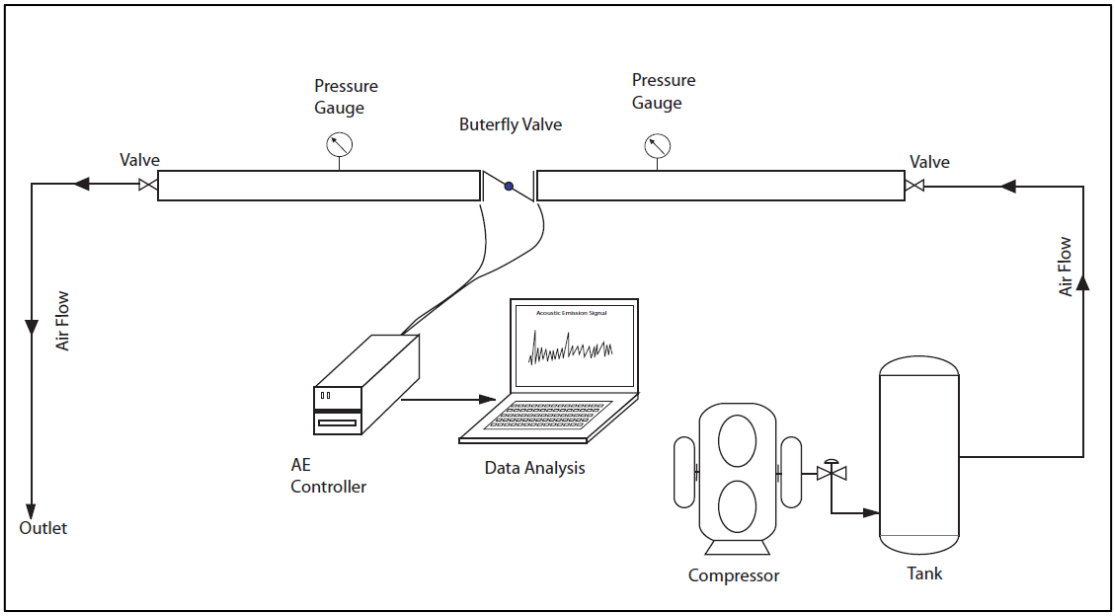

Figure 2: Schematic diagram of experimental arrangement.

4. RESULTS & DISCUSSION

4.1 AE Waveform

Figure 3 presents a typical AE waveform in the leakage valve at three gap percentages. The waveform plots the amplitude (V) as a function of 0 to 1,026 vs the time domain. The waveform gaps of 1, 2 and 3% provided the amplitudes of 0.15, 0.3 and 0.4 V respectively. The voltage exhibited a significant increment as the gap percentages increased. Therefore, the acquired waveform can be used as a signal pattern to compare different conditions monitored in real-time as well as identify leakage in the pipeline system. This demonstrates that continuous low-amplitude AE signals are generated from low-energy sources and thus, the amplitude and pressure increase due to the occurrence of fluid leakage and internal frictions.

4.2 Power Spectral Density (PSD)

The PSD analysis was conducted to support the AE signal waveform. The analysis results indicate that the PSD spectrum was at a frequency range of 0 to 500 kHz at 1, 2 and 3 percent gaps, as shown in Figure 4. The power spectrum exhibited an increment as the gap leakage increased, which is similar to the waveform analysis. It can be concluded that the signal from the presented PSD is not a unique power associated with the amplitude and voltage. However, the power spectral density function is a handy tool to identify oscillatory signals in time series data due to the amplitude signal. From the power spectral density, high-frequency range variations can be determined. Hence, further analysis should be conducted.

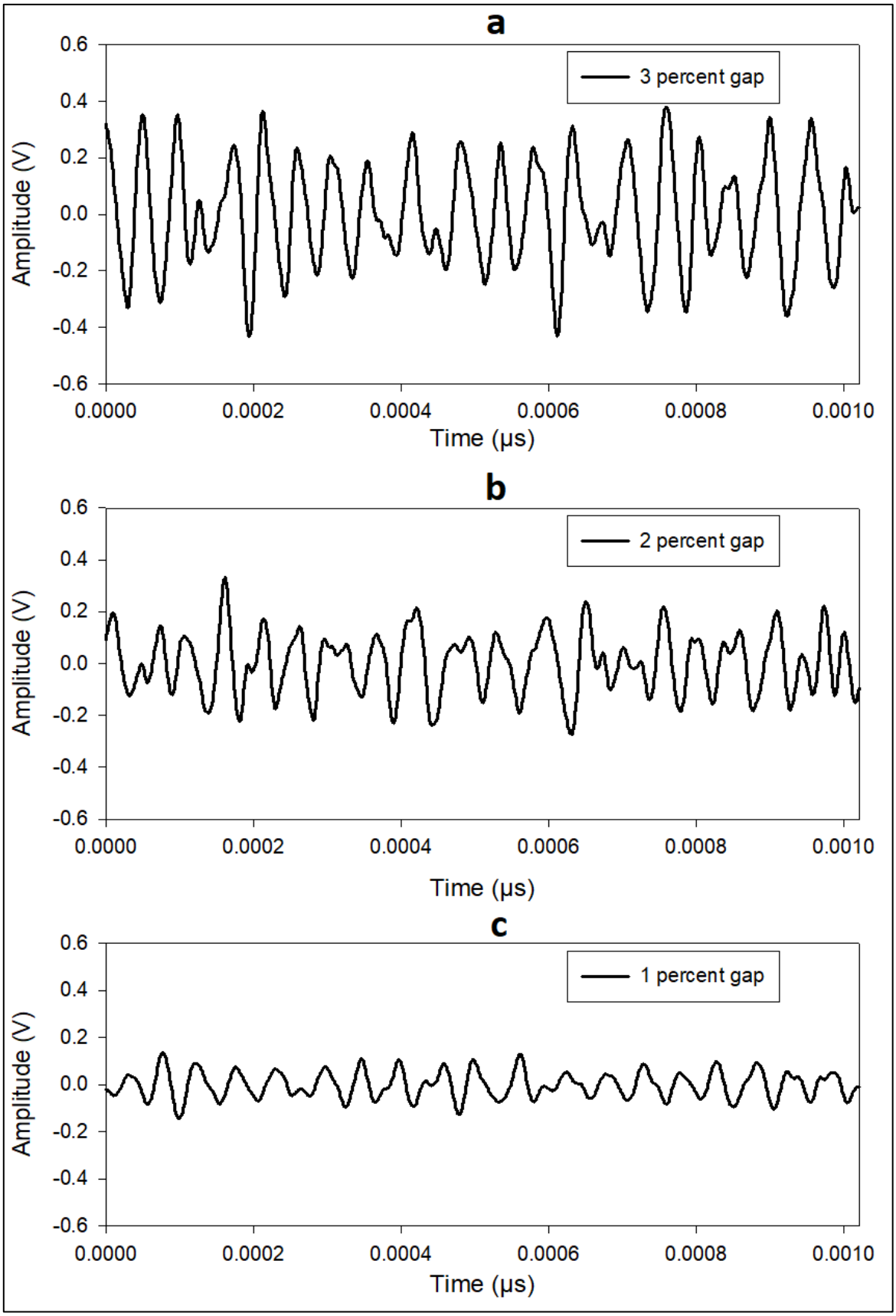

Figure 3: Waveform spectra of the different internal leakage gaps monitored: (a) 3% gaps, (b) 2% gaps and (c) 1% gaps.

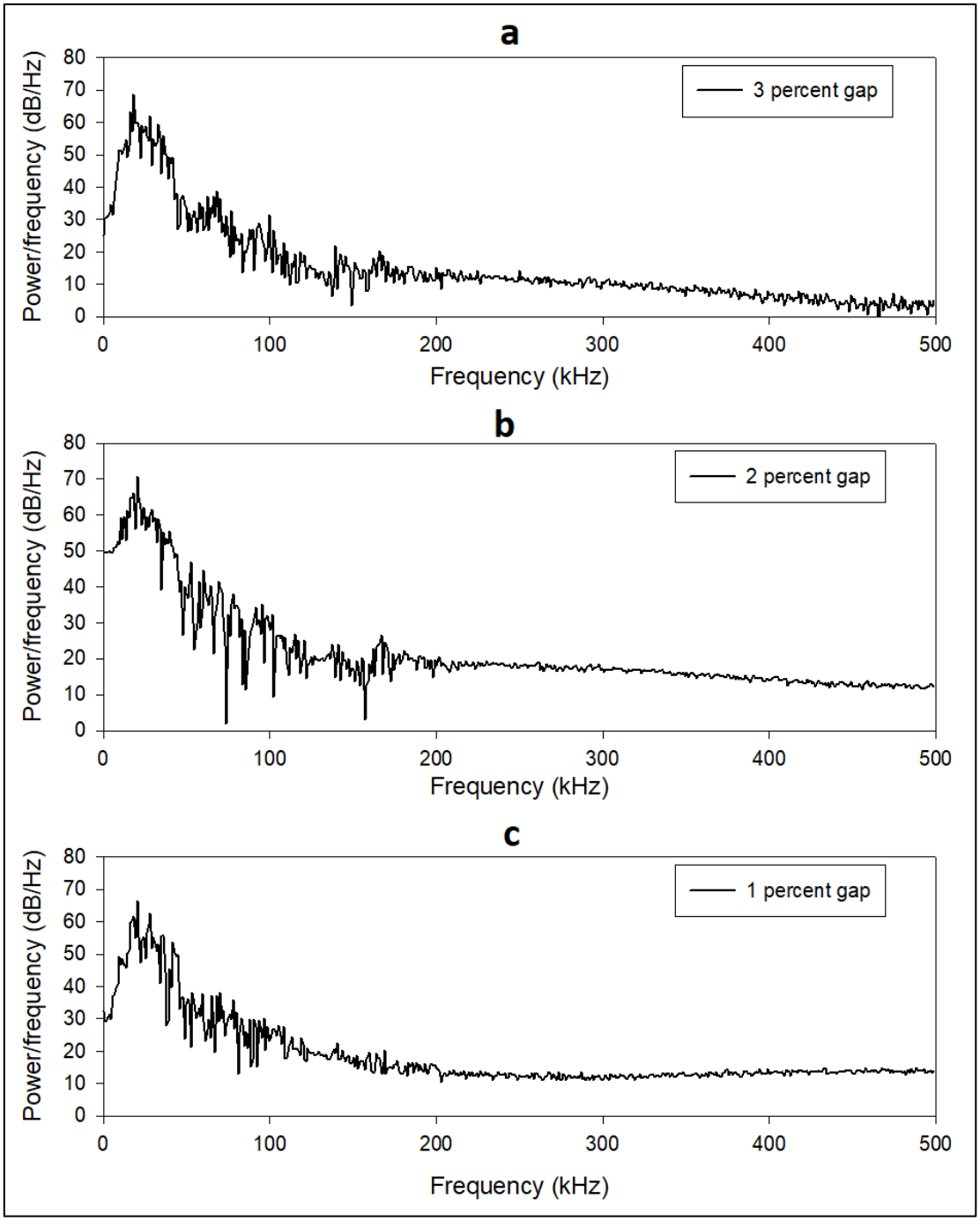

Figure 4: Power spectrum for leakage modes: (a) 3% gaps, (b) 2% gaps and (c) 1% gaps.

4.3 Fast Fourier Transform (FFT)

FFT is a method that transforms a function of time into a function of frequency. In this study, the leakage measurement at each butterfly valve failure mode was calculated, resulting in the spectrum of leakage frequency, as shown in Figure 5. From the graphs, the leakage gap optimises from 1 to 3 percent at 14 to 30 kHz, which is directly proportional. This result converts a signal from its original domain to be represented in the frequency domain and vice versa. The range obtained can be used to transform the time domain, which is useful for time-dependency leakage phenomena.

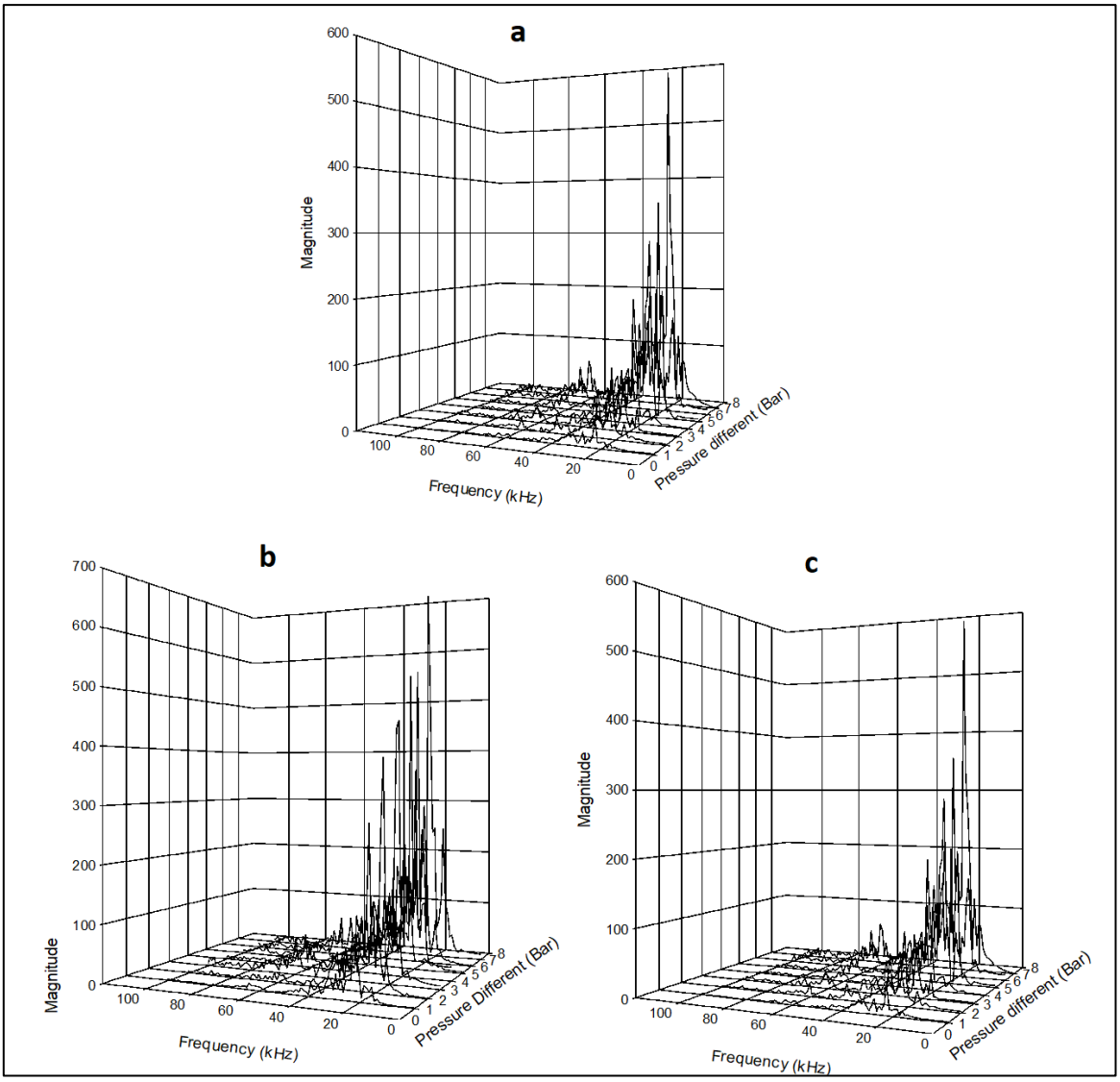

Figure 5: FFT for various leakage modes: (a) 3% gaps, (b) 2% gaps and (c) 1% gaps.

4.4 Continuous Wavelet Transform (CWT)

The CWT provides an overcomplete representation of a signal by allowing the wavelets' translation and scale parameters to continuously vary on the butterfly leakage valve. The CWT presented in Figure 6 shows a similar pattern even at different leakage modes within 18 to 25 kHz frequencies. The CWT is capable of simultaneously describing a broad range of signals at any time and frequency domain.

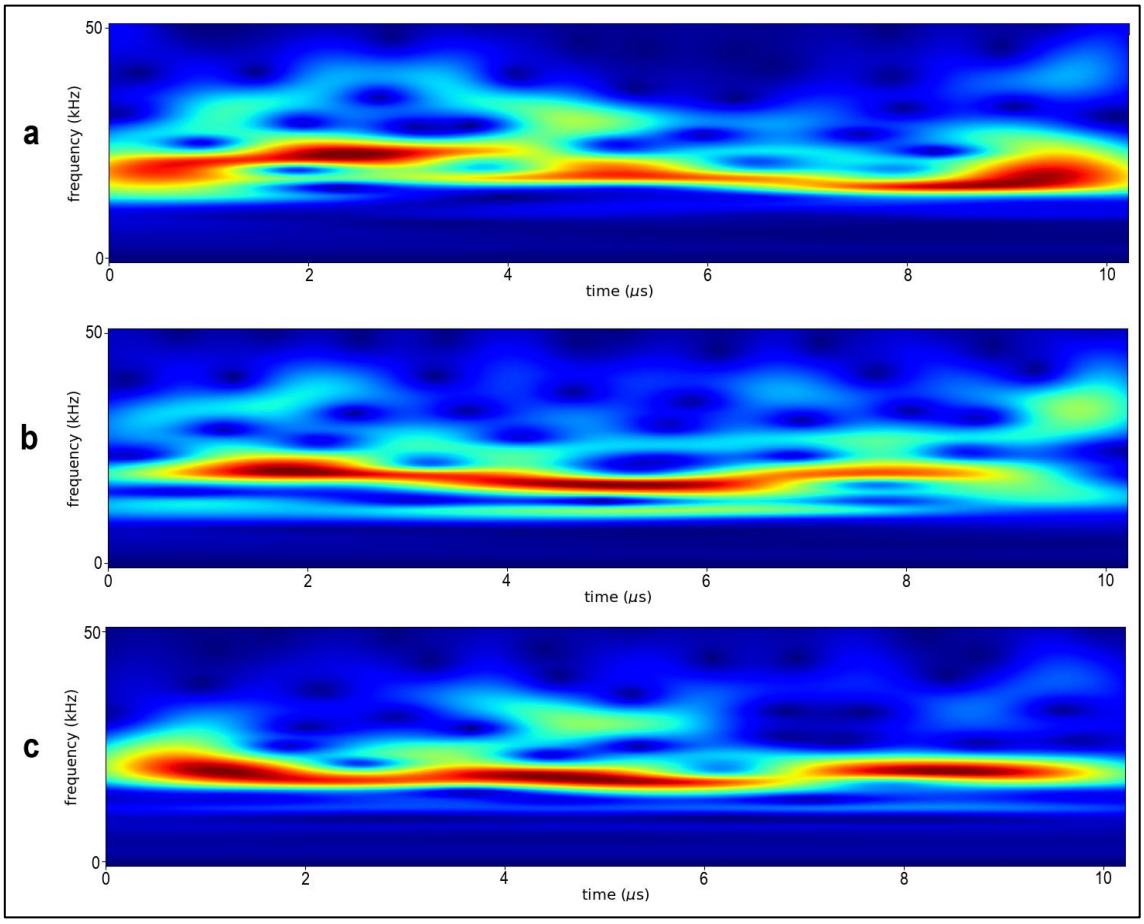

Figure 6: Continuous wavelet transform for butterfly valve: (a) 3% gaps, (b) 2% gaps and (c) 1% gaps.

5. CONCLUSION

The investigation of internal leakage using the butterfly valve was achieved by manipulating the valve gaps and pressure in a developed piping system. The sensor location at the valve body allowed the collection of accurate signals due to its close proximity to the leakage gap. Manipulating the valve gaps by 1-3% successfully stimulated the internal gas leakage of the butterfly valve. The AE parameters at different valve gaps were successfully optimised using FFT, PSD, AE waveform and CWT. The PSD spectrum presented an increment as the gap leakage increased. The pressure simultaneously drops corresponding to the frequency obtained to provide an optimum value, which was also demonstrated in the waveform analysis. The FFT analysis has shown that the frequency bands of 18 to 25 kHz are the best for determining leakage from gaps in the valve. The CWT also presented a similar pattern to the FFT frequency. This method for measuring leakage in the butterfly valve is more feasible than assessing the leakage gap for improving leak detection. It was observed that the leakage characteristics obtained by PSD and waveform, which also applies to AE, are essential features for condition monitoring.

ACKNOWLEDGMENT

The authors would like to acknowledge the Malaysian Ministry of Science, Technology and Innovation as well as researchers from the Malaysian Nuclear Agency for their assistance.

REFERENCES

Al-lababidi, S., Addali, A., Yeung, H., Mba, D. & Khan, F. (2009). Gas void fraction measurement in two-phase gas/liquid slug flow using acoustic emission technology. *J. Vib. Acoust.: T. ASME,* **131**: 0645011–0645017.

Chan, T.K., Chin, C.S. & Zhong, X. (2019). Review of Current Technologies and Proposed Intelligent Methodologies for Water Distributed Network Leakage Detection. *IEEE Access*, **6**: 78846–78867.

Duong, B.P., Kim, J.Y., Jeong, I., Kim, C.H. & Kim, J.M. (2020). Acoustic emission burst extraction for multi-level leakage detection in a pipeline. *Appl. Sci.*, **10**: 1–11.

Kaewwaewnoi, W., Prateepasen, A. & Kaewtrakulpong, P. (2005). Measurement of Valve Leakage Rate using Acoustic Emission. *Proc. 2nd Int. Conf. Electr. Eng./Electron. Comput. Telecommun. Inf. Technol.*, 10-14 July 2005, Kunming, China.

Kim, C.K., Lee, S.M. & Jang, C.M. (2019). Performance analysis of a ball valve used for gas pipelines by introducing nondimensional parameters. *Adv. Mech. Eng.*, **11**: 1–10.

Li, S., Wen, Y., Li, P., Yang, J., Dong, X. & Mu, Y. (2014). Leak location in gas pipelines using cross-time – frequency spectrum of leakage-induced acoustic vibrations, *J. Sound Vib.*, **333**: 3889–3903.

Li, Z., Zhang, H., Tan, D., Chen, X. & Lei, H. (2017). A novel acoustic emission detection module for leakage recognition in a gas pipeline valve. *Process Saf. Environ. Prot.*, **105(**: 32–40.

Lin, F. & Schohl, G. A. (2004). CFD prediction and validation of butterfly valve hydrodynamic forces. *Proc. 2004 World Water Environ. Res. Congress: Crit. Transitions Water Environ. Res. Manage.*, 27 Jun - 1 July 2004. Salt Lake City, Utah, USA.

Mostafapour, A. & Davoudi, S. (2013). Analysis of leakage in high pressure pipe using acoustic emission method. *Appl. Acoust.*, **74**: 335–342.

Quy, T. B., Muhammad, S. & Kim, J. M. (2019). A reliable acoustic emission based technique for the detection of a small leak in a pipeline system. *Energies*, **12**: 1472.

Ren, L., Jiang, T., Jia, Z. Guang, Li, D. Li, D., Yuan, C. & Li, H. (2018). Pipeline corrosion and leakage monitoring based on the distributed optical fiber sensing technology. *Meas.: J. Int. Meas. Conf.*, **122**: 57–65.

Rondeau, A., Lafargue, E. & Cartier, F. (2017). Leakage noises in valves. *Proc. Meet. Acoust.*, 18-20 December 2017, Honolulu, Hawai, USA.

Sandberg, C., Holmes, J., McCoy, K. & Koppitsch, H. (1988). Application of a continuous leak detection system to pipelines and associated equipment. *Ind. Appl. Soc. 35th Annu. Pet. Chem. Ind. Conf.*, 12-14 September 1988, Dallas, USA.

Shashi Menon, E. (2015). *Transmission Pipeline Calculations and Simulations Manual*. Gulf Professional Publishing, UK.

Song, Y.J. & Li, S.Z. (2018). Leak detection for galvanized steel pipes due to loosening of screw thread connections based on acoustic emission and neural networks. *J. Vib. Control*, **24**: 4122–4129.

Thampi, A. (2015). *Seat Leakage Analysis of a Valve using Numerical Methods*. Manipal Institute of Technology, India.

Toufique Hasan, A.B.M., Matsuo, S. & Setoguchi, T. (2015). Characteristics of transonic moist air flows around butterfly valves with spontaneous condensation. *Propul. Power Res.*, **4**: 72–83.

Yan, J., Heng-Hu, Y., Hong, Y., Feng, Z., Zhen, L., Ping, W. & Yan, Y. (2015). Nondestructive detection of valves using acoustic emission technique. *Adv. Mater. Sci. Eng*., 749371

Zhou, J. Y., Jin, S.J., Feng, H., Zeng, Z.M. & Qu, Z.G. (2008). Study on oil and gas pipeline leakage real-time inspection system based on distributed optical fiber. *Key Eng. Mater.*, **381–382**: 447–450.

Zhu, S. Bin, Li, Z.L., Zhang, S.M., Ying, Y. & Zhang, H.F. (2019). Deep belief network-based internal valve leakage rate prediction approach. *Meas.: J. Int. Meas. Conf.*, **133**: 182–192.
Zhu, L., Zou, B., Gao, S.H., Jiang, M. & Li, Z.P. (2014). Research on gate valve internal leakage detection based on acoustic emission signal processing. *Adv. Mater. Res.*, **1037**: 169–173.

ELECTRICAL, MORPHOLOGICAL AND SURFACE ROUGHNESS ANALYSIS OF SILVER NANOPARTICLES-FILLED EPOXY CONDUCTIVE INK

Adzni Md. Saad[1,2], Mohd Azli Salim[1,2,3*], Murni Ali[4], Feng Dai[5], Fauzi Ahmad[1] & Roshidah Hamidi[1]

[1]Fakulti Kejuruteraan Mekanikal, Universiti Teknikal Malaysia Melaka (UTeM), Malaysia
[2]Intelligent Engineering Technology Services Sdn. Bhd., Malaysia
[3]Advanced Manufacturing Centre, Universiti Teknikal Malaysia Melaka (UTeM), Malaysia
[4]NanoMalaysia Berhad, Malaysia
[5]China Railway Eryuan Engineering Group Co., China

[*]Email: azli@utem.edu.my

ABSTRACT

Conductive ink has become a potential alternative to replace the conventional circuitry in electronic applications. Due to this, various efforts have been conducted to obtain the optimum ink formulation that can fulfill the current demand. The objective of this study is to determine the performance of different formulations of silver nanoparticles-filled epoxy conductive ink with various filler loadings in terms of electrical conductivity. The main investigated parameter was the sheet resistance of the composition. The changes of morphology of the ink surface and surface roughness were also examined, which directly correlated to the sheet resistivity. The obtained results showed that the minimum threshold of silver nanoparticles (AgNP) filler required was 60 %wt for the ink to conduct electricity. However, this filler loading was not acceptable because of the wide dispersion of data. The ink filler loadings that can conduct electricity also showed the presence of granular particles on the ink layer surfaces, which also increased their surface roughness. The sheet resistance value also achieved a saturated value with filler loading of 90 %wt. It means that further addition of filler loading is not going to further improve the sheet resistivity of the composition. Based on this study, it can be summarised that the percentages of AgNP filler loadings of conductive ink that can fulfil the acceptable performance are between 70 to 90 %wt.

Keywords: *Silver nanoparticles conductive ink; resistivity; morphology; surface roughness; filler loadings*

1. INTRODUCTION

Conductive ink has been considered as one of the most magnificent findings in the field of electronic circuitry. It can be used to replace conventional wiring and is beneficial for simple circuitry that requires low-manufacturing costs (Mokhlis *et al*., 2020). Recently, there have been many other various applications of conductive ink, such as for the construction of batteries (Kazemzadeh *et al.*, 2020), supercapacitors (Lehtimäki *et al*., 2014) and sensors (Lynch *et al*., 2020). With the advancement of the technology and more research efforts being conducted in this field, it opens more possibilities of performance enhancement of conductive ink. Various factors can contribute to the performance of conductive ink and the main factor is the filler of the ink. It plays an important role for conducting electricity by allowing the electron flow between the filler particles with low resistivity (Ismail *et al.*, 2020). Furthermore, the composition and printing methods are also important in determining the performance of the conductive ink (Yunos *et al*., 2020).

Silver nanoparticles (AgNP) have been used as the filler of the composition of conductive ink. It is due to the well-known inherent properties of silver as a good electrical conductor. Besides that, it also possesses excellent optical and chemical properties (Bose *et al*., 2018). They also possess high sintering efficiency (Huang *et al*., 2014), undemanding sintering conditions (Chen *et al*., 2020), and chemical stability (Titkov *et al*., 2018). Unfortunately, the requirement of having heat treatment

through sintering limits the utilisation of substrates to be used with the conductive ink. This heat treatment is required to remove hazardous organic solvents, such as toluene, xylene and alkane (Park *et al.*, 2018). However, AgNP has high formulation stability and can be printed using various different printing techniques (Kosmala *et al*., 2011).

For the preparation of AgNP filled epoxy conductive ink, various types of printing methods have been introduced by previous studies. These include inkjet printing, gravure printing and screen printing (Saad *et al*., 2020). For the purpose of this study, it does not require a high resolution of ink pattern. Due to this, the simplest method of printing is utilised to produce the ink tracks on the substrate, which is the doctor blade method. It can be considered as a practical option because of the capability to produce a thick film in a single pass. This reduces tremendously the processing time (Rajan *et al*., 2016).

In studying the performance of AgNP filled epoxy conductive ink, some important parameters need to be examined as the baseline for more advanced investigation works. The first is the minimum content of AgNP in the ink composition that has the capability to work as conductive ink. For this, the measurement of sheet resistivity is performed as it can directly translate to the capability of the ink formulation to conduct electricity. In contrary to metal to metal contact that produces contact resistivity, the more prominent parameter that influences the electrically conducted material for the thin sheet is sheet resistivity (Peng *et al*., 2015). Then, morphological analysis is performed to study the microstructure of the ink layer surface that contributes to the capability of conducting electricity. Different ink formulations produce different ink layer microstructures. In addition, most of the morphological analysis is carried out by referring to the captured images of the microstructure. It requires changes in the physical structure of the ink to explain the results of the analysis. Therefore, surface roughness analysis is performed to obtain the correlation between the morphology of the ink with its physical attributes (McGrath *et al*., 2021).

This study aims to provide initial insight of using AgNP as the filler element for the production of conductive ink. A stable ink formulation that has the capability to conduct electricity was obtained by determining the sheet resistance of the ink formulation at different filler loadings. Then, morphological analysis was performed to study the microstructure of the ink layer that contributes to the electrical conductivity capabilities. The morphological analysis was conformed to the physical features of the ink layer by obtaining the surface roughness of the ink with different filler loadings.

2. METHODOLOGY

2.1 Test Samples Preparation

The material used for this experiment is AgNP as the filler element, epoxy as the binder, and hardener to harden the mixture composition. The composition weight of the ink loading shown in Table 1 was used to produce the total weight of 2 g for each sample.

The mixture composition was blended using the manual stirring process with a glass rod. For filler loadings of 10 to 50 %wt, they were stirred for 5 min at room temperature, while for filler loadings of 60 to 90 %wt, the stirring time was increased to 10 min. This was to ensure that consistency of the mixture due to the increased viscosity of the composition with the increment of filler loading (Htwe *et al*., 2019). Then, the produced ink was printed on the glass substrate using the doctor-blade technique. It was performed by covering the whole glass slide with cellophane tape except for the opening gap for the printed ink. Then, the ink was dropped on the glass slide and a sharp blade was used to spread the ink by moving across the substrate at a constant speed and filling in the gap.

The printed ink track is illustrated in Figure 1. For each sample, two tracks were printed, which were labelled as Tracks A and B. For each position, three points were determined for the measurement. Overall, six points were investigated for each sample. The purpose of having two ink tracks for one glass slide substrate is to examine the homogeneity of the conductive AgNP in the mixture by using a

limited amount of formulated mixture. It is one of the main characteristics of determining the electrical conductivity of mixture composition (Cai *et al*., 2019). Then, the samples were cured in an oven at 160 ºC for 1 h. The purpose of the curing process is to anneal the ink mixture by removing the excess solvent that can become an obstruction to the conductive network paths, which results in better electrical conductivity. Furthermore, it can enhance the adhesion of the ink tracks to the substrate (Htwe *et al*., 2019).

Table 1: Composition of ink loading.

Sample	Filler		Binder		Hardener (g)	Total (g)
	(%)	(g)	(%)	(g)		
1	10	0.2	90	1.8	0.54	2
2	20	0.4	80	1.6	0.48	2
3	30	0.6	70	1.4	0.42	2
4	40	0.8	60	1.2	0.36	2
5	50	1.0	50	1.0	0.30	2
6	60	1.2	40	0.8	0.24	2
7	70	1.4	30	0.6	0.18	2
8	80	1.6	20	0.4	0.12	2
9	90	1.8	10	0.2	0.60	2

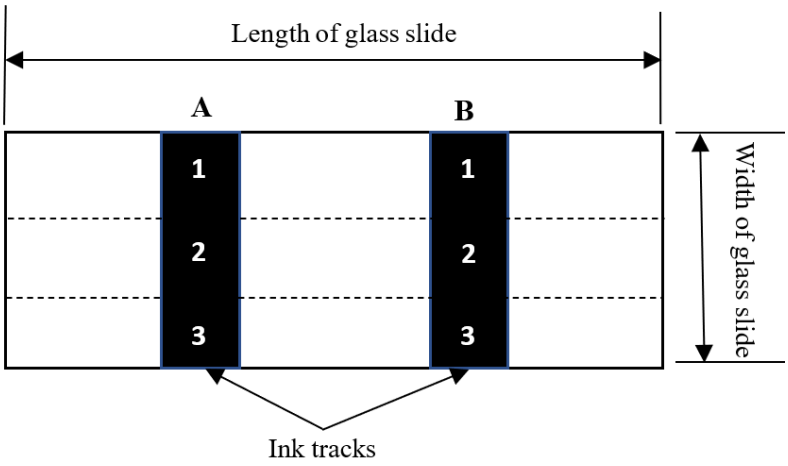

Figure 1: Printed ink tracks on the glass slide substrate.

2.2 Measurement of Sheet Resistivity

For the sheet resistivity measurement, a four-point probe was used. This is because it is suitable for low resistivity thin film and its independence of the square (Ismail *et al*., 2020). For each point, three sheet resistivity readings were taken. Then, the standard deviation of the data was calculated to obtain its dispersion behaviour. Then, the estimation of error (*E*) for the sheet resistivity values were calculated using the following equation:

$$E = \left| \frac{Resistivity\ at\ one\ point - Average\ resistivity}{Average\ Resistivity} \right| \times 100\% \quad (1)$$

2.3 Surface Morphology

For the morphological analysis, the microscopy technique was used to obtain the images of the ink layer surface. Three different resolutions were used to capture the image for every investigated point, which where 5x, 10x and 20x. All the images were recorded in the computer attached to the microscope. Surface morphology is a qualitative analysis by utilising the graphical images of the ink layer surface in terms of the particles' size, shape, profile and structure. With the addition of different filler loadings, it changes the ratio of material composition. Therefore, it affects the atomic and molecular arrangement of the compound (Kulkarni, 2014), which is also portrayed on the ink layer surface. The correlation between the changes of microstructure surface and sheet resistivity can then be obtained.

2.4 Surface Roughness Measurement

For surface roughness, the measurement was taken using a surface roughness sensor. It was performed by moving the sensor probe along the ink layer surface. For this study, two directions of the movement were used, which were the horizontal and vertical directions. Horizontal direction indicates movement along the length of the glass slide, while vertical direction indicates movement along the width of the glass slide. For every investigated point, three surface roughness measurements were taken to increase the accuracy and reliability of the obtained data. Surface roughness measurement can provide qualitative data in reinforcing the surface morphological analysis to determine the effect of filler loadings on sheet resistivity (Buszewski *et al*., 2010). It has a direct correlation with the presence of AgNP granules on the ink layer surface.

3. RESULTS AND DISCUSSIONS

3.1 Sheet Resistivity

The sheet resistivity of different points for different percentages of filler loading is shown in Figure 2. The conductivity of composites is not a straightforward phenomenon. As mentioned by Merilampi *et al*. (2009), there several different controlled parameters involved such as conductive filler, surface resistance of the filler and hopping conductivity. This experiment attempts to discover the direct correlation between the amount of conductive filler and sheet resistivity behaviour. Even though the experiment was carried out for filler loadings starting from 10 until 90 %wt of AgNP, the sheet resistivity results can only be obtained for the filler loadings starting from 60 to 90 %wt. This is because low content of filler loading does not produce any electrical conductivity.

The presence of AgNP in the composition is inadequate to produce a continuous conductive path that allows the electrons to flow in the composition, which produces sheet resistivity. By adding the amount of AgNP in the conductive ink composition, it increases the network path of silver particles and effectively allows the current to flow (Mou *et al*., 2020). Thus, by having more amount of AgNP inside the composition, it reduces the sheet resistivity. This is proven by the collected data, which shows that filler loading of 60 %wt produces the highest sheet resistivity both for Tracks A and B with values of 150.53 and 369.65 Ω/sq respectively. With the addition of filler loading to 70 %wt, it significantly reduces the values of sheet resistivity. Consequently, the values of sheet resistivity for filler loadings of 80 and 90 %wt also show substantial reduction but with minimum difference between Tracks A and B. The reduction trend as illustrated in Figure 2 also shows that the curve achieves a plateau at filler loading 90 %wt. This indicates that sheet resistivity already has achieved a saturated level and any addition of AgNP in the ink mixture composition of more than filler loading of 90 %wt will produce insignificant improvement in sheet resistivity. It only increases the cost of using an unnecessary amount of AgNP in the composition.

The dispersion of sheet resistivity data is shown in Table 2. It shows that filler loading of 60 %wt has the worst data disparity as compared to other the filler loadings. By increasing the filler loading to 70 %wt, it significantly reduces the values of standard deviation. High standard deviation values indicate that the sheet resistivity values are scattered in a wider range across all the examined points. It implies

inconsistency of AgNP in the composition, whereby some portion of the ink paste has a higher content of AgNP as compared to others. This occurrence is because of the limited amount of AgNP in the mixture. Furthermore, it shows the preparation method used, in particular the manual mixing process is unable to create consistent distribution or dispersion of AgNP inside the compound (Mou *et al*., 2020). The value for filler loading of 60 %wt should become the low threshold value for filler loading when preparing AgNP filled conductive ink, which is prepared using a manual mixing process. Even though it can measure the occurrence of electrical conductivity and generates sheet resistivity, the data dispersion is unacceptable to be used for further analysis. On the other hand, filler loading of 90 %wt shows the smallest values of standard deviation. It indicates the minimum distribution of sheet resistivity as compared to the average values. This is caused by the increased amount of conductive material inside the composition, which allows consistent values of electrical conductivity to exist at all measured points of the sample (Merilampi *et al*., 2009). Furthermore, the very low values of sheet resistivity generated by filler loading of 90 %wt also contribute to the low dispersion data.

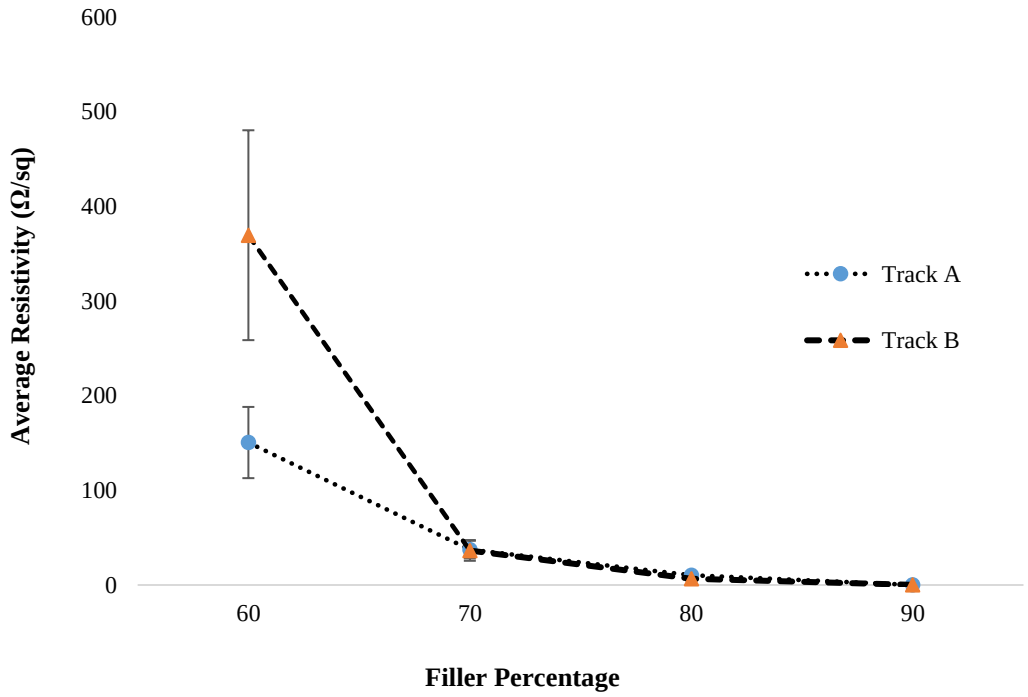

Figure 2: Average sheet resistivity vs filler percentage.

Table 2: Standard deviations of sheet resistivity for different filler percentages.

Filler (%)	Track	Standard Deviation			Overall Standard Deviation
		Point 1	Point 2	Point 3	
60	A	12.16	25.66	101.35	77.82
	B	13.11	59.30	147.68	289.86
70	A	2.70	3.92	5.19	2.69
	B	20.39	4.85	6.31	7.20
80	A	4.67	2.29	4.54	5.29
	B	0.83	0.81	2.56	1.04
90	A	0.04	0.00	0.01	0.08
	B	0.07	0.08	0.03	0.03

The data of estimation of error for sheet resistivity at every measured point is tabulated in Table 3. It is expected that low filler loading produces higher error and vice versa. However, the obtained data shows a random pattern of estimation error. This occurrence is caused by two factors, which are the printing technique and the measurement using the four-point probe. The doctor-blade printing technique requires consistent speed to ensure that the ink is well-distributed in the required gap to produce the ink strips. When the movement speed is too high, it causes ink loss and inaccurately fills the gap (Khirotdin *et al*., 2017). Furthermore, it produces inconsistent thickness of ink, which leads to uneven distribution of ink content as shown in the surface microstructure images in Figures 3 and 4. On the other hand, the measurement using a four-point probe requires delay time for the readings to become stable before they can be recorded. This is due to resistance-capacitance (RC) delay, especially for high resistive samples as the current requires some time to climb up to the saturation value.

Table 3: Estimation of error percentages of sheet resistivity at different filler percentages.

Filler (%)	Average Estimation of Error (%)					
	Track A			Track B		
	1	2	3	1	2	3
60	9.99	21.19	32.24	6.42	17.48	16.24
70	40.48	35.95	35.68	40.63	28.21	40.79
80	50.92	32.12	30.73	27.58	27.44	36.69
90	27.58	0.00	33.33	53.33	31.25	30.56

3.2 Surface Morphology

Morphological analysis was carried out by investigating the surface microstructure images of the ink samples. It is divided into two separated tabulated images, which are the microstructures with no electrical conductivity and microstructures with electrical conductivity. Figure 3 shows the ink microstructure for filler loadings from 10 to 50 %wt that produce no electrical conductivity. In general, the presence of AgNP can be recognised with the formation of dark spots in the microstructure images. For filler loading of 10 %wt, almost no trace of AgNP can be found. The figure portrays light-coloured images, which indicate that the amount of binder and hardener overwhelms the quantity of filler in the composition with the formation of voids. Due to this, it produces no electrical conductivity. Meanwhile, for filler loadings of 20, 30 and 40 %wt, they show scattered existence of AgNP, with these particles portrayed as dark spots in the microstructure images. The frequency of gaps between the silver nanoparticles can affect the electrical properties of the conductive ink layers. The increased gap distance prevents the formation of conductive path and causes the resistance to increase due to the high voltage required to ensure there is a current flow among the AgNP particles (Woo *et al*., 2013). For filler loading of 50 %wt, even though it has the same ratio of filler to the binder, the presence of AgNP is still insignificant. It is represented with very light-coloured microstructure images to indicate the scarce existence of AgNP particles in the composition.

Figure 4 shows the microstructure images for the samples with filler loadings of 60 to 90 %wt that produce electrical conductivity. Based on these images, the samples with filler loadings of 60 to 80 %wt show the presence of granular-like particles on the ink layer. These granular particles contain the 3D connection of conduction, which leads to the existence of particle necking. These particles become conductive although they possess porous characteristic because the growth of the interparticle neck produces the continuous connection between particles (Park *et al.*, 2007). The comparison between these samples of different filler loadings does not display significant difference in terms of microstructure, either for size or shape of the particles.

Filler (%)	Magnifications		
	5x	10x	20x
10	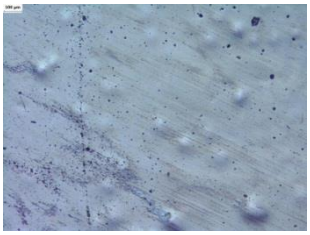	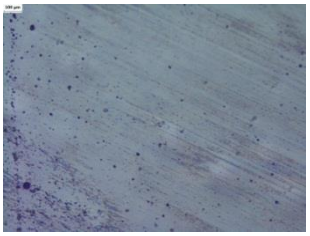	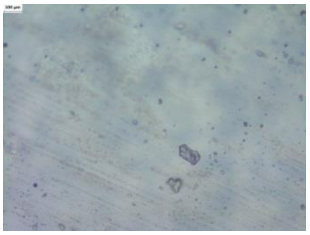
20	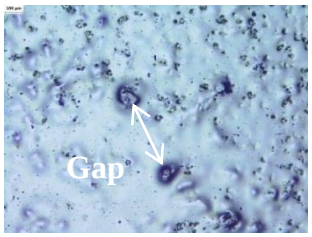	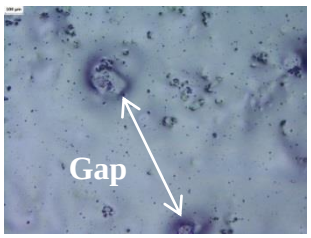	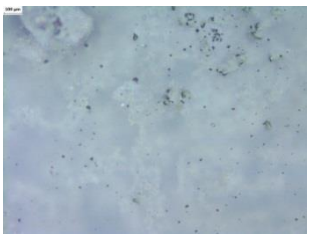
30	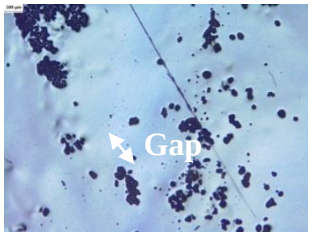	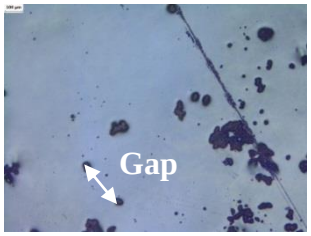	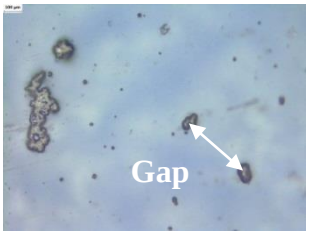
40	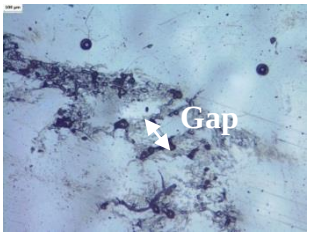	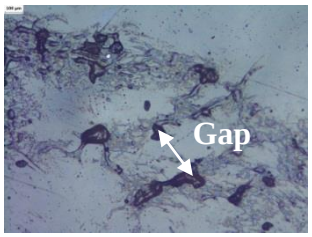	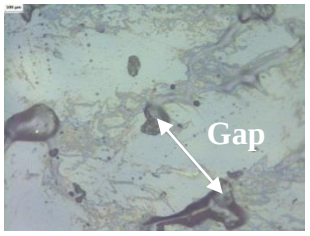
50	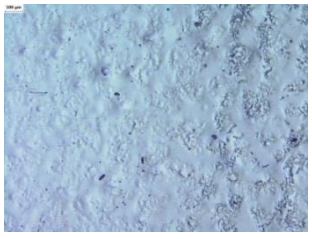	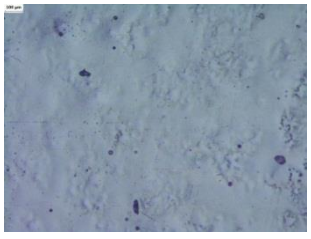	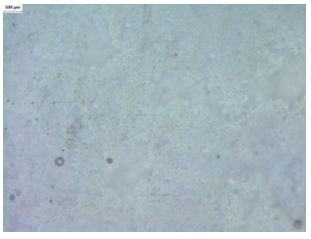

Figure 3: Microstructures with no conductivity.

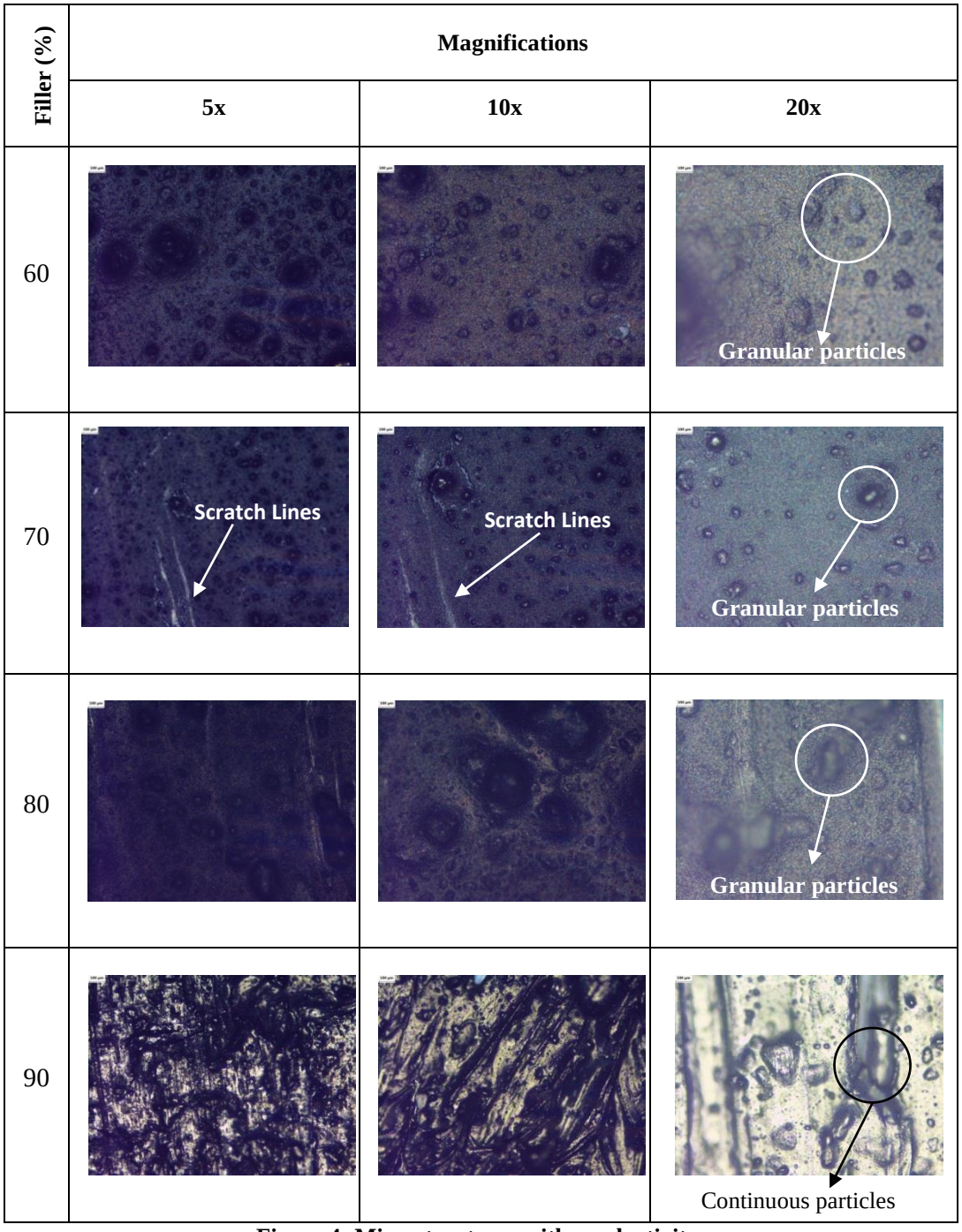

Figure 4: Microstructures with conductivity.

For the filler loading of 70 %wt, it shows evidence of scratch lines on the ink layer surface. This defect is caused by the printing process, where excessive pressure was applied on the razor blade when spreading the ink on the substrate. The filler loading of 90 %wt shows a more obvious presence of AgNP on the ink layer. The increased amount of AgNP creates ink layers with a close-packed structure, where the particles create strong bonding between each other. This is displayed by the continuous particles in the microstructure image to illustrate the contact of particles with each other rather than discrete and spherical shape of particles, which increases the contact area between particles (Zhou *et al*., 2014).

The increase of electrical conductivity because of the increased particle contact area can be described by the percolation threshold. This is because several conducting bridges are formed and an electrical conductivity higher than several orders of virgin polymer is manifested (Khan *et al*., 2019). However, Figure 4 also shows the heterogeneity of AgNP dispersion in the composition. It indicates that the electrical conductivity of the composition can be further improved by forming a more homogenous mixture with a better molecular arrangement (Kulkarni, 2014). One of the methods that this can be done is by improving the annealing process with more suitable operating parameters for the composition. The precise heat addition provides enough molecular energy to form a homogeneous molecular arrangement and prevents agglomeration (Jiang *et al*., 2013).

3.3 Surface Roughness

The measurement of ink layer surface roughness of the samples in this study was conducted for two different movement directions, which were vertical and horizontal directions. The purpose is to eliminate the inconsistency of the obtained data that is sourced from the inaccuracy of the printing technique. Figure 5 illustrates the data and trend of average ink layer surface roughness for the different filler loadings. For the samples with low content of filler loading that do not have the capability to conduct electricity, which are from 10 to 50 %wt, they produce relatively small values of average ink layer surface roughness. The recorded average values are in the range of 0.2 to 0.5 µm. However, with the increment of filler loading starting from 60 %wt, which in the range that the ink composition can conduct electricity, the values of surface roughness increase exponentially. The recorded average values are in the range of 3.5 to 5.5 µm. The increased surface roughness is because of the amalgamation of the AgNP in the composition. The higher amount of AgNP causes more clustering and penetration inside the mixture composition.

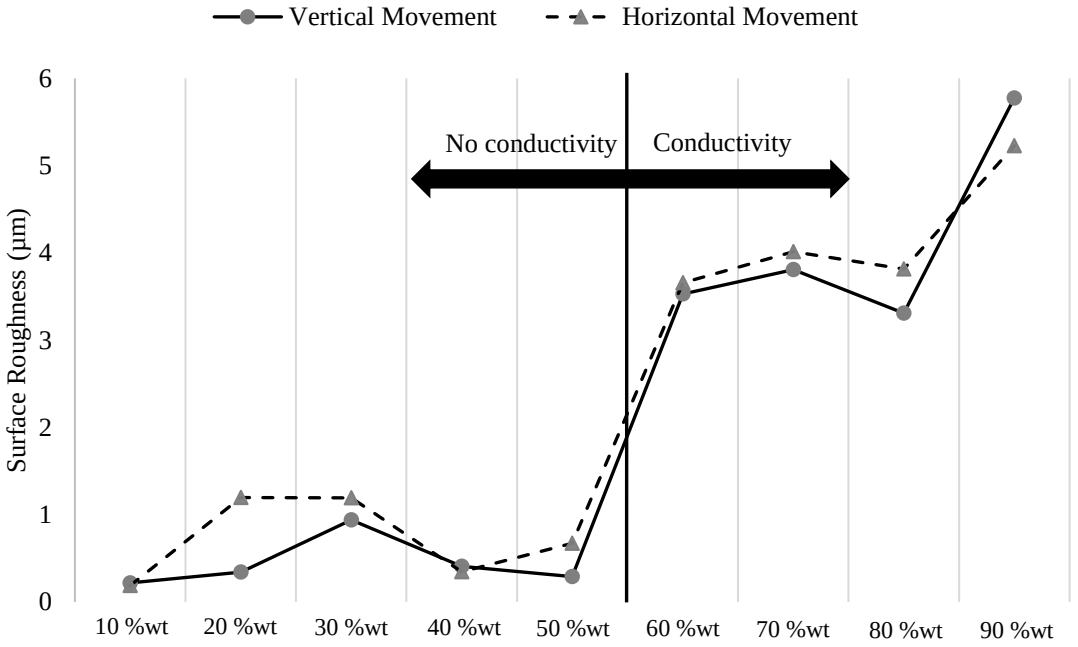

Figure 5: Surface roughness at different filler loadings for horizontal and vertical directions of measurement.

Furthermore, the larger distribution of particle sizes also causes rougher surfaces of the samples (McGrath *et al*., 2021). By referring to Figure 5, the same trend is shown for both the vertical and horizontal directions of movement. This eliminates the influence of inconsistency due to the printing method and the analysis can be solely done on the mixture composition of the ink. Based on the

previous research by Mendez-Rossal *et al.* (2019), there is no direct correlation between surface roughness and electrical conductivity. However, both parameters can potentially be caused by the same source. By focusing on the mixture composition, the results of this study show that higher average surface roughness and higher electrical conductivity are originated from larger distribution of AgNP in the composition.

4. CONCLUSION

The investigation about the resistivity, morphology and surface roughness of silver nanoparticles conductive ink has been conducted. The composition mixture was prepared using a manual mixing process and the doctor-blade technique was chosen as the printing method to form ink tracks on the glass substrate. The correlation between the three investigated parameters was obtained. The minimum required filler loading for the composition to have the ability to conduct electricity is 60 %wt. However, this minimum threshold shows a discrepancy in the tabulated data, which is unacceptable. The resistivity values also reach a plateau with for filler loading of 90 %wt. It indicates that further addition of filler loading is not going to give a significant improvement in electrical conductivity performance.

In terms of morphological analysis, filler loadings of 60 to 80 %wt show the presence of granular particles that contain 3D connection of conduction. This produces the electrical conductivity characteristic. For filler loading of 90 %wt of, it shows the presence of continuous particles that becomes the connecting bridges of higher electrical conductivity capabilities. For the surface roughness analysis, the increment of filler loading increases the surface roughness. Larger distribution of AgNP sizes contributes to higher surface roughness. Based on the results, the usable range of AgNP for conductive ink application is in the range of 70 to 90 %wt. The electrical conductivity performance shows a direct correlation with ink layer surface morphological characteristics but not surface roughness.

ACKNOWLEDGEMENT

The authors would like to thank to the Advanced Academia-Industry Collaboration Laboratory (AiCL) and Fakulti Kejuruteraan Mekanikal (FKM), Universiti Teknikal Malaysia Melaka (UTeM) for providing the laboratory facilities.

REFERENCES

Bose, S., Chakraborty, S. & Sanyal, D. (2018). Water-ethylene glycol mediated synthesis of silver nanoparticles for conductive ink. *Mater Today: Proc.* **5**: 9941–47.

Buszewski, B., Plugaru, V.R., Pomastowski, P. and Sidorenco, A. (2010). *Silver Nanoparticles*. Vukovar, Croatia

Cai, Y., Yao, X., Piao, X., Zhang, Z., Nie, E. & Sun, Z. (2019). Inkjet printing of particle-free silver conductive ink with low sintering temperature on flexible substrates. *Chem. Phys. Lett.*, **737**: 136857.

Chen, Y., Li, Q., Li, C., Dai, Z., Yan, H., Zhu, M., Zhang, Y., Yao, Y. & Li, Q. (2020). Regulation of multidimensional silver nanostructures for high-performance composite conductive adhesives. *Comp. Part A: App. Scie. Manuf.*, **137**: 106025.

Htwe, Y.Z.N., Chow, W.S., Suriati, G., Thant, A.A. & Mariatti, M. (2019). Properties enhancement of graphene and chemical reduction silver nanoparticles conductive inks printed on polyvinyl alcohol (PVA) substrate. *Synt. Met.*, **256**: 116120.

Huang, Q., Shen, W., Xu, Q., Tan, R. & Song, W. (2014). Properties of polyacrylic acid-coated silver nanoparticle ink for inkjet printing conductive tracks on paper with high conductivity. *Mater.*

Chem. Phy., **147**: 550–56.
Ismail, N., Salim, N.A., Naroh, A., Masripan, N.A. Md. Saad, A., Sudin, M.N. & Caridi, F. (2020). Resistivity characterization for carbon based conductive nanocomposite on polyethylene terephthalate and thermoplastic polyurethane substrates. *Inter. J. Nanoelectr. Mater.*, **13**: 315–326.
Ismail, N., Salim, M.A., Naroh, A., Md Saad, A, Masripan, N.A., Donik, C., Omar, G. & Dai, F. (2020). The behaviour of graphene nanoplatelates thin film for high cyclic fatigue. *Intern. J. Nanoelectr. Mater.*, **13**: 305–314.
Jiang, B., Li, M., Yu, H. & Bai, F. (2013). Effect of temperature on the morphology of silver nanoparticles on si substrate in the silver mirror reaction. *ICMREE 2013 - Proc. 2013 Int. Conf. Mater. Renew. Ener. Envir.*, **1**: 140–42.
Farizhandi, A.A.K., Khalajabadi, S.Z., Krishnadoss, V. & Noshadi, I. (2020). Synthesized biocompatible and conductive ink for 3d printing of flexible electronics. *J. Mech. Beh. Biomedic.Mater.*, **110**: 103960.
Khan, T., Irfan, M.S., Ali, M., Dong, Y., Ramakrishna, S. & Umer, R. (2021). Insights to low electrical percolation thresholds of carbon-based polypropylene nanocomposites. *Carbon*, **176**: 602-631.
Khirotdin, R. K., Hassan, N., Siang, H.H. & Zawahid, M.H. (2017). Printing and curing of conductive ink track on curvature substrate using fluid dispensing system and oven. *Engin. Lett.*, **25**: 336–341.
Kosmala, A., Wright, R., Zhang, Q. & Kirby, P. (2011). Synthesis of silver nano particles and fabrication of aqueous ag inks for inkjet printing. *Mater. Chem. Phy.*, **129**: 1075–1080.
Kulkarni, S.K. (2014). *Nanotechnology - Principles and Practices, 3rd Ed,* Springer, Berlin.
Lehtimäki, S., Li. M., Saalomaa, J., Porhonene, J., Kalanti, A., Tuukkanen, S., Heljo, P., Halonen, K. & Lupo, D. (2014). Performance of printable supercapacitors in an RF energy harvesting circuit. *Inter. J. .Elect. Pow. Ener. Sys.*, **58**: 42–46.
Lynch, P.J., Ogilvie, P.S., Large, M.J., Graf, A.A., O'Mara, M.A., Taylor, J., Salvage, J.P. & Dalton, A.B. (2020). Graphene-based printable conductors for cyclable strain sensors on elastomeric substrates. *Carbon* **169**: 25–31.
McGrath, F., Qian, J., Gwynne, K., Kumah, C., Daly, D., Hrelescu, C., Zhang, X., O'Carroll, D.M. & Bradley, A.L. (2021). Structural, optical, and electrical properties of silver gratings prepared by nanoimprint lithography of nanoparticle ink. *Appl. Surf. Sci.*, **537**: 147892.
Mendez-Rossal, H.R. & Wallner, G.M. (2019). Printability and properties of conductive inks on primer-coated surfaces. *Int. J. Poly. Sci.*, **2019**: 3874181
Merilampi, S., Laine-Ma, T. & Ruuskanen, P. (2009). The characterization of electrically conductive silver ink patterns on flexible substrates. *Microelectr. Reliab.*, **49**: 782–90.
Mokhlis, M. Salim, M.A., Masripan N.A., Md.Saad, A., Sudin, M.N., Omar, G. & Caridi, F. (2020). Nanoindentation of graphene reinforced epoxy resin as a conductive ink for microelectronic packaging application. *Int. J. Nanoelectr. Mater.*, **13**: 407–18.
Mou, Y., Wang, H., Peng, Y., Liu, J., Cheng, H., Sun, Q. & Chen, M. (2020). Low temperature enhanced flexible conductive film by ag flake/ion composite ink. *Mater. Des.*, **186**: 108339 .
Park, B.K., Kim, D., Jeong, S., Moon, J. & Kim, J.S. (2007). Direct writing of copper conductive patterns by ink-jet printing. *Thin Sol. Films*, **515**: 7706–7711.
Park, J.Y., Lee, W.J., Kwon, B.S., Nam, S.Y. & Choa, S.H. (2018). Highly stretchable and conductive conductors based on Ag flakes and polyester composites. *Microelectr. Eng.*, **199**: 16–23.
Peng, S.A., Jin, Z., Ma, P., Zhang, D.Y., Shi, J.Y., Niu, J.B., Wang, X.Y., Wang, S.Q., Li, M., Liu, X.Y., Ye, T.C., Zhang, Y.H., Chen, Z.Y. & Yu, G.H. (2015). The sheet resistance of graphene under contact and its effect on the derived specific contact resistivity. *Carbon*, **82**: 500–505.
Rajan, K., Toppola, I., Chiappone, A., Bocchini, S., Perrone, D. & Chiolerio, A. (2016). Silver nanoparticle ink technology: State of the art. *Nanotech. Sci. App.*, **9**: 1–13.
Saad, H., Salim, M.A., Masripan, N.A. Md.Saad, A. & Dai, F. (2020). Nanoscale graphene nanoparticles conductive ink mechanical performance based on nanoindentation analysis. *Int. J. Nanoelect. Mater.*, **13**: 439–448.
Titkov, A.I., Shundrina, I.K., Gadirov, R.M., Odod, A.V., Kurtsevich, A.E., Yukhin, Y.M. & Lyakhov, N.Z. (2018). Thermal and laser sintering of a highly stable inkjet ink consisting of silver nanoparticles stabilized by a combination of a short chain carboxylic acid and a polymeric

dispersant. *Mater. Today: Proc.*, **5**: 16042-16050.
Woo, K., Jang, D., Kim Y. & Moon, J. (2013). Relationship between printability and rheological behavior of ink-jet conductive inks. *Ceramics Int.*, **39**: 7015–7021.
Yunos, A. M., Omar, G., Salim, M.A., Masripan, N.A. & Al-Mola, N.H.A. (2020). The effect of temperature on the electrical conductivity and microstructure behaviour of silver particles. *Int. J. Nanoelect. Mater.*, **13**: 431–438.
Zhou, X., Li, W., Wu, M., Tang, S. & Liu, D. (2014). Enhanced dispersibility and dispersion stability of dodecylamine-protected silver nanoparticles by dodecanethiol for ink-jet conductive inks. *App. Surf. Sci.*, **292**: 537–43.

INVESTIGATION OF POLYURETHENE RESIN PERFORMANCE AS AN INTERLAYER IN LAMINATED GLASS SUBJECTED TO EXPLOSIVE LOADING

Mohammed Alias Yusof[1*], Norazman Mohamad Nor[1], Muhamad Azani Yahya[1], Vikneswaran Munikanan[1], Fakroul Ridzuan Hashim, [1] Arifin Ismail[2] & Ho Chong Choai[3]

[1]Faculty of Engineering, National Defence University of Malaysia (NDUM), Malaysia
[2]Faculty of Management Studies, National Defence University of Malaysia (NDUM), Malaysia
[3]Secuglass Sdn. Bhd., Malaysia

[*]Email: alias@upnm.edu.my

ABSTRACT

This paper investigates the performance of polyurethane resin interlayer in laminated glass subjected to explosive loading. In this research, a total three glass panels, which consisted of one 7.52 mm thick annealed glass panel and two 7.52 mm thick laminated glass panels, were subjected to air explosive with explosive charge weights of 200 and 400 g at a fix standoff distance of 1,500 mm. The blast test results showed that the 7.52 mm thick annealed glass was damaged when subjected to peak overpressure of up to 250 kPa resulting from 200 g of explosive. Meanwhile, the 7.52 mm thick laminated glass with polyurethane resin interlayer survived the peak pressures of 250 and 650 kPa resulting from 200 and 400 g of explosive respectively. The polyurethane resin interlayer successfully retained the glass fragments and reduced the risk of injuries from the glass breakage. The results showed that the laminated glass panel using polyurethane resin as an interlayer has potential to be used as a blast resistant laminated glass panel.

Keywords: *Field blast test; polyurethane resin; annealed glass; laminated glass; explosive loading.*

1. INTRODUCTION

Terrorist attacks on buildings have been a very common terrorist tactic since the 1960s. In most of the bombing attacks, the majority of injuries from bomb blasts have been from flying glass fragments (Cooper & Kurowski, 1996). This can be seen from the attack on the Brussels airport and Maalbeek metro station in Belgium on 22 March in 2016. The attacks were carried out by two suicide bombers at the airport and one on the metro, and killed 32 people, with 340 people injured (The Brussels Times, 2019). The damage to the airport building façade is shown in Figure 1.

Figure 1: Damaged to the airport building façade in Belgium (The Brussels Times, 2019).

There are a number of methods to stop and protect against terrorist attacks, such gathering intelligence on the terrorists and stopping the attack before it takes place. Another way is to protect buildings from damage by incorporating blast resistant material in the building structure and also retrofitting of the existing structure (Mohammed Alias *et al.,* 2013). This area of research is currently receiving more attention from many structural engineers as they begin to consider blast loading and blast resistant materials in their designs in order to protect important buildings and structures from such attacks. Nowadays glass is one of the most popular building materials due to its inherent transparency and aesthetic design. Therefore, the requirement for the residual load bearing capacity of glass structures is very important (Pauli *et al.*,2021). According to the "fail safe approach" by Feldmann *et al.* (2014), in structural glass engineering, in case of partial or total fragmentation of glass, the glass structure has to provide sufficient stiffness and strength, delivering a certain post fracture performance under at least the permanent loads as well as a fraction of the live loads. Annealed glass is often used in windows due to its low cost, but it is a brittle material that offers little resistance to blast waves produced by explosions. When it fails, it breaks into very sharp fragments that can travel at very high velocity and causes injuries. Currently, blast resistant glass used in most buildings is made from laminated glass. Laminated glass is produced from the bonding of at least two sheets of annealed or tempered glass using transparent polyvinyl butyral (PVB) or polymer resin, which is known as interlayer. Mohammed Alias *et al*. (2018). The common architecture of laminated glass is shown in Figure 2.

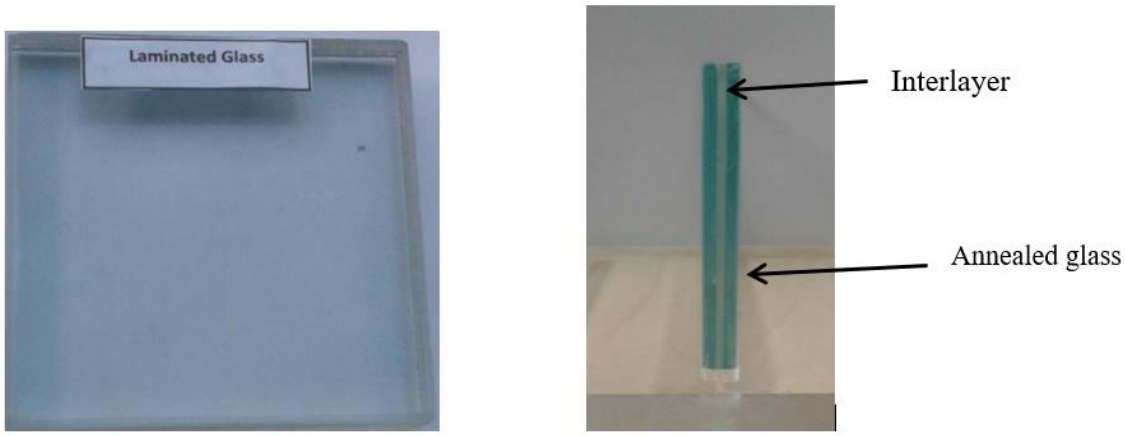

Figure 2: Common architecture of the laminated glass (Mohammed Alias *et al.*, 2018).

Many researchers have carried out studies on the laminated glass using PVB as an interlayer. In a previous study by Larcher *et al.* (2011), they conducted experimental and numerical investigations of laminated glass using PVB under air blast loading. The experiments include both the failure of the glass sheets and PVB interlayer. It is shown that the layered model can adequately reproduce the experimental results, as well as in the cases where the interlayer fails.

Luigi Biolzi *et al.* (2018) investigated on laminated glass under static and impact loading. The structural performance of laminated glass for different glass thickness and interlayers is used in their research. The glass panels used were heat strengthened and tempered glass with PVB interlayer. The static test was performed with a loading system made of four pneumatic jacks attached to the strong floor that was applied to the load. As for the impact test, the researchers used 1 kg of hard and semi-rigid tempered steel ball as the impactor. The impact tests on the laminated glasses were repeated three times at three different contact spots. They found that the PVB interlayer was able to absorb the energy from the impact loading on the glass. Thus, it prevented the laminated glass from breakage due to impact loading.

There is a need to investigate other alternative materials to be used as interlayer in laminated glass, such as polyurethane resin, which can provide resistance to explosive loading. Polyurethane resin is an industrial product that used in the production of many products, such as rubbers and medicines. (Akindoyo *et al.,* 2016).

The objective of this research is to investigate the performance of polyurethane resin as an alternative material to be used as interlayer in laminated glass subjected to explosive loading. In this research, tensile strength measurements for the polyurethane resin interlayer were carried out according to ASTM D638-10: Standard Testing Method for Tensile Properties of Plastic (ASTM, 2010), while field blast tests were conducted on the laminated glass panels according to ISO 16933:2007: Glass in Building: Explosion Resistant Security Glazing Test and Classification for Arena Air Blast Loading (ISO, 2007).

2. METHODOLOGY

In this research, two types of testing were conducted, which are tensile strength of the polyurethane resin and field blast testing. A total of three polyurethane resin interlayer samples were prepared with average size of 120 mm x 20 mm to determine the tensile strength according to ASTM (2010). The dimensions of the polyurethane resin sample is shown in Figure 3.

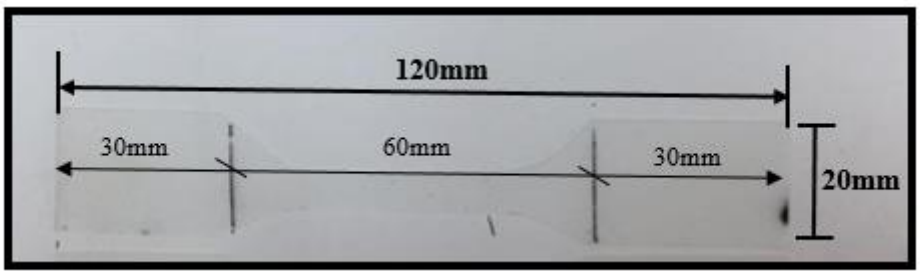

Figure 3 : A sample of the polyurethane resin interlayer.

The tensile strength tests were performed using an INSTRON testing machine with a 5,000 N load cell. The distance between the lower and upper clamp was approximately 60 mm for all the tests. The test setup is shown in Figure 4. The average tensile strength of the polyurethane resin interlayer is 342.68 MPa.

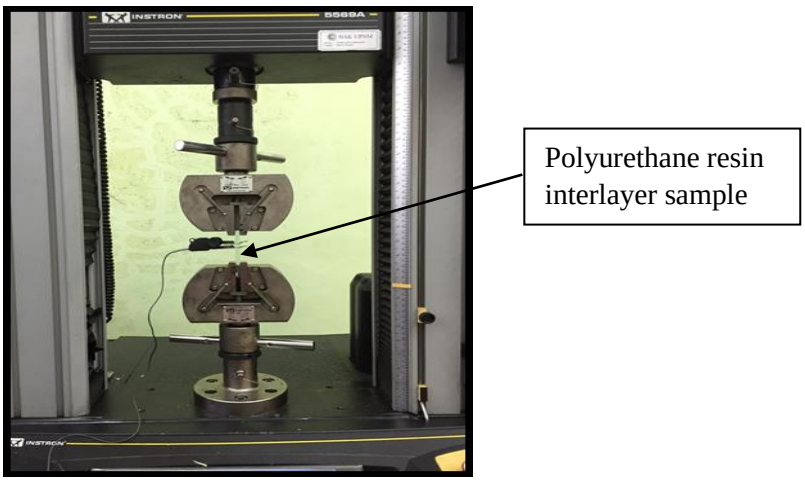

Figure 4: Tensile strength test setup for polyurethane resin interlayer.

A total of three glass panels were obtained from Secuglass Sdn. Bhd., a safety glass manufacturer in Malaysia. The glass panels consisted of one 7.52 mm thick annealed glass panel as a control sample and two 7.52 mm thick laminated glass panels using polyurethane resin as an interlayer. The size of the glass panel was 900 mm x 1,100 mm. Figure 5 shows a laminated glass panel sample used in the experimental works.

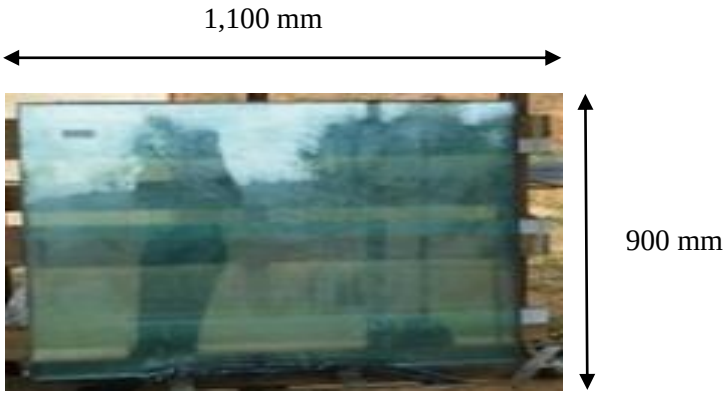

Figure 5: Laminated glass sample used in the experiment.

The field blast tests were conducted according to ISO (2007) at an undisclosed military facility. The panels were fixed to the steel frame testing structure. The blast testing structure in the plan, with size of 1,200 mm x 1,000 mm, was face turned towards the blast. The height of the test frame is 1,500mm. A wooden timber supporting the explosive was erected to hold the charge. The field blast test setup is shown in Figure 6.

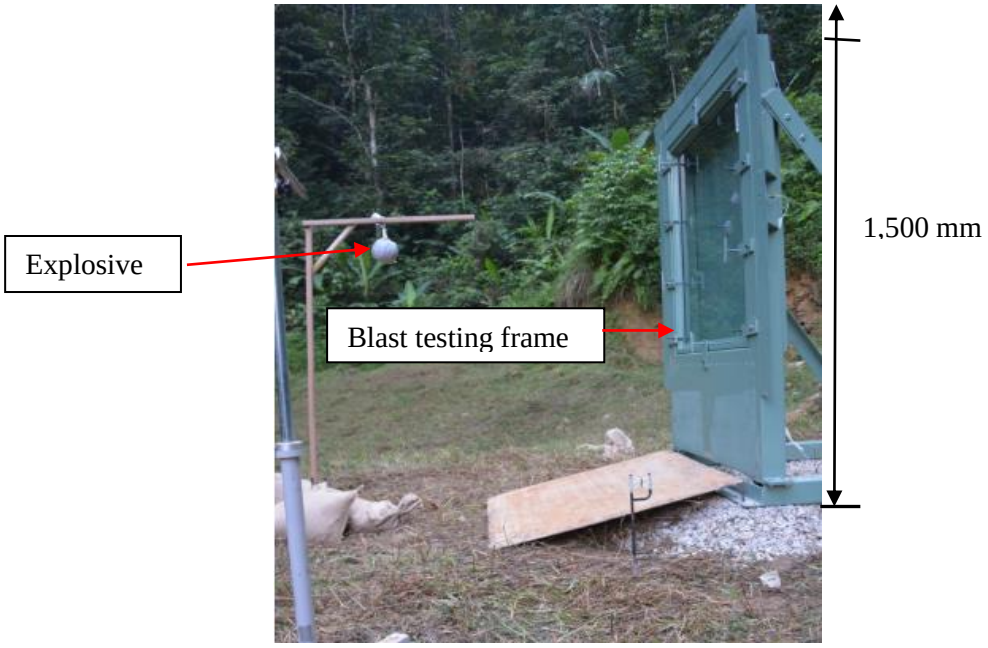

Figure 6: Field blast test setup.

Two Piezoelectric ICP® pressure sensors were used to measure the peak overpressure resulting from the explosion. The sensors were mounted on both sides of the glass panel. The data was captured using a high speed data acquisition system. This system consisted of a data acquisition (DAQ) module and LabVIEW, which was embedded in the computer used to display the blast test results. The schematic layout for the instrumentation used in the field blast tests is shown in Figure 7.

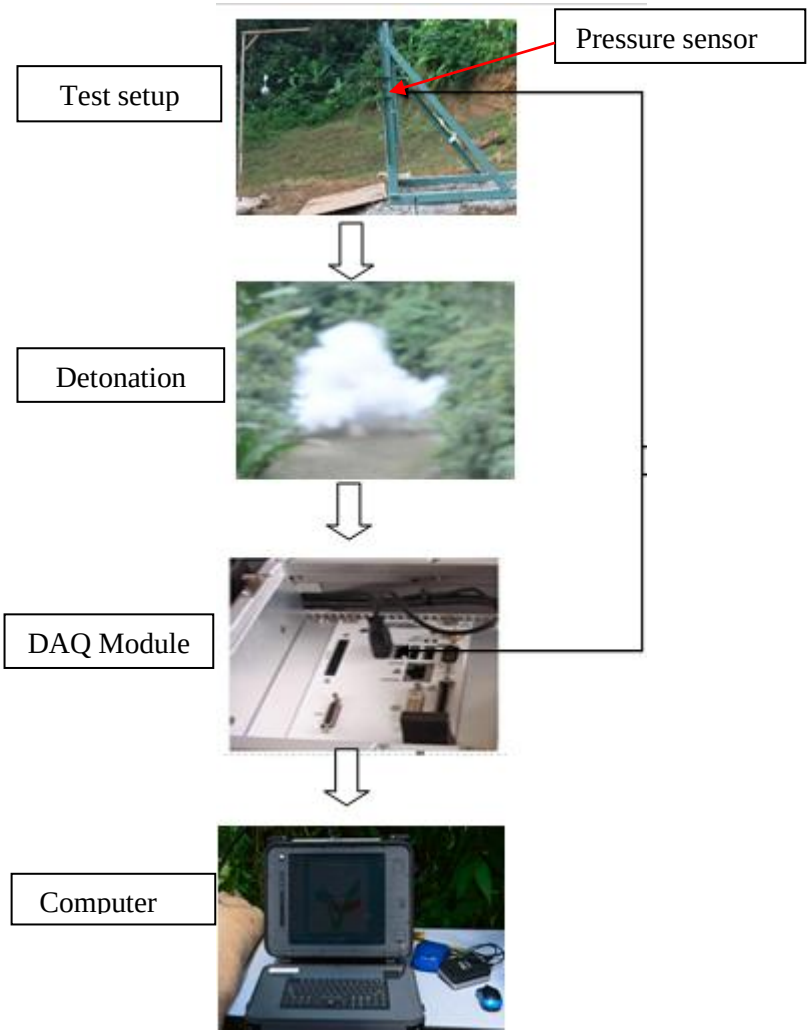

Figure 7: Schematic layout of the instrumentation used in the field blast test.

The annealed and laminated glass panels were tested using explosive charge weights of 200 and 400 g at a fix standoff distance of 1,500 mm. The type of samples and explosive charge weights used in the experiment are summarised in Table 1.

Table 1: Type of glass samples and explosive charge weights used in the field blast test.

Item	Type of sample	Explosive charge weight (g)
Sample 1	Annealed glass	200
Sample 2	Laminated glass	200
Sample 3	Laminated glass	400

3. RESULTS & DISCUSSION

3.1 Sample 1: 7.52mm Annealed Glass Panel Subjected to 200 g of Explosive

Sample 1 is a 7.52 mm thick annealed glass. This sample was used as a control sample. This panel was subjected to 200 g of explosive at a standoff distance of 1,500 mm. Figure 8 shows the pressure time history graph for the sample. From the graph, it was found that the average peak overpressure resulting from the detonation of the explosive is 250 kPa.

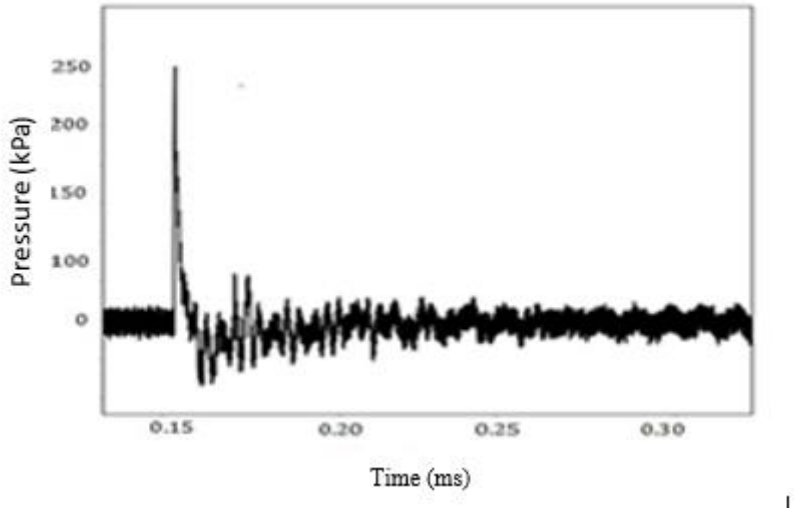

Figure 8: Pressure time history for the 7.52 mm thick annealed glass panel subjected to 200 g of explosive.

From the blast test, it was found that the sample had failed and was broken into pieces. This shows that 7.52 mm annealed glass is not able to withstand blast pressure of 250 kPa resulting from a minimum explosive charge weight of 200 g at a standoff distance of 1,500 mm. This is because annealed glass is a brittle material that possesses very low resistance against the blast loading. Figure 9 shows the damage of the annealed glass panel after the blast test.

Figure 9 : Damage on the annealed glass after the blast test.

3.2 Sample 2: 7.52 mm Laminated Glass Panel Subjected to 200 g of Explosive

Sample 2 is a 7.52 mm thick laminated glass panel with polyurethane resin as an interlayer. This panel was subjected to 200 g of explosive at a standoff distance of 1,500 mm. Figure 10 shows the pressure time history graph for the sample. From the graph, it was found that the average peak overpressure resulting from the detonation of the explosive is 250 kPa.

.

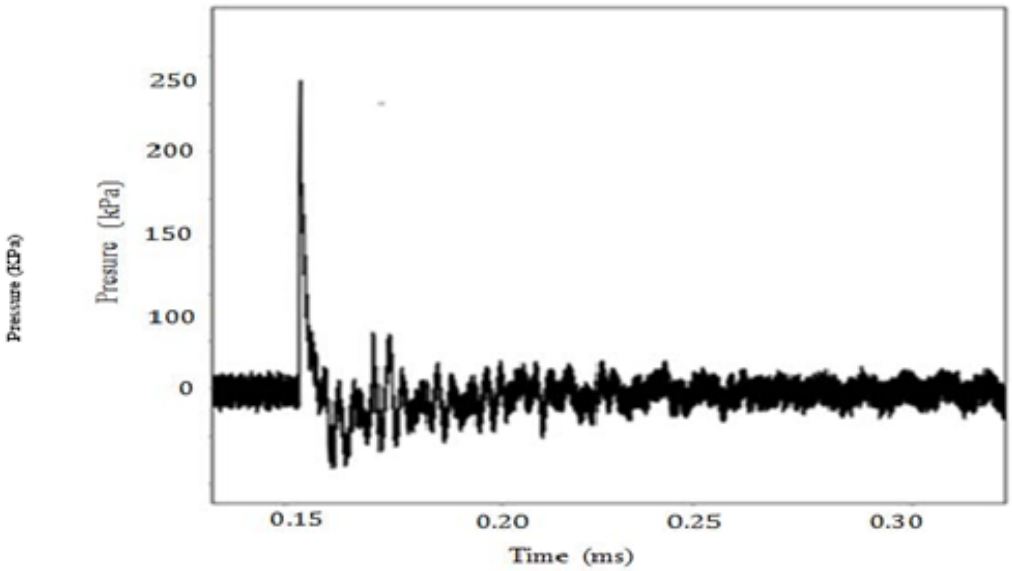

Figure 10: Pressure time history for the 7.52 mm thick laminated glass panel subjected to 200 g of explosive.

From the blast test, it was found that only minor surface cracks were observed at the centre and edge of the panel. The laminated glass remained intact in the frame and there was no perforation observed at the panel. This is because the polyurethane resin as an interlayer managed to hold the glass together and absorb the energy resulting from the explosion of the explosive. Figure 11 shows the cracks of the laminated glass panel after the blast test.

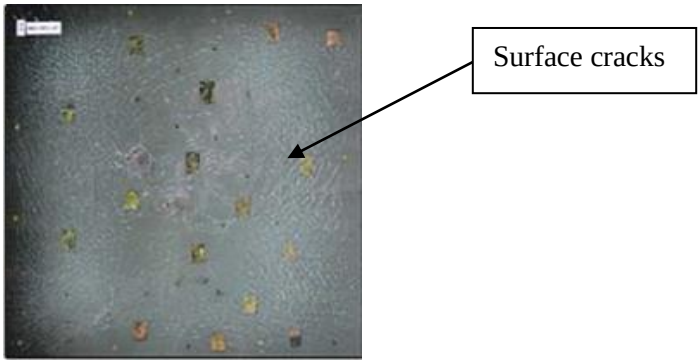

Figure 11: Surface cracks on the laminated glass subjected to 200 g of explosive.

4.3. Sample 3: 7.52mm Laminated Glass Panel Subjected to 400 g of Explosive

Sample 3 is a 7.52 mm thick laminated glass panel with polyurethane resin as an interlayer. This panel was subjected to 400 g of explosive at a standoff distance of 1,500 mm. Figure 12 shows the pressure time history graph for the sample. From the graph, it was found that the average peak overpressure resulting from the detonation of the explosive is 650 kPa.

Sample 3 did not break into pieces after the blast test. This shows that 7.52 mm laminated glass can withstand the blast pressure of 400 g of explosive. Severe radial cracks were observed around the surface of the glass panel. However, there was no perforation on the surface of the glass panel. This shows that the glass panel may have reached its ultimate limit in absorbing the blast energy before it failed. Figure 13 shows the damage on the laminated glass after the blast test.

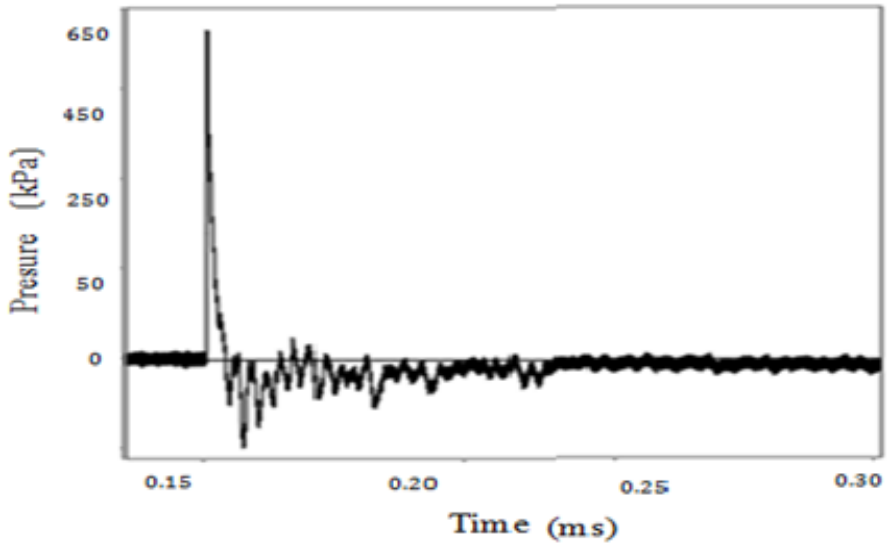

Figure 12: Pressure time history for the 7.52 mm thick laminated glass panel subjected to 400 g of explosive.

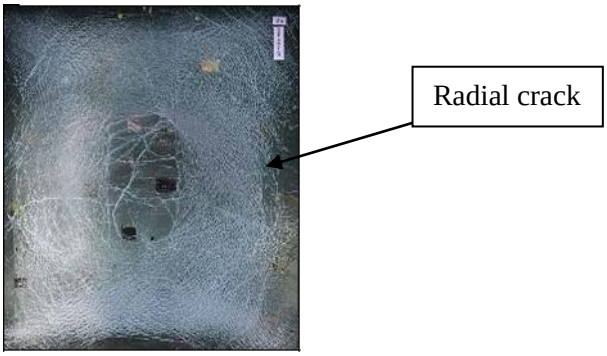

Figure 13: Radial cracks on the laminated glass panel subjected to 400 g of explosive.

5. CONCLUSION

The blast test results showed that the 7.52 mm thick annealed glass was damaged when subjected to blast pressure up to 250 kPa resulting from 200 g of explosive. Meanwhile, the 7.52 mm thick laminated glass with polyurethane resin interlayer survived the blast pressure of up to 650 kPa with severe cracks observed around the surface of the glass panel. However, there was no perforation on the surfaces of the glass panels, which remained intact in the frame. The polyurethane resin interlayer successfully retained the glass fragments, and reduced the risk of cutting or piercing injuries from the glass breakage. The results of this study show that laminated glass using polyurethane resin have the potential to be used as blast resistant glass panels.

ACKNOWLEDGEMENTS

The authors wish to gratefully acknowledge the support from Secuglass Sdn Bhd for providing the laminated glass samples for the testing purposes, as well as the Malaysia Armed Forces (MAF) for providing the blast testing facilities.

REFERENCES

Akindoyo, J.O., Beg, M.D.H., Ghazali, M.D.H., Islam, M.R., Jeyaratnama, N. & Yuvarajc, A.R. (2016). Polyurethane types, synthesis and applications – a review. *RSC Adv.*, **6:** 114453.

ASTM (American Society for Testing and Materials) (2010). *ASTM D638-10: Standard Testing Method for Tensile Properties of Plastic*. American Society for Testing and Materials (ASTM), Pennsylvania, US.

Biolzi, L., Bonati, A. & Cattaneo, S. (2018). Laminated glass cantilever plates under static and impact loading. *Adv. Civil Eng.*, **3**:1-11.

Cooper, P.W. & Kurowski, S.R. (1996). *Introduction to the Technology of Explosives*. Wiley, US.

Feldmann, M., Kasper, R., Abeln, B., Cruz, P., Belis, J., Beyer, J. & Colvin, J. (2014). *Guidance for European Structural Design of Glass Components: Support to the Implementation, Harmonization and Further Development of the Euro Codes*. JRC Scientific and Policy Reports, Ispra, Italy.

ISO (International Organization for Standardization) (2007). *ISO 16933:2007: Glass in Building: Explosion Resistant Security Glazing Test and Classification for Arena Air Blast Loading. International Organization for Standardization* (ISO), Geneva, Switzerland.

Larcher, M., Solomos, G., Casadei, F. & Norbert, G. (2011). Experimental and numerical investigations of laminated glass subjected to blast loading. *Int. J. Impact Eng.*, **39**: 42-50.

Mohammed Alias, Y., Norazman, M.N. & Ariffin, I. (2013). Performance of hybrid steel fibres reinforced concrete subjected to air blast loading. *Adv. Materials Science Eng*, **13**: 1-7.

Mohammed Alias, Y., Norazman, M.N. & Ariffin, I. (2018). *Blast Resistant Material: Concrete and Glass.* UPNM Press, Malaysia.

Pauli, A., Kraus, M.A. & Siebert, G. (2021). Experimental and numerical investigations on glass fragments: shear-frame testing and calibration of Mohr Coulomb plasticity model glass. *Struct. Eng.*, **6 :**65–87.

The Brussels Times (2019). *Inquiry into Brussels Terror Attacks is Complete, but Trial is Some Way Off*. Available online at: https://www.brusselstimes.com/news/belgium-all-news/justice-belgium/59625 (Last access date: 11 June 2021).

QUASI-STATIC INDENTATION BEHAVIOUR OF UNIDIRECTIONAL r-PET / KEVLAR HYBRID LAMINATED COMPOSITES

Nurul Zakiah Zamri Tan[1], Azrin Hani Abdul Rashid[1*], Fatin Nurhidayah Mohd Shaidi[1], Nur Izzati Ibrahim[1], Razlin Abdul Rashid[1], Mohd Yazid Yahya[2], Mohd Yuhazri Yaakob[3] & Risby Mohd Sohaimi[4]

[1]Faculty of Engineering Technology, Universiti Tun Hussein Onn Malaysia (UTHM), Malaysia
[2]School of Mechanical Engineering, Faculty of Engineering, Universiti Teknologi Malaysia (UTM), Malaysia
[3]Faculty of Mechanical and Manufacturing Engineering Technology, Universiti Teknikal Malaysia Melaka (UTeM), Malaysia
[4]Faculty of Engineering, National Defence Universiti of Malaysia (UPNM), Malaysia

[*]Email: azrin@uthm.edu.my

ABSTRACT

This experimental work presents quasi-static indentation (QSI) tests on hybrid laminated composites of unidirectional recycled polyethylene terephthalate (r-PET) strip mats and plain-woven Kevlar fabric as the reinforcer. Silicone sealants were used as the adhesive material for the laminated layers. The hybrid composites were fabricated using hand lay-up and followed by the vacuum bagging technique. The samples were left to cure at room temperature for 24 h. The hybrid laminated composites were prepared in four layering sequences. The non-hybrid composites of full unidirectional r-PET mat and full plain-woven Kevlar fabric were used as reference samples. The QSI tests were carried using a universal testing machine at the speed of 5 mm/min. The energy absorption and maximum indentation force of the hybridising laminated composite structure were studied. The area of force-displacement curves was calculated to demonstrate the hybridisation effects. In summary, this work demonstrates the positive hybridisation effects of those two materials. The results obtained can inspire future applications of high impact energy absorption composites.

Keywords: *Hybrid laminated composites; Kevlar; recycled polyethylene terephthalate (r-PET); indentation responses; energy absorption*.

1. INTRODUCTION

A hybrid composite is a combination of two or more reinforcement materials in the polymer matrix. It is a versatile material that can be a combination of synthetic and natural fibres in the polymer matrix. Hybrid composites have been utilised in many engineering applications to improve mechanical properties as compared to traditional composites. The most used high-performance fibre in hybrid composites is plain-woven Kevlar fabric. It has a unique combination of characteristics that differentiate it from other manmade fibres. Kevlar has superior strength, high modulus and toughness, as well as has good thermal stability. Kevlar reinforced composites usually have high ductility and toughness, which provides advantages to composite systems that require high-speed energy absorption (Pach *et al*., 2021).

The existence of Kevlar has fulfilled the demand of many industries for their advanced technologies. In composite manufacturing, Kevlar gained trust and reputation when NASCAR replaced fibre glass-reinforced plastic with Kevlar in their race car bodies and air dams to avoid leaving debris or shatter after a crash. Kevlar is also widely used in ballistic applications due to its advantages (Reashad *et al*., 2013), including, playing an important role in absorbing and dissipating the impact energy of

ammunition that hits body armours (Yahaya *et al*., 2016). It is still in demand because of its good performance, lightweight and ease to integrate, but its high cost needs to be reduced (Alubel *et al*., 2019). Besides that, Kevlar's production depends on the petroleum sources, whereby it is difficult to manage its waste due to carbon dioxide (Naveen *et al*., 2019). Therefore, hybridisation of fibres is an effective technique to reduce the cost of producing expensive Kevlar (Bulut *et al*., 2016).

Recycled polyethylene terephthalate (r-PET) plastic bottles have come into interest because of their excellent strength and have been applied to many research areas to overcome the global plastic waste problem. The use of the r-PET bottles for impact applications in long strip form seems novel, and its use might be one of the ways to encourage plastic recycling activities. As of today, there are limited studies about the use of wastes, such as r-PET plastic bottles, for hybrid composite, such as in soft body armour. Based on various researches in civil engineering and constructions, r-PET bottles have been extensively used as a reinforcement due to the strength of the bottles (Saikia *et al*., 2014; Khalid *et al*., 2018; Alani *et al*., 2019; Foti, 2019; Perera *et al*., 2019). The use of r-PET bottles for high-end applications could attract people to conserve and take care of the environment by recycling bottles in a proper way. This could also uplift the value of the waste and increase awareness on recycling.

This study presents a hybrid laminated composite with reinforcement made of r-PET bottle and plain-woven Kevlar fabric. Laminated composites and hybrid laminated composites with silicone sealant as the adhesive material were prepared with different layering sequences. Silicone sealant could promote flexibility to the hybrid laminated composite as proven in the study by Kumar *et al*. (2021). Quasi-static indentation (QSI) tests were performed on the hybrid laminated composites to analyse the penetration resistance behaviour and the impact damage of the composite. These tests can also portray the hybridisation effect on the energy absorption behaviour without dynamic impact loading (Pach *et al*., 2021). It is a simpler and cheaper way to be used to present the impact events as compared to low- and high-velocity impact tests (Guled *et al*., 2019; Fotouhi *et al*., 2020). The QSI test and its response is beneficial in the design phase for impact related applications (Guled *et al*., 2019).

Similar studies have been conducted for hybridised laminated composites that consist of Kevlar with other reinforcement materials. It was observed that layering sequence and the placement of reinforcement fibre in outer layers play a significant role in absorbing impact energy and the occurrence of impact damage mechanism of the hybrid laminated structures. The value of energy absorbed during the QSI tests were found to be higher when the Kevlar or aramid fibres were placed in the outer layer and Kenaf fibres were placed in the inner layer of the hybridised composites. This is as the strength of Kevlar in the outer layer (skin layer) resists the formation of shear plug (Yahaya *et al*., 2014; Malingam *et al*., 2018; Feng *et al*., 2020).

Meanwhile the quasi-static indentation behaviour of pineapple leaf and Kevlar fibre reinforced composite demonstrated the potential of hybridisation. It was presented by a comparable indentation property between Kevlar hybrid composite with other materials as the outermost layer and non-hybrid Kevlar fibre reinforced composite. The maximum load and energy absorption were improved by the placement of Kevlar fibre as the outermost layer (Feng *et al*., 2020). Similar trends were shown in studies on hybridisation on kenaf / Kevlar (Malingam *et al*., 2018) and carbon / Kevlar (Guled *et al*., 2019). Quasi-static penetration test of hybrid laminated composites that consist of carbon, Kevlar and S-glass fibres verified that hybridisation techniques presented higher indentation force and energy absorption than non-hybrid composites (Bulut *et al*., 2016).

There have been many studies of Kevlar hybridisation to reduce the weight and cost of the hybrid laminated composites, and it is still ongoing. However, there has been no work reported on the QSI response of r-PET / Kevlar hybrid laminated composites. The aim of this study is to broaden the current knowledge of the behaviour of r-PET / Kevlar hybrid laminated composites that are subjected to QSI tests. The energy absorption, maximum indentation force, specific energy absorption and impact damage of the non-hybrid and hybrid laminated composites were studied.

2. EXPERIMENTAL DETAILS

2.1 Materials

The reinforcement materials used to manufacture the hybrid laminated composite in this study were unidirectional r-PET mats and plain-woven Kevlar fabric, as shown in Figure 1. r-PET bottles which have no pattern or grooves on their surface, were utilised. The bottles were collected before it was dumped into the trash or landfill. Meanwhile, woven Kevlar 29 was supplied by China Beihai Co. Ltd., China. This woven Kevlar fabric has yarn size of 1,100 dtex and the fabric weight is 200 g/m^2. The material properties of the unidirectional r-PET and woven Kevlar fabric are listed in Table 1. The resin used in this analysis is temperature vulcanising (RTV) adhesive silicone sealant SA-107, which serves as an adhesive material. The primary purpose of the silicone sealant is to bind the r-PET mats and Kevlar fabric. SA-107 all-purpose silicone sealant is a single component sealant that offers outstanding adhesion, weathering and elasticity for general glazing and sealing applications. The silicone sealant was supplied by Mohm Chemical Sdn. Bhd., Malaysia.

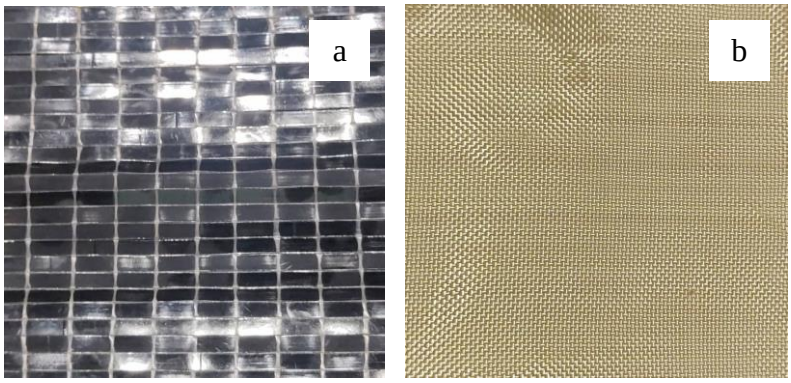

Figure 1: (a) Unidirectional r-PET mat (b) Plain-woven Kevlar fabric.

Table 1: Properties of r-PET strips (Zakiah *et a*l., 2021) and Kevlar fibre (Feng *et al*., 2020).

Properties	r-PET Strip	Kevlar Fibre
Tensile strength (Mpa)	96-126	3000
Tensile modulus (Gpa)	2.41-3.05	124
Strain at break (%)	0.1-1.3	2.5

2.2 Preparation of r-PET Unidirectional Mat

The recycling process of the r-PET bottles was started by collecting plastic bottles and removing the unwanted parts, which are the caps, plastic labels as well as top and bottom sections of the bottles. Then, the bottles were washed to remove any residue and dried. The bottles were cut into a long continuous strips using a bottle cutter. Once the strips were cut into shorter strips, they were straightened using a rod to remove the roll-up. This step is important to produce a flat mat. Unidirectional r-PET mats were produced using a customised device. The unidirectional structure is made using a polyester yarn as warp thread. The use of polyester yarn is inspired from the available unidirectional carbon fibre fabric (Sujon *et al*., 2020). The pegs on the device were used to secure the warp yarn. The initial step to start the unidirectional mat making was to tie the yarn at the first peg. The yarn was then brought through the aligner to the peg at the other side and back up again to the peg at the other side. The aligner was used to ensure that the polyester yarn was placed in the right position. The yarn was warped vertically and tied with a slipknot again to finish. After that, the r-PET was fed horizontally, line by line until the desired size was achieved. As shown in Figure 2, the custom-made device was filled with the r-PET structure to form a mat. All the mat edges were secured with masking tape to avoid the strip from being detached from the mat. In previous reported

researches about weaving r-PET, various technique have been implemented to get good orientation, tight and less porous structures, such as for body of a boat (Idejica, 2019) and concrete (Baciu *et al*., 2020). The method in this research provides neater structure and better dimensional stability than available research.

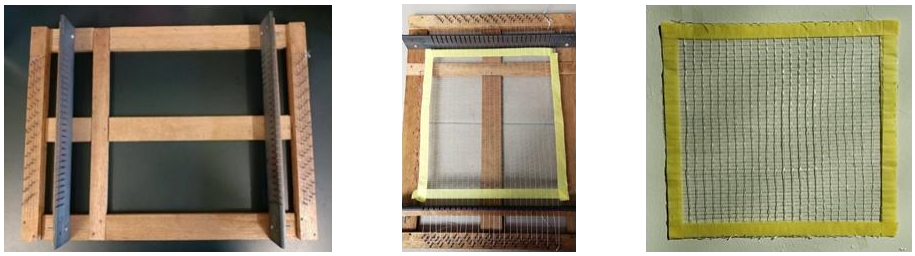

Figure 2: Custom made device to produce unidirectional r-PET mats.

2.3 Fabrication of Hybrid Laminated Composite

Laminates with four types of layering sequences and two control samples were manufactured using the hand lay-up technique. Then, the vacuum bagging technique was adopted because this technique provides better tensile performance than hand lay-up alone (Hidayat, 2018). During the vacuuming process of the hybrid laminated composites, the pressure was maintained at 381 mmHg for 1 h at room temperature. After the vacuum bagging process was completed, the samples were left to cure at room temperature for 24 h. After the curing process was completed, the vacuum hose was disconnected, while the vacuum bag, breather fabric, perforated release film and peel ply were discarded. Finally, the laminates were removed from the mould. The numbers of layers used for the QSI tests were seven for the hybrid laminated composites and six for the control samples. The layering sequences were KPKPKPK, K4P3, PKPKPKP and P4K3 respectively, where K is Kevlar, P is r-PET mat and the numbers denote the number of layers as illustrated in Figure 3. K6 and P6 are the control samples, which consist of full Kevlar fabrics and r-PET mats respectively. The physical properties of the r-PET / Kevlar hybrid laminated composites are summarised in Table 2.

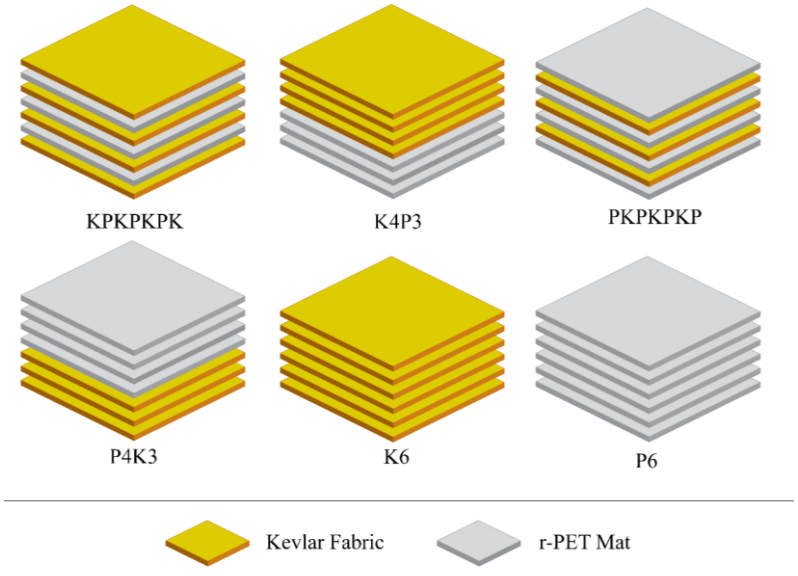

Figure 3: Fibre layering sequences in composite laminates.

Table 2: Physical properties of the hybrid r-PET / Kevlar composites.

Sample configuration	Total layers	Weight (g)	Thickness (mm)	Density (g/mm^2)
KPKPKPK	7	129.55	0.865	0.001
K4P3	7	142.30	0.938	0.010
PKPKPKP	7	135.97	0.911	0.001
P4K3	7	140.31	0.867	0.011
K6 (control)	6	79.72	0.674	0.008
P6 (control)	6	82.26	0.656	0.008

2.4 Quasi-Static Indentation (QSI) Tests

QSI tests on the hybrid laminated composites were carried out to investigate the indentation behaviour. The results of the test were evaluated with regards to maximum indentation force, energy absorption, specific energy absorption and impact damage. The sample dimensions for the QSI tests were 10 mm x 10 mm. The QSI tests were conducted on r-PET / Kevlar hybrid laminated composites with reference to ASTM D6264 using a universal testing machine (Victor). A quasi-static crosshead displacement rate of 5 mm/min was fixed throughout the indentation test. The composite laminates were clamped between the top and bottom support plates using four screws at the corners to avoid any slippage that may affect the accuracy and reliability of the results during the indentation tests. A stainless-steel indenter with a 12.7 mm diameter hemispherical tip was used to perform the QSI tests. The indentation load was applied at the centre of the samples, as shown in Figure 4.

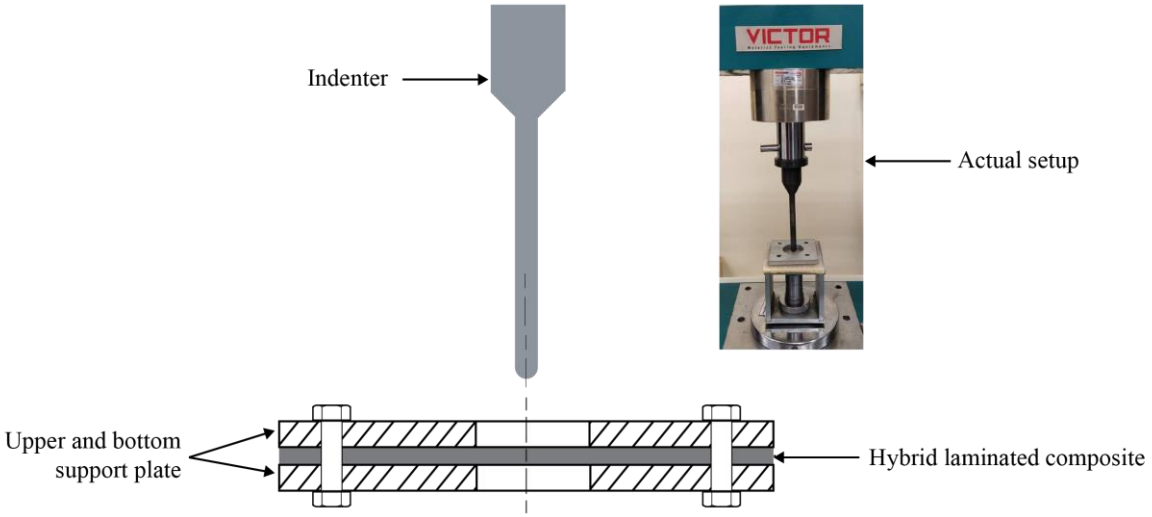

Figure 4: Actual and schematic setups of the QSI tests.

3. RESULTS AND DISCUSSION

3.1 Quasi-Static Indentation Properties

The QSI tests were carried out to compare the indentation resistance of hybrid laminated composites. Energy absorption, E was calculated from the area under the force-displacement curves that were recorded during the tests. Figure 5 demonstrated a very similar trend of force-displacement curves of all the tested laminated hybrid composites.

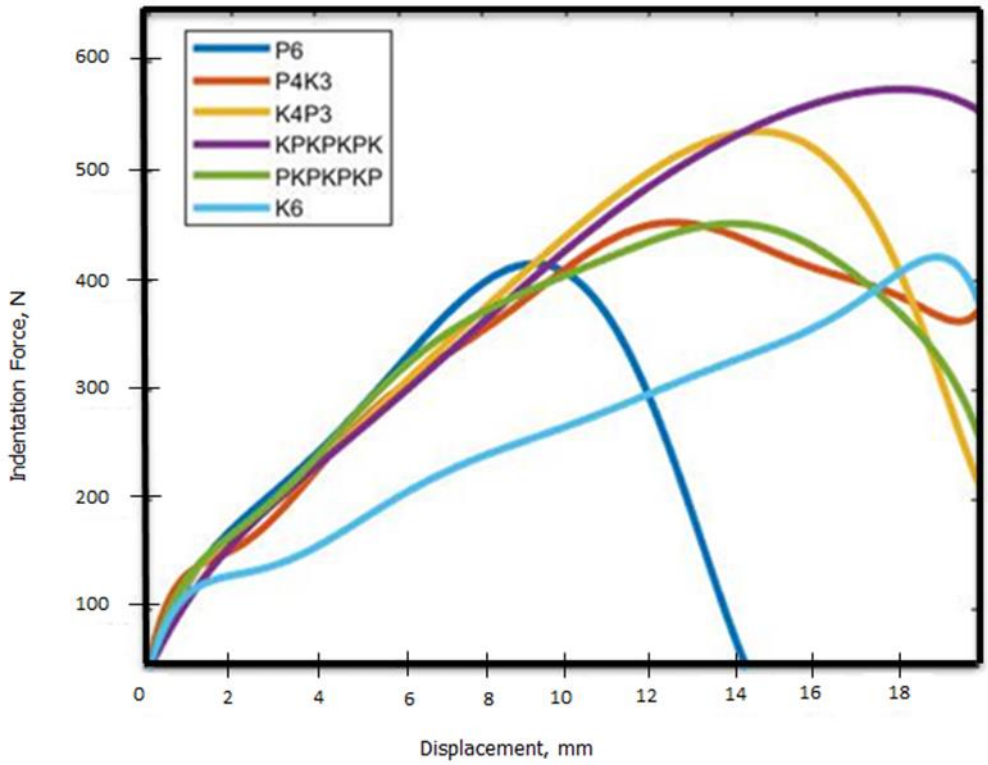

Figure 5: Force-displacement curves of unidirectional r-PET / Kevlar composites.

In general, the behaviour of QSI of the r-PET / Kevlar hybrid laminated composites can be described in three stages (Vella *et al.*, 2014; Bulut *et al.*, 2018). Initially, the early stage is characterised by increased linear behaviour of the loading process with an elastic response of the outer skin layer and the core of the laminates. The second stage is where the laminates were exposed to elastic bending, which led to delamination. The propagation of delamination is increased with the increasing load. Finally, in stage three, the upper skin was punctured to the back skin, which is a complete penetration because of the laminates were under tension. In this study, the curve demonstrated the same trend for all samples.

It is shown in Table 3 that the energy absorption at maximum indentation force (E^{MIF}) and maximum indentation force of hybrid laminated composite KPKPKPK is higher than the full Kevlar composite, K6. The E^{MIF} and maximum indentation force that were recorded for KPKPKPK were 6.86 J and 574.14 N respectively. This layering sequence provides better indentation resistance as compared to other hybrid laminated composite samples. Kevlar as the skin layer was able to resist the perforation of the indenter due to its strength (Yahaya *et al.*, 2014; Malingam *et al.*, 2018; Feng *et al.*, 2020), as well as having better load carrying and energy absorption capability (Hani *et al.*, 2016; Bulut *et al.*, 2018).

Table 3: Indentation properties of the hybrid r-PET / Kevlar composites.

Sample configuration	Maximum indentation force (N)	Total energy absorbs at maximum indentation force (J)	Specific energy absorption at maximum indentation force (J/kg)
KPKPKPK	574.14	6.86	6.51
K4P3	535.67	5.22	4.51
PKPKPKP	452.86	3.71	3.38
P4K3	451.78	4.45	3.96
K6 (control)	421.45	4.82	7.38
P6 (control)	415.52	2.43	3.38

The E^{MIF} and maximum indentation force for K4P3 were 5.22 J and 535.67 N. In contrast, non-hybrid or full unidirectional r-PET composite demonstrated the lowest E^{MIF} and maximum indentation force with the values of 2.43 J and 415.30 N respectively. The advantage of Kevlar as an outer skin layer is proven as the results of composite with r-PET as the outer skin layer shows the lowest values. PKPKPKP have shown to exhibit E^{MIF} of 3.71 J and the maximum indentation force of 452.86 N.

The P6 non-hybrid laminated composite showed the final failure and maximum indentation force at the lowest displacement as compared to the others. This indicates that it has a property of low strain to failure (Farhood *et al*., 2021). The reduction of stiffness may be observed up to the maximum load achieved due to initiation of delamination and fibre ruptures. The enhancement of maximum load was influenced by the tensile and shear properties (Gustin *et al*., 2005; Bulut *et al*., 2018).

Specific energy absorption (SEA) was calculated by dividing the total energy absorption of the laminated composites with their areal density. The highest specific energy absorption was demonstrated by K6 with value of 7.38 J/kg due to its lower mass and density, as well as high specific modules and elongation of break. On the other hand, the SEA of KPKPKPK was 6.51 J/kg. That the SEA of K6 and KPKPKPK are comparable signifies the potential of r-PET as the reinforcement material in hybrid laminated composites and can reduce the usage of expensive Kevlar.

3.2 Damage Assessment

The damage assessment of the reinforced composites was carried out by observing the hybrid laminated composite surface. The impact damage of the front and rear sides of the laminated composites were described in Table 4. From the observation, the delamination of layers is caused by adhesive tearing and local deformations around the indenter. The positioning of r-PET mats and Kevlar fabric in different layering sequences played an important role to the impact damage of the hybrid laminated composites. For example, if the r-PET act as the skin layer, the top and bottom surfaces have a higher degree of damage as compared to those with Kevlar as a skin layer. This was caused by the structure of unidirectional r-PET, which made the indenter able to get through between the adjacent strips of the mat.

No perforation occurred for K6, while P4K3 has perforation on the top side but not on the bottom side. This is different to K4P3, whereby the sample was perforated on the top side. This effect was due to the stiffness of fibres and the placement of r-PET mat and Kevlar fabric in the laminates. The laminated composite that placed Kevlar at the outer or in between layer had evidenced the wedge through phenomenon (Khodadadi *et al*., 2019), whereby the indenter got through between yarns and pulled the yarn further without breaking it. There were a smaller number of broken yarns in the Kevlar fabric. The four long tail lines that were visible on the top surface of KPKPKPK and K4P3 were the strip tensions in weft and warp directions due to the indention force.

The images of all samples showed that the damage area on the bottom side is larger as compared to the top layer. The bulging that occurred at the bottom of all samples was due to the penetration of the indenter. It is clearly shown that serious delamination occurred for KPKPKPK, K4P3 and K6, especially on the top surface. Other samples only displayed slight delamination.

Table 4: Impact damage (front and back) of r-PET / Kevlar hybrid laminated composites.

Composites	Front	Back
KPKPKPK	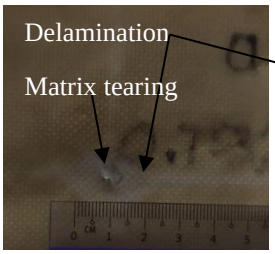	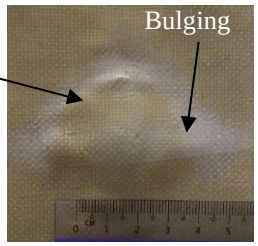
PKPKPKP	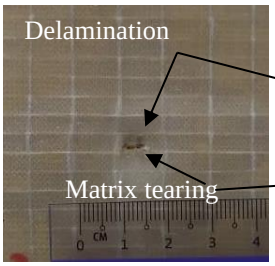	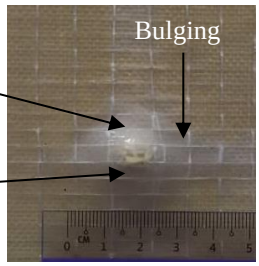
K4P3	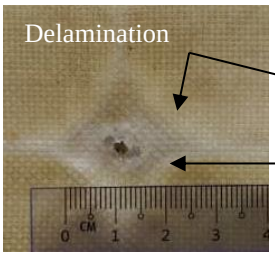	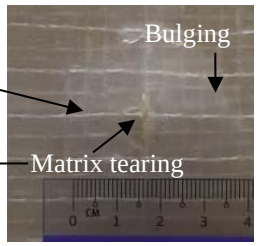
P4K3	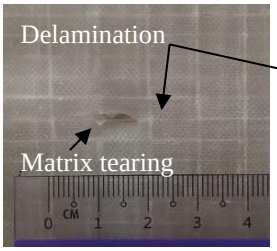	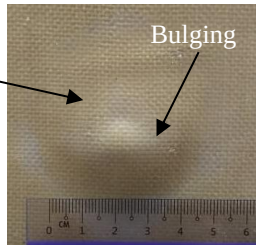
K6	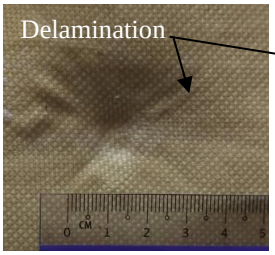	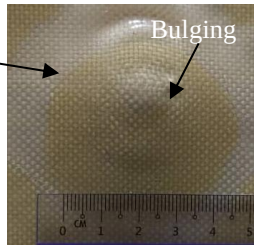
P6	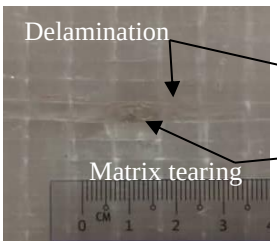	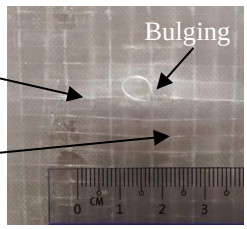

4. CONCLUSION

This research analysed the effect of hybridisation on laminated composites to absorb impact energy. Different stacking sequences of hybrid laminated composites were prepared. R-PET mats and Kevlar fabric were used for reinforcement. According to the QSI test results, it can be concluded that the hybridisation technique using r-PET mats and Kevlar fabric affect the indentation response. The SEA at maximum indentation force shows comparable results between the hybrid laminated composite KPKPKPK and full Kevlar composite K6. This indicates the potential of r-PET to be used as an alternative material for the expensive Kevlar.

From the visual inspection, it was observed that damages, such as delamination, adhesive tearing, bulging, strip pull out and strip stretching occurred due indentation force. Different destructions were observed depending on the type of fibre and placement of it either on the top or bottom of the hybrid laminated composite. Kevlar as a skin layer showed the highest maximum indentation force and energy absorbed. Different types of fibre offers different stiffness, so the sequences of r-PET mats and Kevlar fabric play an important role to the enhancement of the maximum indentation force and energy absorbed. The results of this study are beneficial to design hybrid laminated composites for high impact energy absorption applications, such as the ballistic panel, protective gear, automotive and aerospace.

ACKNOWLEDGEMENT

This research was supported by the Ministry of Higher Education (MOHE) through Fundamental Research Grant Scheme (FRGS) (FRGS/1/2018/TK03/UTHM/02/18) and Collaborative Research Grant (CRG) (vot K036). We also want to thank to Universiti Tun Hussein Onn Malaysia (UTHM) for providing the facilities to conduct this research.

REFERENCES

Alani, A.H., Bunnori, N.M., Noaman, A.T. & Majid, T. A. (2019). Durability performance of a novel ultra-high-performance PET green concrete (UHPPGC). *Constr. Build. Mater.*, **209**: 395–405.

Alubel, M., Boussu, F., Bruniaux, P., Loghin, C. & Cristian, I. (2019). Ballistic impact mechanisms – A review on textiles and fibre-reinforced composites impact responses. *Compos. Struct.*, **223**: 110966.

Baciu, A.M., Kiss, I., Bordeasu, I. & Micu, L.M. (2020). Compressive strength of woven and strand of Recycled Polyethylene Terephthalate (PET) reinforced concrete. *Mater. Plast.*, **57**: 263–271.

Bulut, M. & Erkliğ, A. (2018). The investigation of quasi-static indentation effect on laminated hybrid composite plates. *Mech. Mater.*, **117**: 225–234.

Bulut, M., Erkliğ, A. & Yeter, E. (2016). Hybridization effects on quasi-static penetration resistance in fiber reinforced hybrid composite laminates. *Compos. B Eng.*, **98**: 9-22.

Farhood, N.H., Abdul-Lateef, W. E. & Sultan, K.F. (2021). Quasi-static indentation behaviour of carbon-basalt hybrid cylindrical composites. *J. Mech. Eng. Res. Dev.*, **44:** 189–197.

Feng, N.L., Malingam, S.D., Subramaniam, K., Selamat, M.Z. & Juan, W. X. (2020). The investigation of the tensile and quasi-static indentation properties of pineapple leaf / Kevlar fibre reinforced hybrid composites. *Defence S & T Tech. Bull.*, **13**: 1–13.

Foti, D. (2019). Recycled waste PET for sustainable fiber-reinforced concrete. In *Use of Recycled Plastics in Eco-efficient Concrete,* Woodhead Publishing, pp. 387-410.

Fotouhi, M., Damghani, M., Leong, M.C., Fotouhi, S., Jalalvand, M. & Wisnom, M.R. (2020). A comparative study on glass and carbon fibre reinforced laminated composites in scaled quasi-static indentation tests. *Compos. Struct.*, **245:** 112327.

Guled, F.D. & Chittappa, H.C. (2019). Damage tolerance of carbon and Kevlar based hybrid composites against quasi-static indentation. *Eng. Res. Express*, 1–8.

Gustin, J., Joneson, A., Mahinfalah, M. & Stone, J. (2005). Low velocity impact of combination

Kevlar/carbon fiber sandwich composites. *Compos. Struct.*, **69**: 396–406.
Hani, A.R.A., Azman, N.S., Ahmad, R., Jaafar, M., Roslan, M.N. & Marsi, N. (2016). Ballistic impact response of woven hybrid coir/Kevlar laminated composites. *MATEC Web Conf.*, **78**: 1048.
Hidayat, S. (2018). Influence of the vacuum bag process on the strength of laminate composite. *2018 Int. Conf. Appl. Sci. Tech .(ICAST 2018)*, pp. *754*–757.
Idejica. (2019). *Woven Boat from Plastic Bottles*. Available online at: https://www.instructables.com/Woven-Boat-From-Plastic-Bottles (Last access date: 29 August 2021).
Khalid, F.S., Irwan, J.M., Wan Ibrahim, M.H., Othman, N. & Shahidan, S. (2018). Splitting tensile and pullout behavior of synthetic wastes as fiber-reinforced concrete. *Constr. Build. Mater.*, **171:** 54–64.
Khodadadi, A., Liaghat, G., Bahramian, A.R., Ahmadi, H., Anani, Y., Asemani, S. & Razmkhah, O. (2019). High velocity impact behavior of Kevlar/rubber and Kevlar/epoxy composites: A comparative study. *Compos. Struct.*, **216**: 159–167.
Kumar, V., Alam, M.N., Manikkavel, A., Choi, J. & Lee, D. J. (2021). Investigation of silicone rubber composites reinforced with carbon nanotube, nanographite, their hybrid, and applications for flexible devices. *J. Vinyl Addit. Technol.*, **27:** 254–263.
Malingam, S.D., Feng, N.L., Sean, N.C., Subramaniam, K., Razali, N. & Mustafa, Z. (2018). Mechanical properties of hybrid kenaf / Kevlar fibre reinforced thermoplastic composites. *Defence S & T Tech. Bull.*, **11:** 209–224.
Naveen, J., Jawaid, M., Zainudin, E.S., Sultan, M.T.H. & Yahaya, R. (2019). Evaluation of ballistic performance of hybrid Kevlar®/Cocos nucifera sheath reinforced epoxy composites. *J. Text. Inst.*, **110**: 1179–1189.
Pach, J. & Kuterek, E. (2021). Investigation of the quasi-static penetration resistance behaviour of carbon/aramid fibre-reinforced pp laminate. *Materials*, **14**: 1–17.
Perera, S., Arulrajah, A., Wong, Y.C., Horpibulsuk, S. & Maghool, F. (2019). Utilizing recycled PET blends with demolition wastes as construction materials. *Constr. Build. Mater.*, **221**: 200–209.
Reashad, K. &Nasrin, F. (2013). Kevlar-The Super Tough Fiber. *Int. J. Text. Sci.*,78–83.
Saikia, N. & De Brito, J. (2014). Mechanical properties and abrasion behaviour of concrete containing shredded PET bottle waste as a partial substitution of natural aggregate. *Constr. Build. Mater.*, **52**: 236–244.
Sujon, M.A.S., Habib, M.A. & Abedin, M.Z. (2020). Experimental investigation of the mechanical and water absorption properties on fiber stacking sequence and orientation of jute/carbon epoxy hybrid composites. *J. Mater. Res. Technol.*, **9**: 10970–10981.
Vella, R., Muscat-Fenech, C.D.M. & Mollicone, P. (2014). QSI response of foam-filled composite marine sandwich hull panels: Simulation and experiment. *Procedia Eng.*, **88:** 200–207.
Yahaya, R., Sapuan, S.M., Jawaid, M., Leman, Z. & Zainudin, E. S. (2014). Quasi-static penetration and ballistic properties of kenaf – aramid hybrid composites. *Mater. Des.*, **63:** 775–782.
Yahaya, R., Sapuan, S.M., Jawaid, M., Leman, Z. & Zainudin, E. S. (2016). Measurement of ballistic impact properties of woven kenaf – aramid hybrid composites. *Measurement*, **77:** 335–343.
Zakiah, Z.T.N., Hani, A.R.A. & Reshevarmen, M. (2021). Puncture impact performance of rPET/Kevlar hybrid laminated composite. *AIP Conf. Proc.*, **2347**: 020178.

IDENTIFICATION OF HARMFUL FUNGAL CONTAMINATION IN MOISTURE DAMAGED LABORATORIES

Ahmad Razi Mohamed Yunus*, Noorliza Hamdan, Mohd Badrolnizam Jamhari, Asmariah Jusoh & Noor Hafifi Zuriani Abdul Rahim

Biosurveillance and Biological Defence Branch, Protection & Biophysical Technology Division (BTPB), Science & Technology Research Institute for Defence (STRIDE), Malaysia

*Email: razi.yunus@stride.gov.my

ABSTRACT

This study is aimed at isolating and identifying filamentous fungi from different environmental sources in two laboratories using the molecular technique. The fungal species were isolated from indoor air sampling. The samples were collected from different locations in the laboratories. The isolation of fungi from indoor air was implemented using a *SKC Quick Take 30 sample pump on Malt Extract Agar (MEA) (fungi) plates. Each air sample was collected for 2 min at sampling flow rate of 28.3 L/min. The plates were incubated at 26 ˚C for three to five days, then the fungal colonies were observed and pure cultures were maintained. The identification of fungi at the genus level was carried out using macroscopic examinations depending on the colony colour, shape, hyphae, conidia, conidiophores and arrangement of spores. For the molecular identification of the isolated fungi at the species level, the extracted fungal DNA was amplified by polymerase chain reaction (PCR) using a specific internal transcribed spacer primer (ITS1/ITS4). The PCR products were sequenced and compared with the other related sequences in GenBank (NCBI).The result showed harmful fungi contamination in both laboratories, with five detected in Laboratory A and three detected in Laboratory B (Aspergillus niger, Aspergillus flavus, Aspergillus aculeatus, Penicillium sclerotium, Penicillium sp., Cladosporium sp. and Byssochlamys spectabilis). The results obtained in this study indicate that Laboratory A's exposure to airborne fungi is generally high and not safe for occupants.*

Keywords: *Fungal contamination; airborne; indoor environment; health problems; indoor air quality (IAQ).*

1. INTRODUCTION

Humans in modern society nowadays have been reported to spend at least 80% or more of their time indoors, whether at work or home (Chin & Patricia, 2007). Indoor air quality (IAQ) has become an important public health concern. Among the various indoor pollutants, microbes are the most vital. It has been estimated that one-third of IAQ complaints are due to microbial contamination (Andrew *et al*., 1993). Among the microbial contaminants, fungal growth and contamination in indoor environments have been the focus of recent studies (Chin & Patricia, 2007; Ahmed *et al*., 2020; Brambilla & Sangiorgio, 2020).

Fungi grow and reproduce through spore production. In their lifecycle, fungi also produce chemical by-products, many of which are associated with fungal spores (Chin & Patricia, 2007). Fungal spores are 100 - 1,000 times more numerous than other bioparticles such as pollen grains, and its particulate fraction in bioaerosols being generally 0.3-100 µm in diameter. Fungal spores larger than 10 µm are deposited in the nasopharynx, and can unchain nasal and ocular disorders. In addition, spores and fragments smaller than 10 µm can be transported to the lower airways and lungs, and trigger allergic reactions and infect tissues (Martinez *et al*., 2004; Stetzenbach *et al*., 2004; Ricardo & Joao 2010).

Fungi spread in buildings via ventilation, air outdoor intakes, human movement, building materials and others. Fungal growth and sporulation occur with increase of humidity in the air (Brian *et al*., 2002). Fungi develop and release their spores into the air for dispersal. These fungi produce large quantities of spores that can easily spread over a wide area. Spores also remain dominant for a long period of time during unfavourable conditions (Mebi *et al*., 2012).

A human inhales on average 10 m^3 of air per day, and spends 80 - 95% of their time indoors (Dacarro *et al*., 2003). Airborne microorganisms are scattered everywhere in both outdoor and indoor environments. Many common infections in both humans and animals can be spread by airborne transmission (Shams-Ghahfarokhi *et al*., 2014). Airborne transmission increases the opportunity of human exposure to pathogenic microorganisms by breathing in the polluted air, or through contamination of food and water (Durugbo *et al*., 2012; Fernstrom & Goldblatt, 2013; Erick *et al*., 2016). Airborne fungi is the most important part of human pathogens that cause several human health problems, such as allergic, contagious, infectious and respiratory diseases (Brian *et al*., 2002; Gots *et al*., 2003).

Dampness or moulds in buildings are strongly associated with several allergic and respiratory effects. Based on relevant literature, exposure to airborne microbes in indoor working environments has become a subject of concern due to it potentially affecting the health condition of indoor occupants (Hwang & Yoon, 2016). It has been estimated almost 4.6 million cases (21%) of total asthma cases in the United States may be due to dampness and moulds (Brambilla & Sangiorgio, 2020). The concentration of airborne moulds is influenced by meteorological conditions such as temperature, humidity and moisture (Xeuyan *et al*., 2020).

The morphology of a fungal colony in filamentous fungi results from growing as fibres (hyphae) that are cylindrical and threadlike, with structure diameters of 2 to 10 μm and length of up to several centimetres. They have different observations of colony features, such as colour, size and shape visible to the naked eye, which is used classically to identify fungi (Ferreti De-Lima & De-Moraes-Borba, 2001). The morphology of fungi is observed under a compound microscope to examine the shapes forming from the arrangement of spores (Gaddeyya *et al*., 2012). The morphological and biochemical identifications of fungi sometimes face many problems, including time consuming, requires high skill, and generates various morpho / biotypes within one species. The use of molecular identification is fast, sufficient, reproducible, and can provide high specificity to distinguish between species and subspecies of fungi, unlike morphological and biochemical tests used in laboratory diagnosis of fungi (Liu *et al*., 2000; Takashi & Akemi, 2003).

Molecular identification techniques based on total fungal DNA extraction provide a unique barcode for the determination and identification of different fungal isolates up to a species level (Landeweert *et al*., 2003). Molecular identification using this barcode has become an essential tool for mycologists studying fungal taxonomy, molecular evolution, population genetics and fungus-plant interactions (Evelyn *et al*., 1992). The identification of fungi using molecular techniques is carried out through the sequencing of polymerase chain reaction (PCR) amplified parts of 18S rRNA genes with universal primers to fungal species (Henselt & Holden, 1996; William *et al*., 2005).

A laboratory can usually be referred to as a space room or building equipped for scientific research and also to carry out any testing of chemicals, biological and physical materials. A clean and optimum indoor environment of the laboratory is crucial to ensure the well-being of the occupants and also to maintain all the expensive instruments, materials and samples in good condition (Yau *et al*., 2012). The microbial compositions from indoor environment in various types of biological laboratories are less well understood (Hazrin *et al*., 2015; Xi *et al*., 2018). Lab workers, especially personnel handling microbiological work, would be more exposed to bioaerosols than those in other occupations. Most laboratory workers feel that they are safer when standard safety practices are applied, but evidence-based research is lacking to confirm this supposition (Hwang & Yoon, 2016). Xi *et al*. (2018) reported that both environmental and human factors are important in shaping the diversity and dynamics of these possible microbial contaminations in biological laboratories.

This study was performed in two different locations for sampling (two laboratories) in October 2019. The laboratories for this study were Laboratories A and B, which are in the same building. These two laboratories started their operations in 2013. Laboratory A is used to carry out biological tests and analysis, while, Laboratory B is used to test and analyse chemical samples. Both laboratories share the same air conditioning systems, which have not been operated since July 2019.

2. MATERIALS AND METHODOLOGY

2.1 Collection of Samples

At each site, a series of air samples in triplicate were collected on Malt Extract Agar (MEA) (fungi) plates using a BioStage® single stage viable cascade impactor attached to a SKC Quick Take 30 sample pump. Each air sample was collected for 2 min at a sampling flow rate of 28.3 L/min (NIOSH, 1998). The sampling pump with representative sampler in line was calibrated before each use using a rotameter, with the impaction aperture cleaned with sterile alcohol wipes between sampling events to minimise cross contamination between locations. The samples were transported promptly to the laboratory. The samples were then assessed for growth of viable fungi and incubated at 25 ˚C for three to five days.

2.2 Isolation of Fungi

After incubation, each fungal colony samples were taken from the plates and transferred into potato dextrose agar (PDA) medium with streptomycin. The cultures were incubated at 26 ˚C in the incubator for three to five days. The fungal colonies were observed, and the pure cultures were maintained (Gaddeyya *et al*., 2012; Javadi *et al*., 2012; Jasuja *et al*., 2013).

2.3 Macroscopic and Microscopic Examination of Isolated Fungi

The fungal morphology was studied macroscopically by observing the colony features (colour, shape, size and hyphae), and microscopically by a compound microscope with a digital camera using a lactophenol cotton blue stained slide mounted with a small portion of the mycelium (Gaddeyya *et al*., 2012).

2.4 Molecular Identification of Fungal Species

2.4.1 DNA Extraction and PCR Amplification

The DNA extraction of genomic DNA from the fungi was conducted from the PDAs culture using Nucleospin Plant II Kit (supplied by Macharel Nage). The fungal ribosomal internal transcribed spacer (ITS) region was amplified using universal primers ITS1 and ITS4. The total reaction volume of 25 µl contained gDNA purified using commercial kit following the manufacturer's protocol, 0.5 pmol of each primer, 200 uM of deoxynucleotides triphosphates (dNTP), 0.5 U/l of DNA polymerase, the supplied PCR buffer and water. The PCR was performed as follow: one cycle (98 °C for 2 min) for initial denaturation; 25 cycles (98 °C for 15 s; 60 °C for 30 s; 72 °C for 30 s) for annealing and extension; and one cycle (72 °C for 10 min) for the final extension of the amplified DNA.

2.4.2 Sequencing and Analysis

The PCR products were purified using the Nucleospin Gel and PCR clean-up kit (Bao *et al*., 2012). The PCR products were purified using the standard method and directly sequenced using the BigDye® Terminator v3.1 cycle sequencing kit (Applied Biosystems). The obtained sequences were compared with the other related sequences using the BLAST search in GenBank (NCBI) (Liu *et al*., 2000; Landeweert *et al*., 2003; Javadi *et al*., 2012).

3. RESULTS

Four different genera, which are Aspergilllus, Penicillium, Clasdosporium and Byssochlamys, as well as five fungi species were isolated and identified. The prevalence of the identified fungi is shown in Table 1. The most prevalent and distributed species of culturable fungal type found in this study was *Aspergillus niger*. It was isolated from both locations, while other species were isolated from only one location.

Table 1: Distribution of the isolated species from different locations.

Species/Locations	Laboratory A	Laboratory B
Aspergillus niger	+	+
Aspergillus flavus	-	+
Aspergillus aculeatus	+	-
Penicillium sclerotium	+	-
Penicillium sp	+	-
Cladosporium sp.	-	+
Byssochlamys spectabilis	+	-

+: present -: absent

3.1 Macroscopic Features of the Isolated Fungi

In this study, the isolated fungi were examined on the basis of cultural and microscopic characteristics. Figures 1 - 7 show the colony morphology of the isolated and identified fungal species.

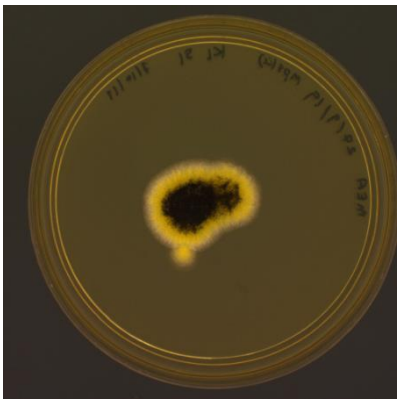

Figure 1: *Aspergillums niger* colony features on PDA.

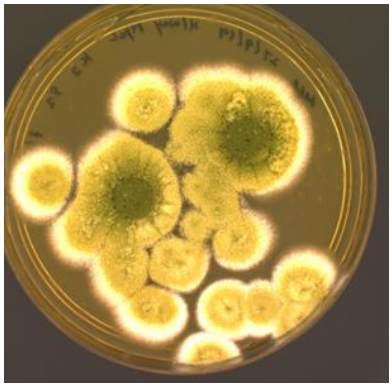

Figure 2: *Aspergillus flavus* colony features on PDA.

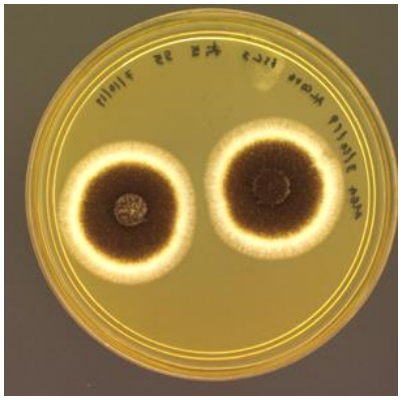

Figure 3: *Aspergillus aculeatus* colony features on PDA.

Figure 4: *Penicillium sclerotium* colony features on PDA.

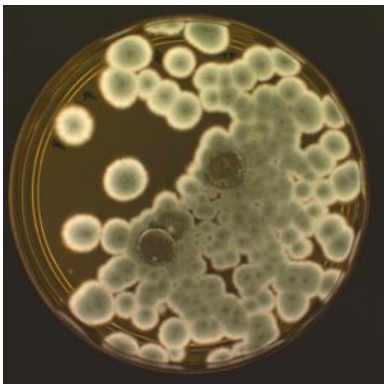

Figure 5: *Penicillium sp.* colony features on PDA.

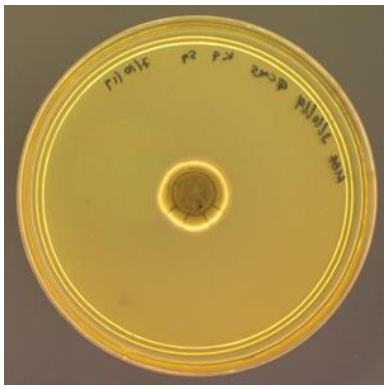

Figure 6: *Cladosporium sp.* colony features on PDA.

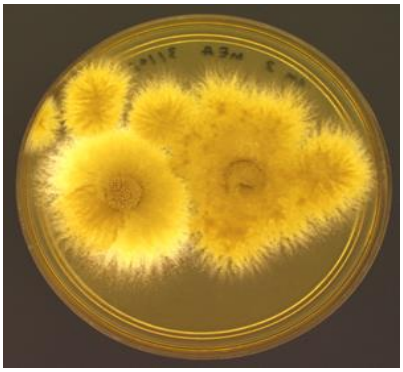

Figure 7: *Byssochlamys spectabilis* colony features on PDA.

3.2 Microscopic Features of the Isolated Fungi

The isolated fungi were also examined microscopically. Figure 8-11 show the microscopic features of four fungal species that were isolated and identified in this study.

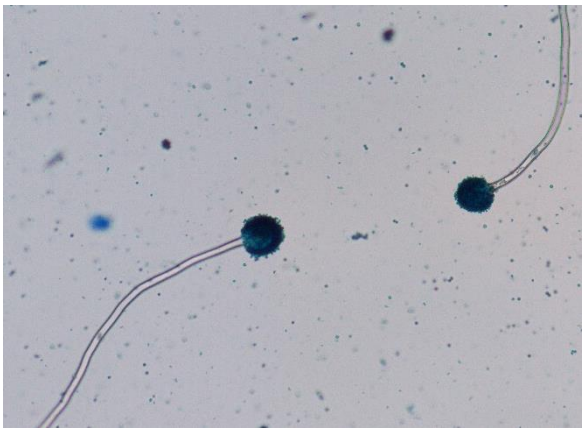

Figure 8: The conidia arrangement of *Aspergillus niger*

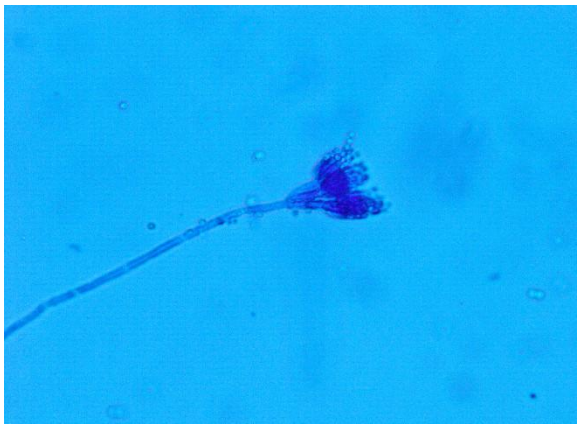

Figure 9: The phialospores of the *Penicillium sp.*

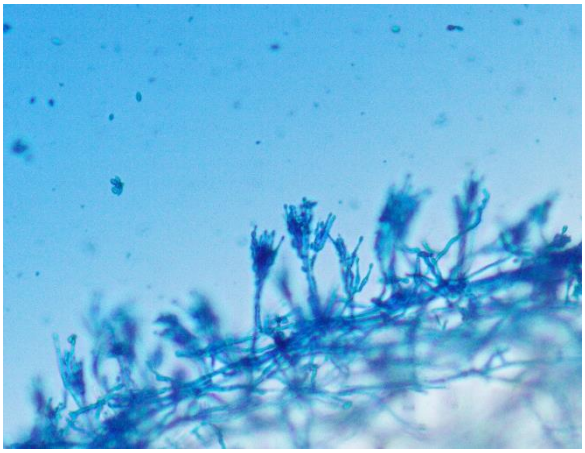

Figure 10: The phialospores of *Penicillium scelotium.*

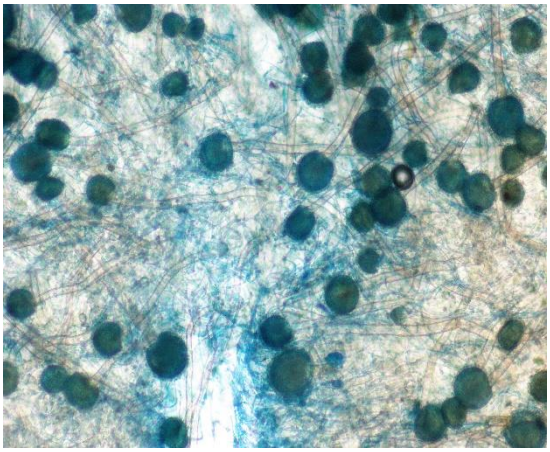

Figure 11: The conidia arrangement of *Aspergillus flavus*

3.3 rDNA Sequences Analysis

The ITS regions of the rDNA sequences are shown in Table 2. The sequence analysis of the ITS regions of the nuclear encoded rDNA showed significant alignments of 97 to 99% for the isolated fungal species.

Table 2: Identification of fungal isolates of ITS regions of the rRNA gene sequences.

Isolate	Species Identified	Length (bp)	Identity
K12S12 & K1S1 (A&B)	***Aspergillus niger***	700	100%
K2S2 (B)	***Aspergillus flavus***	700	98.3%
K5S5 (A)	***Aspergillus aculeatus***	700	100%
K11S11 (A)	***Penicillium sclerotium***	700	99.83%
K4S4 (A)	***Penicillium sp***	700	100%
K9S9 (B)	***Cladosporium sp.***	700	100%
K8S8 (A)	***Byssochlamys spectabilis***	700	100%

**A: Laboratory A B: Laboratory B*

4. DISCUSSION

This study was carried out to identify fungi isolated from indoor air from Laboratories A and B using morphological and molecular analysis methods. Seven fungal species were isolated and identified using macroscopic and microscopic features through morphological analysis, while molecular analysis at the species level were conducted using rDNA ITS sequence comparison and analysis. The molecular identification was carried out using DNA barcoding with ITS region sequencing. The ITS rDNA sequences were compared to those in the databases using NCBI-BLAST. Seven species were identified using DNA barcoding with an identity range between 98 - 100%. As ITS rDNA region sequencing is one of the most important tools for the identification of the fungal species isolated from environmental sources, hence, it has been widely used to detect environmental fungal community, and is as an improvement from classical identifications. ITS rRNA genes are excellent candidates for the phylogenetic analysis because they are universally distributed, functionally constant, sufficiently conserved, and of adequate length to provide a deep view of evolutionary relationships (Anderson & Parkin, 2007).

Most fungi present indoors come from outdoors (Horner *et. al*, 2004). Another source is indoors itself, whereby fungi can grow in building materials, foodstuffs, flower pots, pet bedding materials and house dust (Ricardo & Joao, 2010). Fungi growth in building materials is more dependent on the moisture content of the substrate than on atmospheric relative humidity. The minimum moisture content of building materials allowing fungal growth is near 76% (for atmospheric relative humidity, this value is near 82%). All fungi need nutrients for growth and sporulation. When growing indoors, substrates such as food and nutrients are not limited, but on the surface of certain building materials, nutrients may limit fungal growth (Ricardo & Joao, 2010).

Penicillium is widely distributed and its spores are common in air samples. Members of the genus Aspergillus are also common in the environment and often found contaminating other cultures. Both Penicillium and Aspergillus are frequently encountered in microbiological studies of buildings. In a large study of buildings and outdoor environments in the United States, Penicillium and Aspergillus ranked among the most common culturable airborne fungi in all seasons and across all regions tested (Brian *et al*., 2002). These two moulds are abundant in indoor and outdoor samples from homes free of water damage (Horner *et al*., 2004).

The majority of Aspergillus and Penicillium species are xerophilic and able to growth in substrates with water activity lower than 0.80 Aw. Xerophilic fungi are well adapted to indoor environments, since these fungi grow and sporulate with low atmospheric relative humidity and substrates with low moisture content. Indeed, most of other indoor fungi (namely Cladosporium, Stachybotrys, Chaetomium, Trichoderma and Ulocladium) are much less tolerant to xerophilic conditions (Anna *et al*., 1992). Due to their low water activity requirements (compared with bacteria), fungi are the principal contaminant in various types of indoor substrates. They tend to colonise a wide variety of humid building materials wetted by floods or plumbing leaks (Dacarro *et al*., 2003).

The study by Ahmed *et. al* (2020) found three fungi genera Aspergillus, Penicillium and Alternaria in the Biological Laboratory Room, with Aspergillus having the highest occurrence frequency, followed by Penicillium. The dominant fungal genera in this area were Aspergillus and Penicillium due the ability of their spores to easily spread in various aerobic environments. Aspergillus is characterised by the production of small conidial spores that are widespread in air environment in tropical regions. Many studies have reported elevated concentrations of fungi in air samples of some critical indoor environments. Particularly, high frequency levels of *Aspergillus sp.*, *Cladosporium sp.* and *Penicillium sp.* were recorded by Pavan & Manjunath (2014), Tong *et al*. (2017), Gonnalves *et al*. (2017) and Joana *et al*. (2014).

Aspergillus, Penicillium and Alternaria are allergenic fungi that can colonise in indoor environments and thereby increase fungi exposure levels. Human exposure to fungal aeroallergens can cause an increase in asthma severity (Gabriel *et. al*, 2016). Penicillium and Aspergillus are widespread in

outdoor and indoor environments and thus, they are generally considered as contaminants (Davise, 1995). This is not to say that species of these genera are completely innocuous. Penicillium spp. may cause a variety of infections, while Aspergillus spp. is associated with a range of health problems from allergies to invasive infections (Davise, 1995).

5. CONCLUSION

The isolation and identification of filamentous fungi from Laboratory A displayed the presence and abundance of some pathogenic fungi. The results obtained in this study indicate that exposure to airborne fungi is high and not safe for laboratory workers. The information obtained from the fungal air samples can assist in medical evaluations, determination of remediation procedures as well as assessment of health hazards, and can be useful in proactive indoor air quality monitoring.

REFERENCES

Ahmed, K.A., Mohamed, H.A., Raed, A. & Saleem, E. (2020). Assessment of airborne fungi in indoor environment for biological lab rooms. *J. Pure Appl. Microbiol.,* **13**: 2281-2286.

Anna, L.P., Juutinen, T., Matti, J.J. & Pentti, J. K. (1992). Occurrence and moisture requirements of microbial growth in building materials. *Int. Biodeterior. Biodegrad.*. **30**: pp. 273–283.

Anderson, I.C. & Parkin, P.I. (2007). Detection of active soil fungi by RT-PCR amplification of precursor rRNA molecules. *J. Microbiol. Method.,* **68**: 248-253.

Andrew, M.P., Roy, P. & Harriet, B. (1993). *Indoor Allergens*. National Academy Press, Washington DC, US.

Bao, Z., Ikunaga, Y., Matsushita, Y., Morimoto, S., Takada-Hoshino, Y., *et al*. (2012). Combined analyses of bacterial, fungal and nematode communities in Andosolic agricultural soils in Japan. *Microbes Environ*., **27**: 72–79.

Brambilla, A. & Sangiorgio, A. (2020). Mould growth in energy efficient buildings. *Energy Rev.,* **132**: 110093.

Brian, G.S., Kimberly, H.K., Dana, W.F. & George, K.M. (2002). Profiles of airborne fungi in buildings and outdoor environments in the United States. *Appl. Environ. Microbiol*, **68**:1743-1753.

Chin, S.Y. & Patricia, H. (2007). *Sampling and Analysis of Indoor Microorganisms*. John Wiley & Sons, New Jersey, US.

Dacarro, C., Picco, A. M., Grisoli, P. & Redolfi, M. (2003). Determination of aerial microbiological contamination in scholastic sports environment. *J. Appl. Microbiol.*, **95**: 904-912

Davise, H.L. (1995). *Medically Important Fungi: A Guide to Identification, 3rd Ed*. ASM Press, Washington, D.C., US.

Durugbo, E.U., Kajero, A.O., Omoregie, E.I. & Oyejide, N.E. (2012). A survey of outdoor and indoor airborne fungal spora in the Redemption City, Ogun State, southwestern Nigeria. *Aerobiologia*, **29**: 201–216.

Erick, O.M.H., Maria, G.F.D.L., Esperanze, D.E., Carmen, C.E., Maria, C.J.M., Gustavo, A.A., Facundo, R.B., Conchita, T. & Maria, R.R. (2016). Fungal diversity and Aspergillus species in hospital environments. *Ann. Agric. Environ. Med.*, **23**: 264–269

Evelyn, M.M., Gunter. B., Heinrich. S. & Hartwig, H.G. (1992). A simple and efficient protocol for isolation of high molecular weight DNA from filamentous fungi, fruit bodies and infected plant tissues. *Nucleic Acids Res.,* **20**: 6115-6116.

Fernstrom, A. & Goldblatt, M. (2013). Aerobiology and its role in the transmission of infectious. *Diseases J. Pathog*., **Vol. 2013**: Article ID 493960

Ferreti-de-Lima, R. & de Moraes-Borba, C. (2001). Viability, morphological characteristics and dimorphic ability of fungi preserved by different methods. *Rev. Iberoam. Mycol*., **18**: 191-196.

Gabriel, M.F., Postigo, I., Tomaz, C.T., & Martinez, J. (2016). Alternaria alternata allergens: Markers of exposure, phylogeny and risk of fungi-induced respiratory allergy. *Environ. Int.,* **89-90**:71-80.

Gaddeyya, G., Niharika, P.S., Bharathi, P. & Kumar, P.K.R. (2012). Isolation and identification of soil mycoflora in different crop fields at Salur Mandal. *Adv. Appl. Sci Res.*, **3**: 2020-2026.

Gonnalves, C.L., Mota, F.V., Ferreira, G.F., Mendes, J.F., Pereira, E.C., Freitas, C.H. & Nascente, P.S. (2017). Airborne fungi in an intensive care unit. *Braz. J. Biol.*, **78**: 265.

Gots, R.E., Layton, N.J. & Pirages, S.W. (2003). Indoor health: Background levels of fungi. *Am. Ind. Hygiene Assoc. J.*, **64**: 427–438.

Hazrin, A.H., Anis Syazana, A.A., Noor, F.H.N., Norhidayahm, A. & Mohd, S.M.A. (2015). Indoor microbial contamination and its relation to physical indoor air quality (IAQ) characteristics at different laboratory conditions. *J. Tek.*, **77**:39-44.

Henselt, M. & Holden, D.W. (1996). Molecular genetic approaches for the study of virulence in both pathogenic bacteria and fungi. *Microbiol*., **142**: 1049-1058.

Horner, W.E., Worthan, A.G. & Morey, P.R. (2004). Air-and dustborne mycoflora in houses free of water damage and fungal growth. *Appl. Environ. Microbiol.*, **70**: 6394-6400.

Hwang, S.H. & Yoon, C.S. (2016). Main environmental factors affecting concentrations of culturable airborne bacteria in indoor laboratories over a period of one year. *Appl. Ecol. Environ.Res.*, **15**: 321-333.

Jasuja, N.D., Saxena, R., Chandra, S. & Joshi, S.C. (2013). Isolation and identification of microorganism from polyhouse agriculture soil of Rajasthan. *Afr. J. Microbiol. Res*., **7**: 4886-4891.

Javadi, M.A., Ghanbary, M.A.T & Tazick, Z. (2012). Isolation and molecular identification of soil inhabitant Penicillia. *Ann. Biol. Res*., **3**: 5758-5761.

Joana, M., Cristiana, P., Ines, P., Joao, P.T. & Eduardo, D.O.F. (2014). Identification and levels of airborne fungi in Portuguese Primary School. *J. Toxicol. Environ. Health*, **77**: 816-826.

Landeweert, R., Leeflang, P., Kuyper, T.W., Hoffland, E., Rosling, A., Wernars, K. & Smit, E. (2003). Molecular identification of ectomycorrhizal mycelium in soil horizons. *Appl. Environ. Microbiol*., **69**: 327-333.

Liu, D., Coloe, S., Baird, R. & Pedersen, J. (2000). Application of PCR to the identification of dermatophyte fungi. *J. Med. Microbiol*., **49**: 493-497.

Martinez, K.F., Rao, C.Y. & Burton, N.C. (2004). Exposure assessment and analysis for biological agents. *Grana*, **43**: 193-208.

Mebi, G., Samuel, W. & Ojogba, M. (2012). Relationship between fungal contamination of indoor air and health problems of some residents in Jos. *In* Kumar, S. & Kumar, R. (Eds.), *Air Quality - Monitoring and Modeling.* IntechOpen, London, UK, pp. 1–19.

NIOSH (National Institute of Occupational Safety and Health) (1998). *Method 0800: Biaerosol sampling (indoor air). In NIOSH Manual of Analytical Methods (NMAM), 4th Ed*. National Institute of Occupational Safety and Health (NIOSH), Ohio.

Pavan, R. & Manjunath, K. (2014) Qualitative analysis of indoor and outdoor airborne fungi in cowshed. *J. Mycol.,* **Vol. 2014**: 985921

Ricardo, A. & João, P.C. (2010). Fungal air quality in medical protected environments. *In* Kumar, A. (Ed.) *Air Quality*, IntechOpen, London, UK.

Shams-Ghahfarokhi, M., Aghaei-Gharehbolagh, S., Aslani, N. & Razzaghi-Abyaneh, M. (2014). Investigation on distribution of airborne fungi in outdoor environment in Tehran, Iran. *J. Environ. Health Sci. Eng.,* **12**: 1–7.

Stetzenbach, L.D., Buttner, M.P. & Cruz, P. (2004). Detection and enumeration of airborne biocontaminants. *Curr. Opin. Biotech.*, **15**: 170-174.

Takashi, S. & Akemi, N. (2003). Fungal identification method based on DNA sequence analysis: reassessment of the methods of the Pharmaceutical Society of Japan and the Japanese Pharmacopedia. *J. Health Sci.*, **49**: 531-533

Tong, X., Xu, H., Zou, L., Cai, M., Xu, X., Zhao, Z. & Li, Y. (2017). High diversity of airborne fungi in the hospital environment as revealed by meta-sequencing-based microbiome analysis. *Sci. Rep.*, **7**: 39606.

William, C.N., Arnab, P., Michael, J.A., Jennifer, R.W.H., Stanley, K., *et al*. (2005) Genomic sequence of the pathogenic and allergenic filamentous fungus Aspergillus fumigatus. *Nature*, **438**: 1151-1156.

Xi, L., Xue, Z., Wenji, W. & Kang, N. (2018). Microbial contamination screening and interpretation for biological laboratory environments. *Medicien &Micrecol.*, **5**: 1-10.

Xueyan Z., Jingyi L., Beibei W., Yang L. & Jingchao X. (2020). Indoor air design parameters of air conditioners for mold-prevention and antibacterial in island residential buildings. *Int. J. Environ. Res. Public Health*, **17**:1-16.

Yau, Y.H., Chew, B.T. & Saifullah, A.Z.A. (2012). Studies on the indoor air quality of pharmaceutical laboratories in Malaysia. *Int. J. Sustain. Built Environ.*, **1**:110-124.

DETECTION AND QUANTIFICATION OF BACTERIA ON FREQUENTLY TOUCHED SURFACES AT A WORKPLACE

Nik Nur Ilyani Mohamed Nazri* & Noor Hafifi Zuraini Abdul Rahim

Biosurveillance and Biological Defence Branch, Protection and Biophysical Technology Division (BTPB), Science and Technology Research Institute for Defence (STRIDE), Ministry of Defence, Malaysia

*Email: nikilyani.nazri@stride.gov.my

ABSTRACT

Surfaces frequently touched by personnel at workplaces harbour potential pathogens and may act as a source of infectious diseases and allergic reaction. Contrary to mould growth that usually gives visual discoloration, bacterial growth is often not visible. This study was conducted in April 2021 at a government premise in Selangor, Malaysia using a rapid on-site test based on hydrolase enzyme activity present in bacteria to determine whether frequently touched surfaces at this workplace have been contaminated by bacteria. Ten most frequently touched objects by personnel working in the same building had been identified to be the sampling objects. The Bactiquant-surface (BQS) method was applied in the study using a Mycometer microbial fluorometer detection system with Bactiquant-surface test assays. There were three samples taken from each object surface to ensure higher probability of discovering bacterial contaminations. A 9 cm^2 area self-adhesive template was applied to each surface for every sample taken. The samples were then analysed in the laboratory within 24 h of collection. The Bactiquant surface test results were expressed as Bactiquant-surface values (BQSV) and the surface bacterial contaminated levels were differentiated according to the interpretation criteria given. The results showed that none of the objects had been categorised as bacterial contaminated surfaces. Six of them, toilet door handle, water dispenser tap, sink bench, computer keypad, computer mouse and meeting table were categorised as dirty surfaces (BQSV in the range of 26 to 350), while the other four objects were categorised as clean surfaces (BQSV not more than 25). It was found that the dirtiest surface was the toilet door handle, while the cleanest surface was the incubator door handle. In conclusion, there was bacterial presence detected on the frequently touched surfaces at the workplace due to the transmission of organisms by human hands. These objects were often not cleaned or disinfected and could become potential sites for bacterial colonisation.

Keywords: *Microbial fluorometer detection system; bacteria hydrolase enzyme activity; bacterial contamination level; frequently touched surfaces; workplace.*

1. INTRODUCTION

Microorganisms are responsible for communicable diseases and can spread from various objects. Opportunistic pathogens have the ability to persist and multiply in a variety of environments and cause a wide spectrum of diseases in both humans and animals (Pilipcincova *et al.*, 2010; Akinkunmi & Lamikanra, 2010). Humans have a marked tendency to pick up microorganisms from environmental objects and the hands have been shown to play a role in the transmission of organisms (Oluduro *et al.*, 2011).

Contamination of environmental objects and surfaces is a common phenomenon, with pathogenic microbes dwelling in high concentration in many places of public utility (Alemu *et al.*, 2015). Most people do not realise that microbes are found on many common objects in the outdoors, in their offices and even in their homes, including playground equipment, kitchens, sinks, office desks,

computer keyboards, computer mice, escalator handrails and elevator buttons (Al-Ghamdi *et al.*, 2011; Hong *et al.*, 2012). Knowingly or unknowingly, they can easily infect users and may dwell in their body. When their load increases or one's immunity gets weakened, they become a serious threat (Alemu *et al.*, 2015).

A variety of inanimate objects could harbour bacteria (Rutala *et al.*, 2006; Miller & Diep, 2008; Obinna *et al.*, 2012; Enemuor *et al*., 2012). The ability of plastics and other objects to support viable microorganisms for a prolonged period of time is well documented, and such environmental surfaces and objects, especially those in close proximity with persons and frequently touched, pose a threat to health and are a cause for concern (Oluduro *et al.*, 2011).

The risk of transmission is directly proportional to the duration of survival of the bacteria on the colonised objects. The colonisation and survival depend on geographical and environmental conditions such as temperature, humidity, presence of organic matter, ability to form biofilms and prevalent infection control practices. Gram-positive and some Gram-negative organisms have been found to survive under various environmental conditions, such as in dry conditions and on various fabrics utilised in health care environments (Carter, 2005; Kramer *et al*., 2006). In fact, 80% of infections are spread through hand contact with hands or other objects (Al-Ghamdi *et al*., 2011). Soil and dust are important factors in preserving the viability of bacteria on hand surfaces and thus, dirty surfaces would harbour more bacteria than clean ones. This makes the process of dusting and removal of soil and dust by simple cleaning procedures of paramount influence on the reduction of surface contamination (Anastasiades *et al.*, 2009; Liang *et al.* 2009, Obinna *et al.*, 2012).

Identification of the more frequently contaminated sites and the most commonly identified potential pathogen is important for infection control practices and new interventions (Pittet *et al.*, 2006). Many people believe that microbes are only present in research labs or in hospitals and clinics, and thus they have a misleading feeling of security in other places. Lack of knowledge about where germs prowl could be a cause of health problems (Al-Ghamdi *et al*., 2011). Contrary to mould growth that usually gives visual discoloration, bacterial growth is often not visible (Mycometer, 2011).

To this end, a study was conducted in April 2021 at a government premise in Selangor, Malaysia using a rapid on-site test based on hydrolase enzyme activity present in bacteria to determine whether frequently touched surfaces at this workplace have been contaminated by bacteria to allow for appropriate further actions to be taken. Ten most frequently touched objects by personnel working in the same building had been identified to be the sampling objects.

2. MATERIALS AND METHODS

2.1 Samples Selection

The objects selected for the study were a meeting table in the meeting room; a telephone as well as a set of computer keypad and mouse in the administration room; a sink bench in the pantry; a water dispenser tap in the food laboratory; an elevator button and a staircase railing in the hallway; a toilet door handle; and an incubator door handle in the microbiology laboratory. These objects were selected for this study due to frequent and unavoidable contact with these surfaces by multiple users in the workplace. The objects were also often not cleaned or disinfected and could become potential sites for bacterial colonisation. The ability of door handles (Deshwal *et al*., 2013; Bhatta *et al.*, 2018), water taps (Bhatta *et al.*, 2018), sinks (Al-Ghamdi *et al*., 2011; Bhatta *et al.*, 2018), computer mice (Onasanya, 2002; Rahman, 2014), computer keyboards (Onasanya, 2002; Rahman, 2014), staircase railings (Courage *et al*., 2017; Bhatta *et al.*, 2018), elevator buttons (Kandel *et al*., 2014; Bhatta *et al.*, 2018), and telephones (Ciragil *et al*., 2006; Bhatta *et al.*, 2018) to act as fomites have been previously documented.

2.2 Surface Sampling

Surface sampling was performed according to the protocol for Bactiquant-surface (BQS) sampling (Mycometer, 2011). There were three samples taken from each object surface to ensure a high probability of discovering bacterial contaminations. A 9 cm^2 area self-adhesive template was applied to each surface for every sample taken. Each sterile swab was wetted with sterile saline before swabbing the 9 cm^2 area. Each surface was cleaned thoroughly as well as possible by rubbing the area in horizontal and vertical directions inside the template. The swab was rotated to use as much of the cotton as possible before it was returned into the container until analysis.

2.3 Surface Samples Analysis

The samples were analysed using a Mycometer microbial fluorometer detection system with Bactiquant-surface test assays within 24 h after sampling. The surface sample analysis was performed according to the protocol for BQS analysis (Mycometer, 2011). The results obtained were based on the fluorescence detection of hydrolytic bacterial enzyme activity that depends on the temperature of the enzyme substrate. The air temperature required to perform the analysis was within 18 to 30 °C. All the data measured by the microbial fluorometer detection system was recorded and calculated using the formula in Excel provided by Mycometer for quantifying bacteria in the samples, which converted the fluorescence unit values into Bactiquant-surface values (BQSV) that standardise the fluorescence unit readings for reaction time, temperature and sample volume:

Analysis value (AV) - Combined blank value (SB) = Bactiquant-surface values (BQSV) (1)

Based on the resulting BQSV obtained, the bacterial contamination level on the surface samples were differentiated according to the interpretation guidelines provided by Mycometer. The surface samples that obtained BQSV of not more than 25 were categorised as clean surfaces that are considered to have only background levels of bacteria as that seen in normal non-problematic surfaces. Samples that obtained BQSV in the range of 26 to 350 were categorised as dirty surfaces, while samples that obtained BQSV of more than 350 were categorised as contaminated surfaces.

3. RESULTS AND DISCUSSION

Figure 1 shows the bacteria quantification and interpretation criteria for each sampling object. The results show that there were no bacterial contaminated surfaces detected from all the frequently touched objects at the workplace selected for this study. This could be because the sample collection took place during the COVID-19 pandemic, which may have prompted increased use of hand sanitiser and gloves that block the transmission of organisms by human hands. However, six out of ten objects selected in the study had been detected as dirty surfaces, whereby the resulting BQSV obtained for all these surfaces were in the range of 26 to 350. It was found that the toilet door handle was categorised as the dirtiest surface, while the incubator door handle was the cleanest surface. Different environmental conditions in various sampling locations, such as temperature, humidity, presence of organic matter, ability to form biofilms and prevalent infection control practices may have contributed to the results of this study (Carter, 2005; Kramer *et al*., 2006).

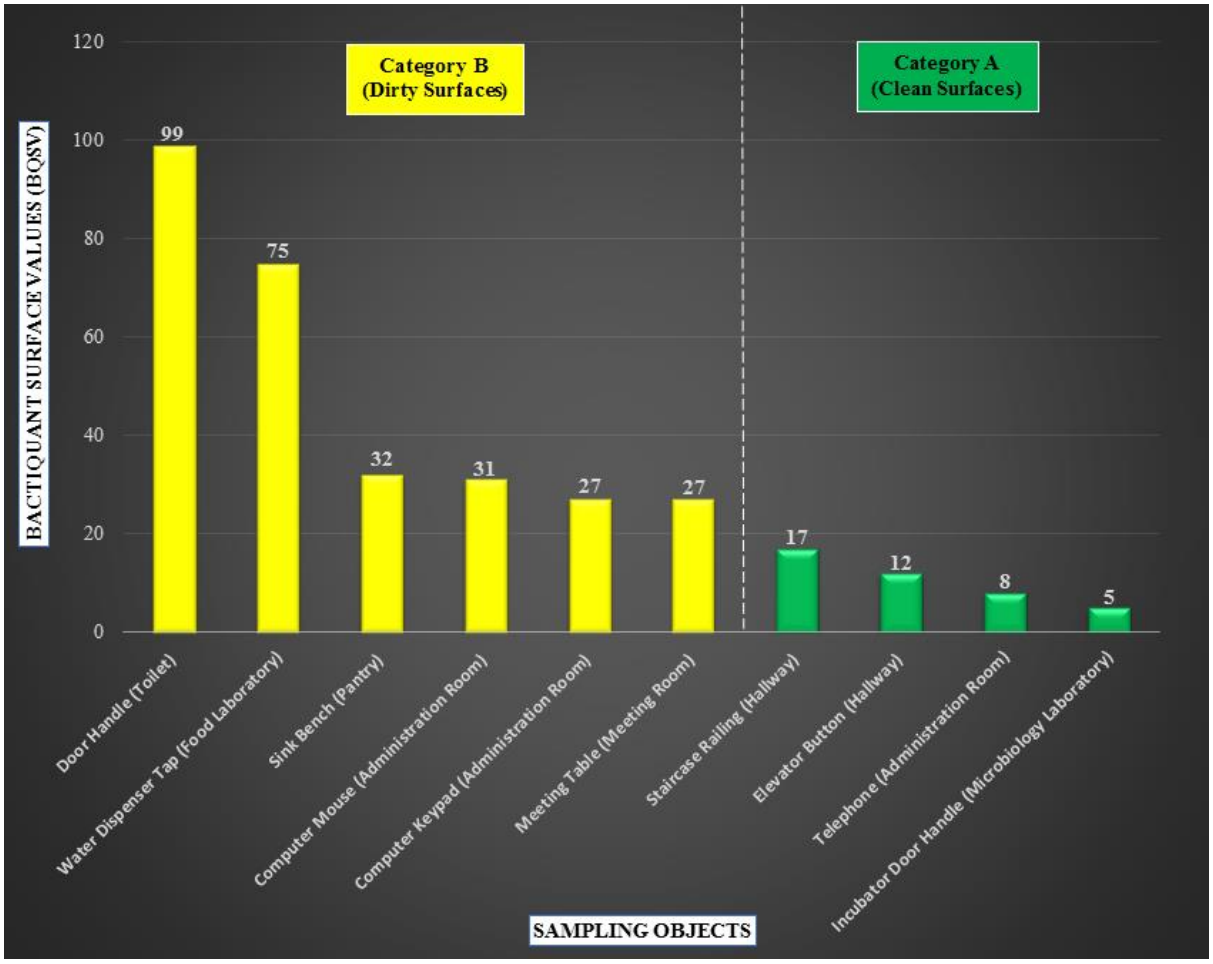

Figure 1: Bacteria quantification and interpretation criteria for each sampling object.

Bacteria are typically unicellular and require more moisture than fungi, both to survive and colonise on new surfaces. Therefore, surfaces in buildings with periodic or constant moisture may give rise to growth of naturally occurring bacteria (Mycometer, 2011). The incubator door handle being the cleanest surface detected in the study could be explained by the full day low temperature setting of 18 °C in the Microbiology Laboratory with the humidifiers functioning well to maintain the humidity and moisture in the laboratory surroundings to ensure the safety of the laboratory equipment that is mostly sensitive to heat and high temperature. The usage of gloves and alcohol-based disinfectants among the lab personnel are also at the highest practice when compared to any other location in the building because of their working nature in handling microorganism samples. The risk of pathogen transmission might be reduced by simple countermeasures (Kandel *et al.*, 2014), such as the usage of alcohol-based hand sanitisers, which is effective for removing surface bacteria (WHO, 2009).

There is no requirement at all to use gloves or hand sanitisers for the toilet users, which caused the toilet door handle to be detected as the dirtiest surface in the building. It should also be noted that a reason for the increased level of contamination of these frequently touched objects from one another is the difficulty to clean and disinfect the surfaces without proper practices. The type of material and size of surfaces are also influential factors (Al-Ghamdi *et al*., 2011). The ability of microorganisms to adhere to inert surfaces, to form biofilms as well as to resist further cleaning and disinfection procedures varies greatly according to the substratum composition (Faille & Carpentier, 2009). Due to these factors, Bhatta *et. al* (2018) stated that to date there are no established practices available for cleaning or disinfecting surface of elevator buttons, door handles, staircase railings, water taps and telephone sets.

Previous studies have identified that most of inanimate object colonisation is by skin bacteria, such as coagulase-negative staphylococci (CoNs) (Hartman *et al.,* 2004; Miller & Diep, 2008; Anderson & Palombo, 2009; Anupam *et al.,* 2011; Obinna *et al.,* 2012). CoNs is the most frequently cultured organism isolated from elevator buttons, and its distribution is approximately even across toilet surfaces (Kandel *et al*., 2014). It is also the most predominant pathogen found on computer equipment (Rutala *et al*., 2006; Awoleye *et al*., 2012; Alemu *et al*., 2015). A combination of constant handling in a restricted area and heat generated by the computers create a prime breeding ground for CoNs that is normally found on human skin because these types of bacteria increase in optimum temperature (Anjumn *et al*., 2011). Skin is a normal habitat for CoNs, but it can occasionally assume an opportunistic pathogenic role in causing human infections such as endocarditis (Anastasiades *et al*., 2009). CoNs are known to be present in hospital environments, and can be a source of cross infection, causing hospital acquired infections (HAI) especially in immuno-compromised hosts (Alemu *et al*., 2015).

Furthermore, available literature suggests that *Staphylococcus* and *Streptococcus* bacteria are present on various sample sites (Deshwal *et al*., 2013). A few reports indicated that Gram-positive bacteria are present on door handles (Deshwal *et al*., 2013; Augustine *et al.,* 2017), computer mice (Onasanya, 2002; Rahman, 2014), computer keyboards (Onasanya, 2002; Rahman, 2014), staircase railings (Courage *et al*., 2017), elevator buttons (Kandel *et al*., 2014; Bhatta *et al.,* 2018), and telephones (Ciragil *et al*., 2006; Bhatta *et al.,* 2018). The ability of *Staphylococcus aureus* to form biofilm on inanimate objects prolongs their survival and spread (Bhatta *et al.,* 2018).

Although *Staphylococcus* and *Streptococcus* bacteria are normal microflora of healthy humans, they are responsible for various diseases such as bacteremia and endocarditis, pneumonia, bone and joint infections, as well as central nervous system (CNS) infections (Snider & Swedo, 2003; Liu *et al.,* 2011). Reservoirs of pathogens have been identified in faeces, around the ear, as well as in the axilla and nares (Eastick *et al.,* 1996). *S. aureus* is part of the normal microbial of human skin and nasal passages, and it is known to be associated with numerous disease conditions. The ecological habitat for this microorganism in humans is in the anterior nares (Miller & Diep, 2008). One-quarter to one-third of healthy persons harbour *S. aureus* in the nose at any time, which can be easily transferred to the hands by simply rubbing the nose (Rutala *et al.,* 2006; Al-Ghamdi *et al*., 2011). *S. aureus* is responsible for nosocomial infections that have come to prominence through the rise of drug-resistant forms, particularly methicillin-resistant *S. aureus* (MRSA) (Thwaites & Gant, 2011). Deshwal (2012) reported that *S. aureus* causes urinary tract infection. Another *Staphylococcus* species, *Staphylococcus epidermis* has normal habitat on the skin but, similar to CoNs, can cause human infections such as endocarditis (Enemuor *et al.,* 2012). *Streptococcus* species indicates the possibility of mouth contamination (Obinna *et al*., 2012; Ubani *et al*., 2012). *Streptococcus pneumoniae* is a normal microflora that has the ability to cause disease and is one of the most common causes of community-acquired pneumonia, meningitis, and bacteremia in children and adults (Lynch & Zhanel, 2009).

Many Gram-negative bacteria, such as *Escherichia coli*, *Acinetobacter* species and *Pseudomonas aeruginosa* can survive on computer keyboards and mice surfaces, even for months (Onasanya, 2002). The presence of these bacteria on door handles (Augustine *et al.,* 2017; Frank, 2017), water taps (Bhatta *et al.,* 2018), elevator buttons (Kandel *et al.,* 2014; Bhatta *et al.,* 2018) and telephones (Bhatta *et al.,* 2018) have also been reported.

Acinetobacter species and *Pseudomonas* species are well known nosocomial pathogens and their presence on the surfaces can lead to spread in the community. Contamination of water taps (washroom and drinking water) by nosocomial pathogens may lead to contamination of drinking water resulting in gastrointestinal disorders. Presence of potential pathogens on hand operated water taps of washrooms increases the possibility of recontamination of hands, which negates the benefits of hand washing (Bhatta *et al.,* 2018). *E. coli* is the most widely adopted indicator of faecal pollution, and it is simple to be isolated and identified, with their numbers usually being given in the form of faecal coliforms/100 ml of wastewater (De Boer & Heuvelink, 2000). *E. coli* causes urinary tract infection and diarrhea (Fine *et al*., 1996). Isolation of *E. coli* from computer keyboards and mice is a

clear indication that the sterilisation or aseptic procedures adopted by the operators, if at all, is not effective in significantly reducing the level of the organism on these surfaces to an acceptable level (Fukada *et al*., 2008).

4. CONCLUSION

The data provided from the microbial fluorometer detection system was time saving, and very helpful for bacteria detection and quantification on frequently touched surfaces. From the results obtained in the study, six out of the ten objects in the study were detected as dirty surfaces, even though the sampling was done during the COVID-19 pandemic, whereby emphasis has been given on the practices of using hand sanitisers and hand washing among personnel. These results are indicative of the need for awareness on disinfection and cleaning of such surfaces on a regular basis and adequate hand hygiene. As these bacteria have pathogenic potential, their presence on the surfaces may be additional reservoirs for the transmission of microorganisms and become vectors for cross transmission of bacterial infections at the workplace.

Decontamination of the objects with alcohol-based disinfectants would reduce the microbial flora from the surfaces. This process would be convenient as most of these objects have small surface area that can be covered in a short period of time. Alcohol-based hand sanitisers are also effective for removing surface bacteria, and their strategic placement inside and outside of toilets, food and microbiology laboratories, administration and meeting rooms, pantries and elevators might attenuate some of the potential risk of pathogen transmission. The provision of non-hand touch techniques for elevator buttons, door handles and water taps could be another way of reducing the transmission.

REFERENCES

Akinkunmi, E.O. & Lamikanra, A. (2010). Species distribution and antibiotic resistance in coagulase-negative Staphylococci colonizing the gastrointestinal tract of children in ILE-IFE, Nigeria. *Trop. J. Pharm. Res.,* **9**: 35-43.

Al-Ghamdi, A.K, Abdelmalek, S.M.A., Ashsh, A.M., Faidah, H., Shukri, H. & Jiman-Fatani, A.A. (2011). Bacterial contamination of computer and mice, elevator buttons and shopping carts. *Afr. J. Microbiol.,* **5**: 3998-4003.

Alemu, A., Misganaw, D. & Wondimeneh, Y. (2015). Bacterial profile and their antimicrobial susceptibility patterns of computer keyboards and mice at Gondar University Hospital, Northwest Ethiopia. *Biomed. Biotechnol.*, **3**: 1-7.

Anastasiades, P.P.T.L., Rousseau, L.H., Steinberg, W.H. & Joubert, G. (2009). Staphylococcus aureus on computer mice and keyboards in intensive care units of the universitas academic hospital, Bloemfontein and ICU staff's knowledge of its hazards and cleaning practices. *S. Afr. J. Epidemiol. Infect.*, **24**: 22-26.

Anderson, G. & Palombo, E.A. (2009). Microbial contamination of computer keyboards in a university setting. *Am. J. Infect. Control*, **37**: 507-509.

Anjumn M.S., Reddy, P.P. & Abbas, I.R. (2011). Microbial contamination of laptop/ keyboards in dental settings. *J. Public. Heal. Denti*., **2**: 4-6.

Anupam, D., Rith, K., Ashish, K., Pandey, A. & Madan, M. (2011). e-Fomites. *Ann. Biol. Res.*, **2**: 111-115.

Augustine, B.O., Frederick, O.E., Paul, I.O. & Sunday, O. (2017). The role of door handles in the spread of microorganisms of public health consequences in University of Benin Teaching Hospital (UBTH), Benin city, Edo state. *Pharm. Sci. Technol*., **2**: 15-21.

Awoleye, O.M., Ogunkambi, D.A., Ayo-lawal, R.O., Adewole, G.O. & Elufisan, T.O. (2012). Techno-microbial hazards associated with cks: public health risk and policy implications in Nigeria. *J. Info. Sci.,* **2**: 37-41.

Bhatta, D.R., Hamal, D., Shrestha, R., Subramanya, S.H., Baral, N., Singh., R.K, Nayak, N. & Gokhale, S. (2018). Bacterial contamination of frequently touched objects in a tertiary care hospital of Pokhara, Nepal: how safe are our hands?. *Antimicrob. Resist. Infect. Control*, **7**: 1-6.

Carter, M.J. (2005). Enterically infecting viruses: pathogenicity, transmission and significance for food and water borne infections. *J. Appl. Microbiol.*, **98**: 1354-1380.

Ciragil, P., Gul, M. & Aral, M. (2006). Bacterial contamination of computers and telephones in a university hospital in Turkey. *J. Hosp. Infect*., **62**: 247-248.

Courage, S.S.S., Jean, K.A. & Stephen, W.K. (2017). Prevalence and pattern of antibiotic resistance of Staphylococcus aureus isolated from door handles and other points of contact in public hospitals in Ghana. *Antimicrob. Resist. Infect. Control*., **6**: 44.

De Boer, E. & Heuvelink, A.E. (2000). Methods for the detection and isolation of Shiga toxin-producing Escherichia coli. *Symp. Ser. Soc. Appl. Microbiol.*, **29**: 133-143.

Deshwal, V.K. (2012). Antibacterial activity of seeds of Mucuna pruriens against Escherichia coli and Staphylococcus aureus. *Global J. Res. Med. Plants Indigen. Med.,* **1**: 109-113.

Deshwal, V.K., Choudhary, S., Chauhan, D.S., Gupta, P.D. & Nisha (2013). Microflora on the surface of laboratory instruments. *J. Acad. Ind. Res.*, **2**: 298-300.

Eastick, K., Leeming, J.P., Bennett, D. & Millar, M.R. (1996). Reservoirs of coagulase negative staphylococci in preterm infants. *Arch. Dis. Child.*, **74**: F99-F104.

Enemuor S.C., Apeh, T.A. & Oguntrbeju. O.O. (2012). Microorganisms associated with computer keyboards and mice in a university environment. *Afr. J. Microbiol. Res.*, **6**: 4424-4426.

Faille, C. & Carpentier, B. (2009). Food contact surfaces, surface soiling and biofilm formation. *In* Fratamico, P.M., Annous, B.A. & Gunther IV, N.W. (Eds.), *Biofilms in the Food and Beverage Industries.* Woodhead Publishing Limited., Cambridge, United Kingdom, pp. 303-330.

Fine, M.J., Smith, M.A. & Carson, C.A. (1996). Prognosis and outcomes of patients with community acquired pneumonia: a meta-analysis. *JAMA*, **275**: 134-141.

Frank, N. (2017). Assessment of bacterial contamination of toilets and bathroom door handles/ knobs at Daeyang Luke Hospital. *Pharma. Biol. Eval.*, **4**: 193-197.

Fukada, T., Iwakiri, H. & Ozaki, M. (2008). Anaesthetists' role in computer keyboard contamination in an operating room. *J. Hosp. Infect.*, **70**: 148-153.

Hartman, B., Benson, M., Junger, A., Qunzzol, L. & Rohrig, R. (2004). Computer keyboard and mouse as a reservoir of pathogens in an intensive care unit. *J. Clin. Monit. Comp.*, **18**: 7-12.

Hong, D.Y., Park, S.O., Lee, K.P., Baek, K.J., Moon, H.W. & Han, S.B. (2012). Bacterial contamination of computer and hand hygiene compliance in the emergency department. *J. Emerg. Med.*, **19**: 387-393.

Kandel, C.E., Simor, A.E. & Redelmeier, D.A. (2014). Elevator buttons as unrecognized sources of bacterial colonization in hospitals. *Open Med*., **8**: e81-e86.

Kramer, A., Schwebke, I. & Kampf, G. (2006). How long do nosocomial pathogens persist on inanimate surfaces? a systematic review. *BMC Infect. Dis*., **6**: 130.

Liang, P., Iksin, L., Chienchen, T. & Ngma., L. (2009). Methicillin-resistant Staphylococcus aureus and interface surfaces of hospital wards and association with clinical isolates. *BMC Infect. Dis*., **164**.

Liu, C., Bayer, A., Cosgrove, S.E., Daum, R.S., Fridkin, S.K., Gorwitz, R.J., Kaplan, S.L., Karchmer, A.W., Levine, D.P., Murray, B.E., Rybak, M.J., Talan, D.A. & Chambers, H.F. (2011). Clinical practice guidelines by the infectious disease's society of America for the treatment of methicillin-resistant Staphylococcus aureus infections in adults and children. *Clin. Infect. Dis.*, **52**: 1-38.

Lynch, J.P. & Zhanel, G.G. (2009). Streptococcus pneumoniae: epidemiology, risk factors, and strategies for prevention. *Semin. Respir. Crit. Care Med.*, **30**: 189-209.

Miller, L. & Diep, B.A. (2008). Colonization, fomites and virulence rethinking the pathogenesis of community associated methicillin-resistant Staphylococcus aureus infection. *J. Infect. Dis*., **46**: 752-760.

Mycometer (2011). *Bactiquant^{TM}-Surface Handbook.* Mycometer, A/S, Hoersholm, Denmark.

Obinna O., Wankiti, N., Ndaka, A., Amarachi, J. & Godwin, O. (2012). Computer keyboard and mouse: etiologic agents for microbial infections. *Nat. Sci.*, **10**: 162-166.

Oluduro, A.O., Ubani, E.K. & Offoezie, L.E. (2011). Bacterial assessment of electronic hardware user

interfaces in I1F-IFE, Nigeria. *J. Basic Appl. Pharm. Sci.*, **32**: 323-334.
Onasanya, S.A. (2002). The impact of computer in a developing country like Nigeria. *Niger. J. Res. Produ.*, **1**: 56-78.
Pilipcincova, I., Bhide, M., Dudrikova, E. & Travnicek, M. (2010). Genotypic characterization of coagulase-negative staphylococci isolated from sheep milk in Slovakia. *Acta. Vet. Brno*., **79**: 269-275.
Pittet, D., Allegranzi, B., Sax, H., Dharan, S., Pessoa-Silva, C.L. & Donaldson, L. (2006). Evidence-based model for hand transmission during patient care and the role of improved practices. *Lancet Infect. Dis.*, **6**: 641-652.
Rahman, R.H.A. (2014). Bacterial contamination of computer keyboards and mouse. *Tikrit J. Pure Sci.*, **19**: 18-22.
Rutala, W.A., White, M.S., Gergen, M.F. & Weber, D.J. (2006). Bacterial contamination of keyboards: efficacy and functional impact of disinfectants. *Infect. Control Hosp. Epidemiol.*, **27**: 372-377.
Snider, L.A. & Swedo, S.E. (2003). Post-streptococcal autoimmune disorders of the central nervous system. *Curr. Opin. Neurol.*, **16**: 359-365.
Thwaites, G.E. & Gant, V. (2011). Are bloodstream leukocytes Trojan horses for the metastasis of Staphylococcus aureus?. *Nat. Rev. Microbiol*., **9**: 215-222.
Ubani, E., Oluduro, K. & Ofoezzie, I.E. (2012). A survey of common habits of computer user as indicators of possible environmental contamination and cross infection. *Afr. J. Biotechnol.*, **11**: 2241-2247.
WHO (2009). *WHO Guidelines on Hand Hygiene in Health Care*. World Health Organization 2009, Geneva, Switzerland.

EVALUATION OF LOSS FUNCTION OF RADIO MODULATION TRAINING DATASET IN AUTOMATIC MODULATION CLASSIFICATION FOR IN-DEPTH ARCHITECTURE NEURAL NETWORKS MODEL

Amira Syuhada Azmer*, Jawad Ali Shah & Suhaimi Bahisham Yusoff

Electronics Technology Section, Universiti Kuala Lumpur British Malaysian Institute (UniKL BMI), Malaysia

*Email: suhaimib@unikl.edu.my

ABSTRACT

In automatic modulation classification (AMC), loss function plays an important role to determine the errors between the outputs of training neural networks for every single training and given target value. Loss function is crucial not only for attaining the objective of minimising loss but also for model parameter estimation and initial assessment phases of the model since its value contributes considerably to the sum of the cost function. In this study, the loss function will be evaluated based on different tuned models of neural networks and how it may affect the performance of the accuracy model by using a combination of deep neural networks (DNNs) of convolutional neural networks (CNNs) and gated recurrent units (GRUs). The results show that by changing the parameters of filter size and number of filters per layer network, the loss function is moderately reduced to an average loss of 1.3 for all four tests carried out during training the DNNs. Overall accuracy performance of 70 - 76% was achieved by utilising a low-specification and low-performance graphics processing unit (GPU) designed specifically for AMD Radeon R5 M330 graphics engine for network model training hardware resources. From the results, the performance accuracy of 76% was achieved by using batch size of 2,000, filter sizes of 1 x 7 and 1 x 8, and 50, 100 and 220 filters per layer in the hierarchy layer of the neural network.

Keywords: Automatic modulation classification (AMC); end-to-end learning; deep learning; deep neural networks (DNNs); loss function.

1. INTRODUCTION

As communication and computing technologies evolved, it became natural when the two began to merge, forming the field of today's smart radio / software systems known as software-based radio (SDR) or cognitive radio that both rely on inseparable parts of next generation wireless networks (5G) (Perre *et al*., 2009). Functional flexibility becomes the leading institution to evolve software radios into a reconfigurable concept of a wireless communication system (Athira *et al*., 2016; Digon & Crippa, 2018). In order to achieve the flexibility concept, modulation information has been used extensively as one of the parameters in the development of software-based radios due to their requirements to operate over any air interface and protocol. This is because excessive numbers in bandwidth-critical applications can cause communication signals to travel in space with different frequencies and modulation types (Digon & Crippa, 2018). Therefore, automatic modulation recognition (AMR) provides modulation information for received signals, which can aid in determining the type of modulation utilised at the transmitter. From its initial evolution, AMR relied mostly on conventional signal processing techniques, but it has since evolved to include intelligent algorithms and computational learning, known as automatic modulation classification (AMC), for better performance in recognition activities for wireless communication systems (Al-Nuaimi *et al*., 2019).

Modulation signal identification associated with neural networks has led to integrated approaches for progressing from hand-crafted feature-based methods to end-to-end learning directly from the spectrum of data to achieve the conception of signal surveillance, frequency spectrum and radio monitoring (Athira *et al*., 2016). Employing deep neural networks (DNNs) in the area of deep learning has contributed significantly to a unified concept of end-to-end learning that requires processing architectures to autonomously learn from different hierarchies of features from data. Hierarchy learning includes extracting low-level features from raw input (i.e., data representation of a sensed wireless signal), which also can be known as the input layer (Peng *et al*., 2019). Followed by higher-level features based on previous level features representation, this may refer to the hidden layer and afterwards to the desired output in the output layer (i.e., predicted type of modulation) by classification tasks. In this process, the approximate reconstruction maps for model parameter estimation from observational data can be easily tuned based on configurations of hyperparameters (Goodfellow *et al*., 2016). However, due to of how their weights are adjusted, the output of training neural networks may differ from the provided target value (Christoffersen & Jacobs, 2004). This may cause errors during the training of neural networks, which can cause the condition known as loss function. It is critical to assess loss function circumstances that converge and compute to the local minimum, where all the efforts of the network models aim at minimising loss function to avoid having significant impact on the accuracy performance once the model has been trained and assessed during the learning process (Marsland, 2011).

In this study, loss function is computed and evaluated via a proposed approach of convolutional neural networks (CNNs) followed by gated recurrent units (GRUs) with hyperparameter configurations for an in-depth architecture neural network model with 30 epochs of 110,000 modulation signal data samples. In order to execute the training process, the proposed model network uses an AMD Radeon R5 M330 graphics engine and Intel 2.30 GHz Core I i5-6200U CPU. Four experiments are carried out by changing the hyperparameters based on filter size, number of filters per layer network and batch size; comparing loss function results; and finally evaluating how it affects overall accuracy performance.

The paper is organised as follows. Section 2 introduces the wireless signal model and the role of the AMC module. Section 3 proposes CNNs together with the gated recurrent unit model for in-depth neural network architecture. In Section 4, the accuracy of the model is analysed using loss function based on how the proposed model's hyperparameter configurations influence it. Section 5 summarises the key findings of the study.

2. WIRELESS SIGNAL MODEL AND THE ROLE OF AUTOMATIC MODULATION CLASSIFICATION MODULE (AMC) IN WIRELESS SYSTEMS

AMC plays an important role in the receiver part of a wireless communication system. The development of modulation recognition methods prompted a shift in research, focussing away from signal processing, and towards intelligent algorithms and computational learning, culminating in the metamorphosis of AMR into AMC. AMC automatically determines the modulation form of the signal being transmitted. The receiver performs a key process in AMC that helps to determine the modulation model from the received signal with the unknown format. Thus, modulation classification activities at the receiver side are the intermediary procedure between signal detection and signal demodulation in non-cooperative communications systems. In order to make this activity possible in terms of end-to-end learning from spectrum data, several researchers have demonstrated that the wireless signal model must go through pipelines that include data acquisition, data pre-processing, classification and decision-making for predictions (Kulin *et al*., 2018; Yu Wang *et al*., 2019). The wireless signal model, in addition to being a smart wireless network for wireless 5G future generation networks, is reminiscent of fundamental wireless communication systems at the system level, which includes a transmitter, receiver and wireless channel, as shown in Figure 1.

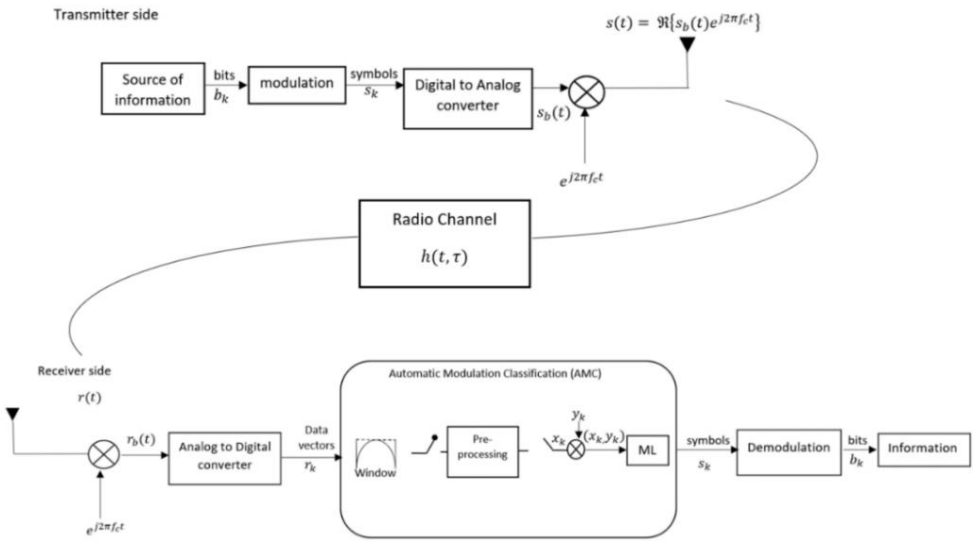

Figure 1: Signal processing chain in basic radio software (Kulin *et al*., 2018).

At the transmitting side, the transmitter converts the message stream of bits $b_k \in \{0,1\}$ generated by the information source into a format that is suitable for transmission signal $s(t)$ over the wireless channel (Haykin, 2014). By using the coding method, the bits are mapped into a new binary sequence. The resulting sequence is then mapped as either real or complex symbols s_k from the desired alphabet or constellation (Dobre *et al*., 2007). The process of the encoded bit is called modulation. Each modulation format has its own set of modulation symbols, and the size of the set determines the number of binary code symbols that can be represented by each modulation symbol (Tse & Pramod, 2005). The encoded bits associated with the symbols are translated into a discrete waveform or signal through a pulse shaping filter in the modulation phase and sent to the digital-to-analog converter module (D/A), where the waveform is converted into an analog continuous-time signal $s_b(t)$ (Chaparro & Akan, 2019). As a result, a baseband signal is obtained, which must then be transferred to a higher frequency by the carrier frequency to generate a wireless signal $s(t)$ (Frenzel, 2018).

The wireless channel is a time-varying fading channel, meaning that the capacity and throughput of the spectral efficiency metrics change over time due to a random fading process (Pérez-Neira & Campalans, 2009). This can happen when a carrier signal is transmitted over a wireless medium, which results in a received random multipath signal due to the scattering of the transmitted signal by several scatters along the transmission path (Schwartz, 2005). The net effect of these wireless channel differences is uncertain especially for signalling over band-limited channels, such as data transmission over the internet (Haykin, 2014). The input and output relation under band-limited bandpass channel impulse response $h(t,\tau)$, which widely used in conventional expert features, can be expressed as:

$$r(t) = s(t) * h(t,\tau) + n(t) \quad (1)$$

where $n(t)$ is additive white Gaussian noise (AWGN), $n \sim \mathcal{N}(0,\sigma^2)$ having mean zero and variance, while $*$ denotes the convolution operation.

Subsequently, the received wireless signal model $r(t)$ is used to transform the signal into an equivalent low-pass representation by combining it with the baseband complex envelope $r_b(t)$ (Al-Nuaimi *et al*., 2019). The process is then continued using data acquisition pipelines, which are critical as input to the AMC module. Adequate training data must be obtained to derive a machine learning model for wireless signal recognition. After the received signal $r(t)$ is amplified, mixed, low-pass filtered and passed through an analog-to-digital converter module (A/D), it is followed by time signal sampling with index k at rate $f = \frac{1}{T_S}$ samples per s, where f_s is the sampling rate to create a discrete version r_k, which denotes the discrete-time observed signal (Kulin *et al*., 2018). Then, input r_k in the form IQ complex becomes an input into the AMC module using the following equation:

$$r[k] = r_I[k] + jr_Q[k], k = 0, \ldots, N-1 \quad (2)$$

The representations of the received continuous sample stream is either segmented or windowed to r_k, which perform similarly to audio signal processing that carries information for assessing what type of modulation signal is sensed (Kulin *et al*., 2018). After collecting r_k, the data is ready to be pre-processed by analysing, processing, and transforming into a representation of feature vectors x_k that is suitable for training, which includes more complex forms, such as frequency, amplitude, and phase. At this stage in the process, the inputs are presented in distinct data point samples or observation pairing $\{(x_i, y_i)\}_{i=1}^{m}$, with each pair (x_i, y_i) responsible to determine the learning algorithm for the predictor f (Kim *et al*., 2016).

3. PROPOSED METHOD OF CNN FOLLOWED BY GRU FOR IN-DEPTH ARCHITECTURE NEURAL NETWORKS

For a good predictor f, the learning method must be chosen carefully. CNN's are widely used as a trained network by researchers because, unlike other feature extractors, CNNs can reduce the dimensionality constraint that is inherent in fully connected networks (Hong *et al*., 2017; O Shea *et al*., 2016; Peng *et al*., 2017; West & O'Shea, 2017; Zhang *et al*., 2018). CNN is organised in nested layers, whereby the input layer of the neural network brings the initial data into the model for processing by the subsequent layer at the start of the workflow. The input examines data with a grid-like topology, such as time-series data, which can be regarded as a 1D grid taking samples at regular time intervals, and image data, which may be regarded as a 2D grid of pixels (Goodfellow *et al*., 2016). Convolutional layers are used to extract higher-level features. The convolutional layer of the CNN algorithm takes feature maps from the previous layer as inputs and performs 2D convolution operations between the inputs and a collection of learnable filters to learn features directly from 2D binary data. The feature extractor $\emptyset(x)$ in at least one of the convolutional network layers uses kernels instead of generic matrix multiplication to feature map the data of feature vectors x_i.

For 2D computation, the kernel h is computed via commutative convolution over the input x equivalent to:

$$(x * h)_{ij} = x[i,j] * h[i,j] \quad (3)$$

$$x[i,j] * h[i,j] = \sum_n \sum_m x[n,m].h[i-n][j-m] \quad (4)$$

where m is the number of samples, and n is the vector of measurement for signal sample length or features vector for i^{th} observation, with the indexes of rows and columns of the resulting matrix marked with i and j respectively. Each convolutional layer in the neural network multiplies the inputs with a weighted matrix and adds a bias term, i.e., the output of the first layer in $W^1x + b_1$ form. When adding only the bias terms after convolutions are calculated, the expression of the CNN linear model tends to be equivalent output f approaching zero, if $W^lx + b_l \leq 0$ for the l^{th} feature map of the convolutional layer (Liang *et al*., 2018). As a result, in a multilayer neural network, the activation functions are used to include this non-linear element, which can define the functional relationship between the output of the upper node and the input of the lower node (Lee *et al*., 2017). These activation functions are set up with a rectified linear unit (ReLU) to speed up the convergence of gradient descent while keeping values for subsequent layers within a reasonable and practical range and forwarding the output (Yang *et al*., 2019).

Hence, the coefficient W^l, input x and bias $b_1$are computed to obtain the feature maps $h_{i,j}^l$ as follows:

$$h_{i,j}^l = g((w^l * x)_{ij} + b_l) \quad (5)$$

Audio source signals, for instance, have the characteristic of being temporarily correlated (Wu *et al*., 2018). Temporal correlation is viewed as critical information for signal representation in non-stationary source separation (Chien, 2019). In time-series analysis, linear models are a natural technique to characterise the temporal correlation structure of a stationary time series. However, when the process is driven by an exogenous variable, defining the correlation structure of the process is more difficult than in the case of stationary time series (Rao *et al*., 2012). Therefore, recurrent neural network (RNNs) is created and utilised after the CNN layers due to their ability to describe temporal sequences and their long-range dependencies (Lee *et al*., 2017). A RNN can memorise arbitrary-length sequences of input patterns by connecting units in a directed cycle (Chung *et al*., 2014). Due to its memorising capabilities, this neural network is immensely beneficial for time series prediction. This benefit can be used by the learning algorithm of GRU that was proposed by Cho *et al*. (2014). GRUs can alternatively be thought of as a less complicated variant of long short-term memory (LSTM). In order to capture dependencies on different time scales, a GRU is created to produce each recurrent unit.

The GRU has gating units that influence the flow of information inside the unit without the use of distinct memory cells. Two gates are introduced in GRU, which is a reset gate r that governs the merging of new input with prior memory, and an update gate z that controls the preservation of valuable memory. The reset and update gates govern how much each hidden unit remembers or forgets while reading or adaptively creating a sequence. The variable-length sequence using a recurrent hidden state whose activation h is dependent on the prior time (Chung *et al*., 2014) and the recurrent hidden state h_t is updated by the following rules defined as:

$$h_t = \begin{cases} 0, & t = 0 \\ \emptyset\left(h_{t-1,x_t}\right) & otherwise \end{cases} \tag{6}$$

The updated recurrent hidden state h_t should be applied as:

$$h_t = g(W_{x_t} + Uh_{t-1}) \tag{7}$$

The final layer of the DNN architecture is the hidden dense layers. The operation of the algorithm in dense layers requires multiplying the dense layer's kernel with the input vector in a matrix, followed by addition with a bias vector and an activation function. The necessary weights and biases to use the near-linear component of the activation function are learned by a dense layer with nonlinear activation. As a result, nonlinear activation increases the number of input-output linkages that a dense layer may learn by a factor of two. In order to recapitulate the proposed model, the whole DNN architecture is made up of multiple convolutional layers, GRU layers and dense layers, all of which are connected and stacked on top of one another. A dense layer with a SoftMax activation and several units equal to the number of types of modulation classes is placed at the end of the layer stack to better suit the classification task. The SoftMax classifier computes the probability distribution of each class label over K classes as the final layer as (Kulin *et al*., 2018):

$$\hat{y}_i = \frac{e^{z_i}}{\sum_{j=1}^{K} e^{z_j}}, \qquad i = 1, \dots, K \tag{8}$$

The computed scores at the output layer Z_i are transformed to probabilities in the form of logits before passing through SoftMax activation. Each feature vector in the training data set is associated with a true label class that is represented using a one-hot encoding that accepts only numerical categorical values. The difference between estimated probabilities of $\hat{y}_i$ and the one-hot encoding of the true class labels y_i, where y_i is the label of sample i and $\hat{y}_i$ is the probability of the sample belonging to the positive class, is assessed by the loss function on the last fully connected layer.

3. METHODOLOGY FOR MEASURING THE LOSS FUNCTION

As illustrated in Figure 2, the process of measuring the loss function starts with data pre-processing of feature vectors and ends with estimated probabilities in the last layer of the classification task. The feature vector must appropriately be able to carry two important tasks during the training dataset. First, the feature vector of $\boldsymbol{x_i}$ is used to compute DNN models that include essential hyperparameter tuning, such as type of neural network models, size of filters and number of filters per layer. The feature vector of $\boldsymbol{y_i}$ is then encoded by using one-hot encoding. In the process of encoding, the binary vectors are used to indicate the categorical variables of the observed data points. The category values must first be transferred to integer values before proceeding, except for the index of the integer with value 1, whereby each integer value is represented as a binary vector consisting entirely of zero values.

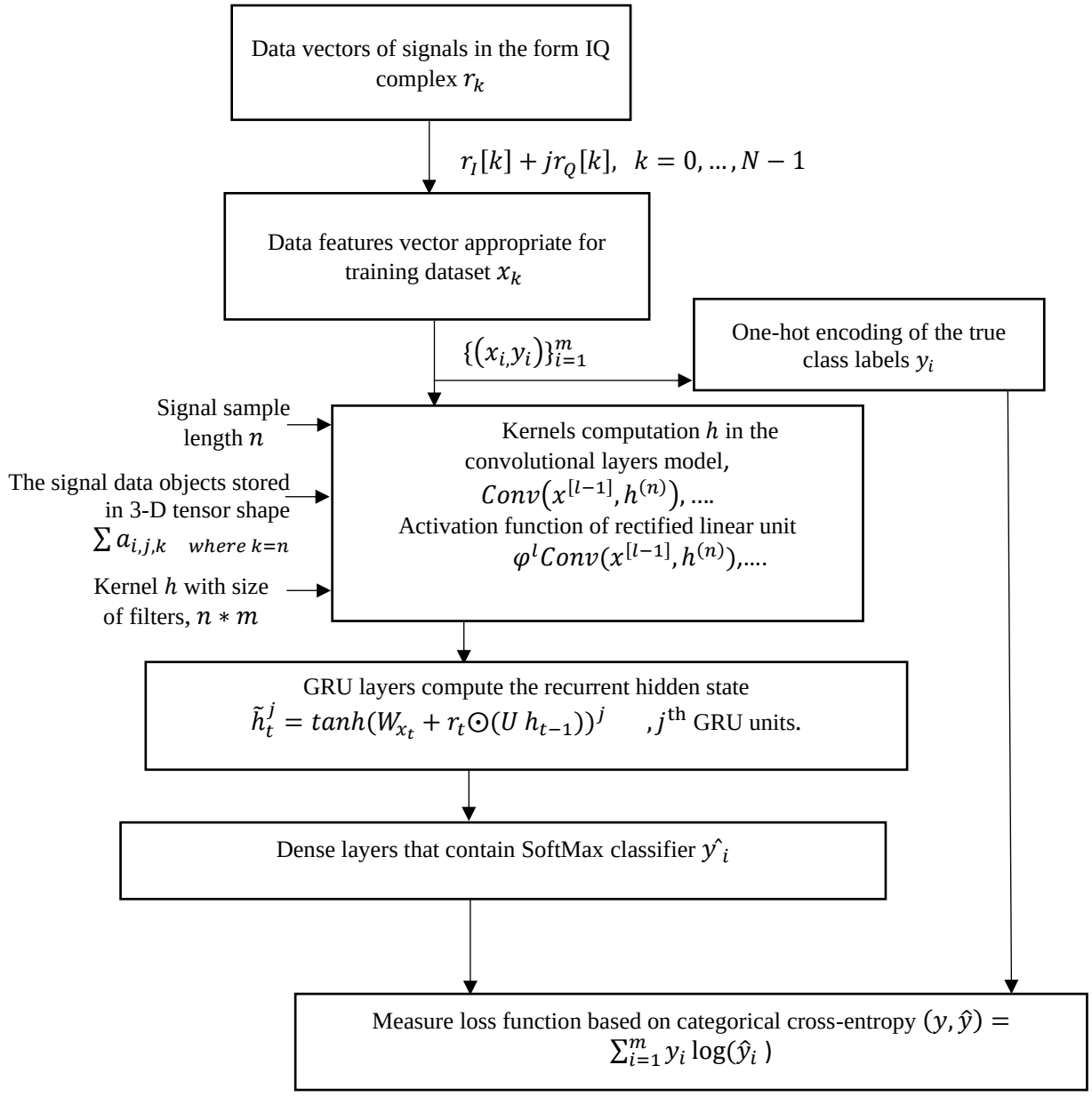

Figure 2: Flow chart of loss function measurement.

The loss function of categorical cross-entropy is determined during the running number of epochs, which is defined as the number of passes in each training dataset viewed by the learning algorithm of the DNN. Its value of loss function substantially adds to the sum of the cost function, which considers

three elements $l(x, y, \theta)$ for performing function estimation f to compute pointwise error between the observed data point y_i and model prediction $\hat{f}(x_i)$ for each value of vector θ. By incorporating the use of θ, which is known as a set of adjustable parameters (weights), approximating f can be described in the parametric model, with training loss $\boldsymbol{J}$ calculated in average as shown in Figure 3.

<table>
<tr><td colspan="2">The observed data will consist of input-output pairs for training data set S</td></tr>
<tr><td colspan="2">$S = \{(x_1, y_1), (x_2, y_2), = tain(x_m, y_m)\}$</td></tr>
<tr><td>Feature vectors of x_i in input X</td><td>Feature Vectors of y_i in output Y</td></tr>
<tr><td>$X = \begin{bmatrix} x_1^T \\ x_2^T \\ \vdots \\ x_m^T \end{bmatrix} \in \mathbb{R}^{mxn}$
$\chi = [x_1^T, x_2^T, \dots\dots\dots, x_m^T]^T \in \mathbb{R}^{mxn}$
$X_i = \left[x_{i1}, x_{i2}, \dots\dots\dots, x_{in}\right]^T \in \mathbb{R}^n \ , i = 1, \dots, m.$</td><td rowspan="2">The outputs y are the outcomes of categorical variables corresponding to the inputs x_i denoted by:
$Y = [y_1, y_2, \dots\dots\dots, y_m]^T \in \mathbb{R}^m$</td></tr>
<tr><td>Parameter of vector θ for predictor $\hat{f}(x_i)$
$\theta = [\theta_1^T, \theta_2^T, \dots\dots\dots, \theta_m^T]^T \in \mathbb{R}^n$</td></tr>
<tr><td colspan="2">By applying the algorithm to the learning processing chain model as in Figure 1, at sampling index k, the observed data training dataset S can be computed as:
$(S) = \{(x_1, y_1), (x_2, y_2), \dots\dots\dots\dots (x_k, y_k)\}$
Estimating θ on the whole training data S:
$(S, \theta) = \{(x_1, y_1, \theta_1), (x_2, y_2, \theta_2), \dots\dots\dots\dots (x_k, y_k, \theta_k)\}$</td></tr>
<tr><td colspan="2">Minimize the training loss using vector θ :
$argmin\, J(\theta) \quad , \theta \epsilon \mathbb{R}^n$
Measuring training loss J using mean square error:
$J(S, \theta) = \frac{1}{m} \sum_{(x_i, y_i) \epsilon S} l(x_i, y_i, \theta)$</td></tr>
</table>

Figure 3: Measurement of the loss function.

In machine learning, a dataset is used to learn data points from input values of X and output values of Y. As a result, the observed data will be input-output pairs for training dataset S as follows:

$$S = \{(x_1, y_1), (x_2, y_2), = foll(x_m, y_m)\} \tag{9}$$

The inputs $\chi h \epsilon \mathbb{R}^{mxn}$ signify the number of distinct data points, with samples or observations denoted by the following equations based on values of X, where m is the number of samples or sample size, and n is the vector of measurement for signal sample length or feature vector for i^{th} observation:

$$X = \begin{bmatrix} x_1^T \\ x_2^T \\ \vdots \\ x_m^T \end{bmatrix} \in \mathbb{R}^{mxn} \tag{10}$$

$$\chi = [x_1^T, x_2^T, \dots\dots\dots, x_m^T]^T \in \mathbb{R}^{mxn} \tag{11}$$

A number of distinct data points samples or observation pairing $\{(x_{i,}y_i)\}_{i=1}^{m}$, where x_i is the i^{th} received sequence and y_i is the corresponding modulation scheme index that can be written as:

$$X_i = [x_{i1,}x_{i2,\ldots\ldots\ldots\ldots,}x_{in}]^T \epsilon\ \mathbb{R}^n\ , i = 1, \ldots, m. \tag{12}$$

$$Y = [y_{1,}y_{2,\ldots\ldots\ldots\ldots,}y_m]^T \epsilon\ \mathbb{R}^m \tag{13}$$

With parameter vector $\theta\epsilon\ \mathbb{R}^n$ to the model prediction $\hat{f}(x_i)$, the learning processing chain model for the input-output pairs $(x_{i,}y_i)$ of the training data can be written as:

$$(S,\ \theta\ ) = \{(x_1, y_{1,}\ \theta_{\ 1}), (x_2, y_2,\ \theta_{\ 2}), \ldots\ldots\ldots\ldots (x_k, y_k,\ \theta_{\ k})\} \tag{14}$$

The advantage of having this estimating parameter θ is to address convex optimisation regarding the training loss $J(\theta)$ averaged across all training examples. At this stage, each pair of $(x_k, y_k,\ \theta_{\ k})$ oversees performing the loss function computation as shown in Figure 4.

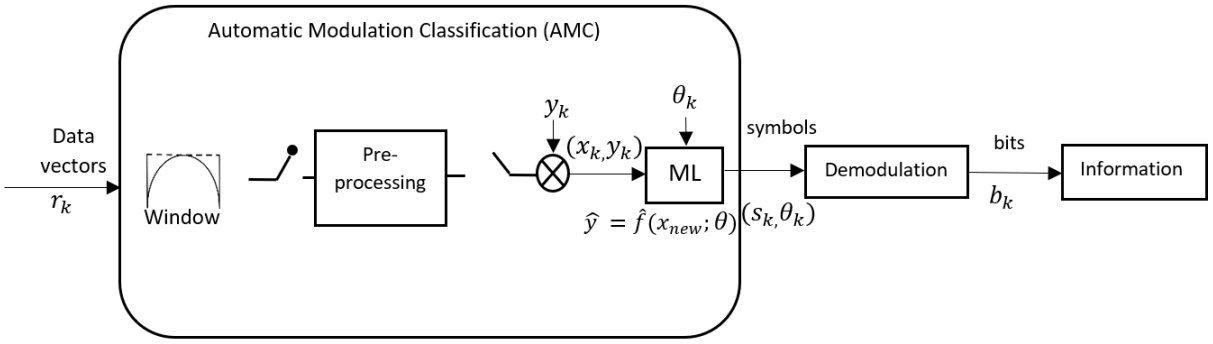

Figure 4: The AMC module.

4. RESULTS AND DISCUSSION

In order to evaluate the process of finding loss function based on the proposed method, a simulation is carried out by conducting four experiments that have different parameters. Table 1 shows how the loss function is minimised based on the proposed method.

Table 1: Results for the four experiments based on the proposed method.

Proposed Method	**Parameters θ**		**Total trainable parameter θ**	**For training and testing, an average loss across 30 epochs was calculated.**
Experiment 1	Type of layers used	CNN, GRU	487,763	1.3037477338178591
	Number of layers used	3 layers of CNN, 2 layers of GRU		
	Size of filters $n * m$	1 x 7, 1 x 8		
	Number of filters per layer	50, 100, 220		
	Batch size	2,000		

Experiment 2	Type of layers used	CNN, GRU	543,863	1.3324869338761676
	Number of layers used	3 layers of CNN, 2 layers of GRU		
	Size of filters $n * m$	1 x 7, 1 x 8		
	Number of filters per layer	50, 120, 220		
	Batch size	2,000		
Experiment 3	Type of layers used	CNN, GRU	618,583	1.3147033873606813
	Number of layers used	3 layers of CNN 2 layers of GRU		
	Size of filters, $n * m$	1 x 7, 1 x 8		
	Number of filters per layer	50, 220, 90		
	Batch size	2,000		
Experiment 4	Type of layers used	CNN, GRU	619,993	1.3665860832922838
	Number of layers used	3 layers of CNN 2 layers of GRU		
	Size of filters, $n * m$	1 x 7, 1 x 8		
	Number of filters per layer	50, 220, 90		
	Batch size	2,500		

In this experiment, 110,000 samples are fed into the network model for the training process. The sample is randomly divided into half as training data and the other half as testing data for the validation dataset to the test data's input and output. The larger dataset quantified with 110,000 samples may lead to the condition stated in Yan Wang *et al*., (2019), where the entire dataset can be trained in the input model if the only condition is permitted by a subset of the data split into the batches for training. The dataset required to train the network model often comprises of a considerable quantity of data and network model training hardware resources, such as computer and graphical memory capacity, which are often considered as requirement for better performance (Yan Wang *et al*., 2019). This is because deep learning is a technique for resolving more intuitive and complicated problems that are difficult to solve with standard computer systems or software (Vishnukumar *et al*., 2018).

The computational demand in neural networks is well-suited to graphic processor unit (GPU) implementation given that the weight resides on the GPU, thanks to the parallel processor of GPUs supporting the assigned tasks by the central processing units (CPUs) (Oh & Jung, 2004; Steinkraus *et al*., 2005). Due to the hierarchy of conceptions, both the CPU and GPU can support neural networks to recognise patterns by gathering knowledge from experience and to learn complicated concepts by creating them out of simpler ones (Oh & Jung, 2004; Vishnukumar *et al*., 2018). In this study, the experiments are conducted using a Windows 10 64-bit operating system with an Intel 2.30 GHz Core I i5-6200U CPU, 8 GB RAM, and 2 GB of AMD Radeon R5 M330 graphics engine, as described in (Jena *et al*., 2021) Although the AMD Radeon R5 M330 graphics processor may not be as powerful as the Nvidia graphics processors demonstrated in other studies (Hong *et al*., 2017; West & O'Shea, 2017; O'Shea *et al*., 2017), the findings of Jena *et al*. (2021) demonstrated that two classifications of images performed better when utilising the deep CNN method with the benefit of Radeon Technology's low cost and low power consumption (Miller, 2013).

During the training, a different number of trainable parameters are adjusted, including batch size to determine the direction of the gradient decrease by observing how to converge the loss functions to reach the minimum. By training on the same module with various tuning parameters, the value of the loss function declines at distinct values between each consecutive epoch. From the results in Table 1, Experiment 1 shows the smallest average value of loss function as compared to Experiments 2-4. The results might seem to fall at different local minimum points during the training process but Experiments 1 and 3 manage to have the consistency of maintaining a number of the same values of loss functions at a few epochs of the training procedure. When 30 epochs have been completed or an early stopping condition has been met, such as when the loss on the validation set has stopped declining, the training is completed. In terms of convergence, the iterative process at 30 consecutive epochs are terminated under two conditions. When the estimator approaches convergence, the first condition ends the procedure. The difference between the anticipated likelihoods of the current iteration and the prior iteration as well as a pre-defined threshold are used to express the condition quantitatively. When the pre-defined number of iterations is achieved, the second condition triggers termination. Figures 7-10 show the graphs that depict the behavioural patterns of convergence, with the vertical axis loss representing the loss of categorical cross-entropy and the horizontal axis representing the number of epochs.

In Figure 7, the graph for Experiment 1 shows that the validation loss slightly increases from the training loss + error as the number of epochs increases from 6 to 11, 12 to 15, and 19 to 22. However, the meet-point is connected to both training and testing via 18 data points. The findings demonstrate that the loss function's 18 data points continuously converge around the same point at the speed convergence with the average loss function at point 1.332.

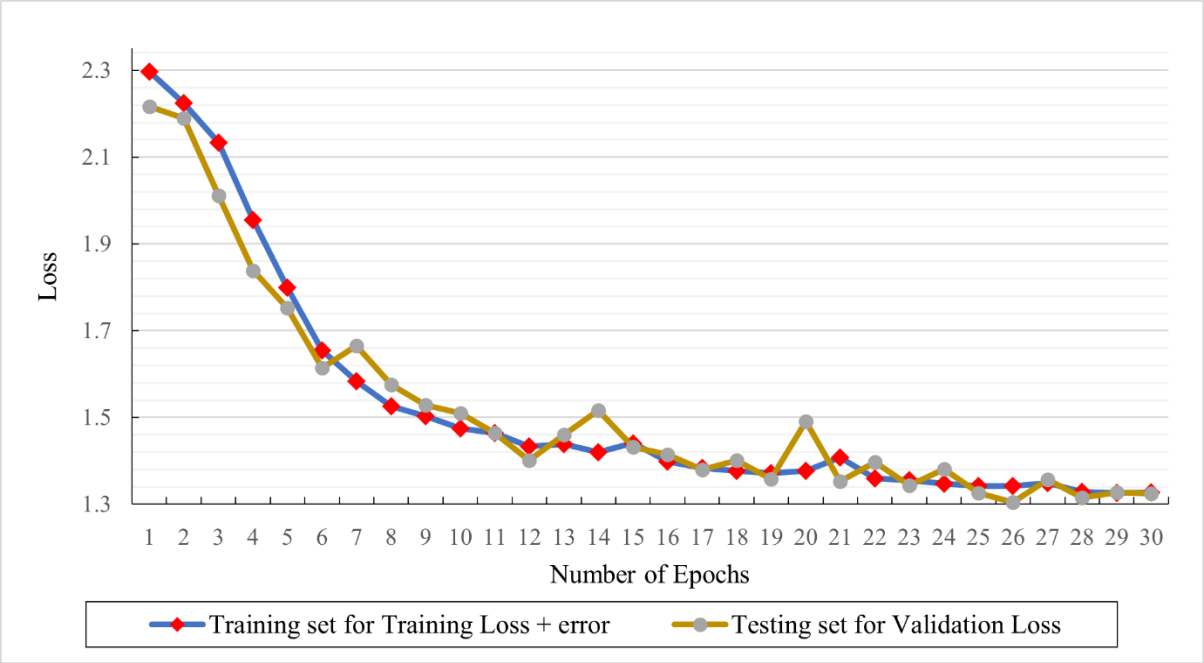

Figure 7: Graph of loss functions for the training and testing sets for Experiment 1.

In Figure 8, the graph for Experiment 2 shows that the validation loss is steadily increasing, and that overfitting may occur during epochs 6 to 15. There are about 12 meet-points that are connected to both training and testing. The results show that the 12 data points of the loss function continually converge towards the same point at the same pace as the average loss function at point 1.303.

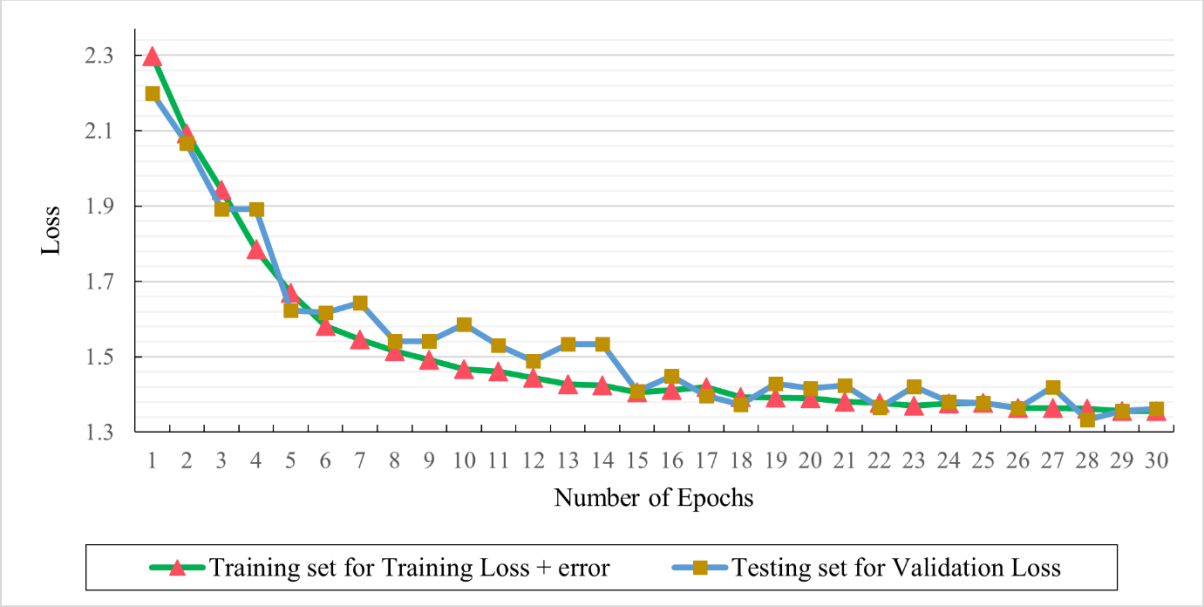

Figure 8: Graph of loss functions for the training and testing sets for Experiment 2.

In Figure 9, the graph for Experiment 3 shows that 10 data points converge extremely smoothly at a rate of 1.314, particularly during epochs 27 to 29. Experiment 3 appears to be more convergent than Experiment 2, even though there are only approximately 10 data point intersects for both training and testing.

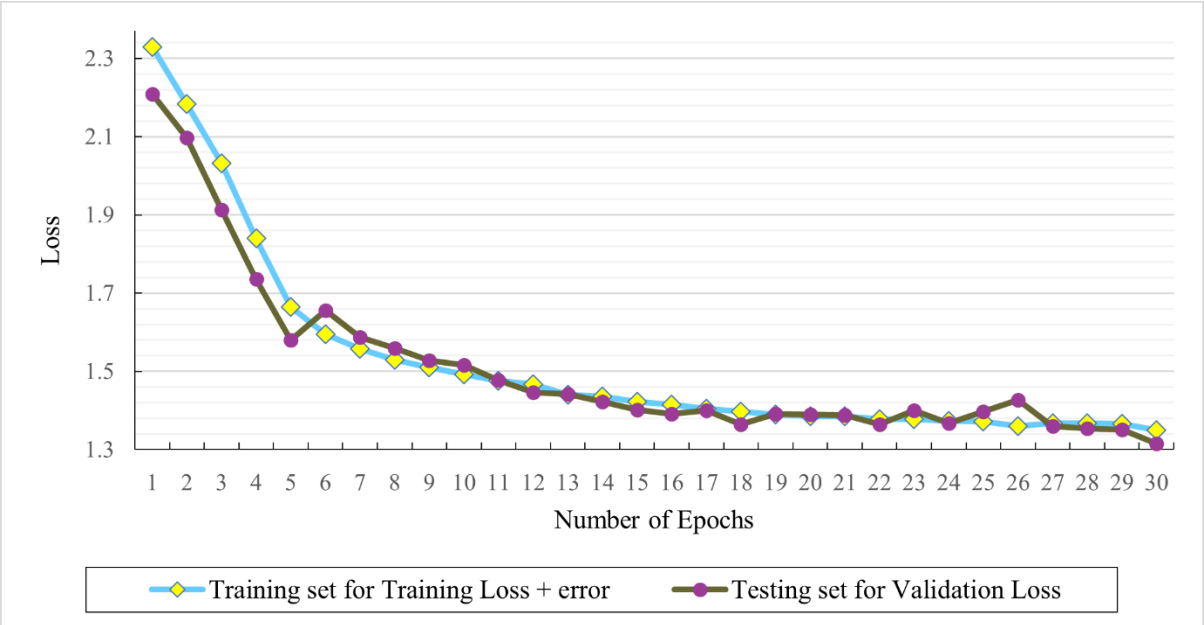

Figure 9: Graph of loss functions for the training and testing sets for Experiment 3.

For Experiment 4, Figure 10 reveals that the most intense oscillations occur between epochs 5 and 11, indicating that overfitting has taken place.

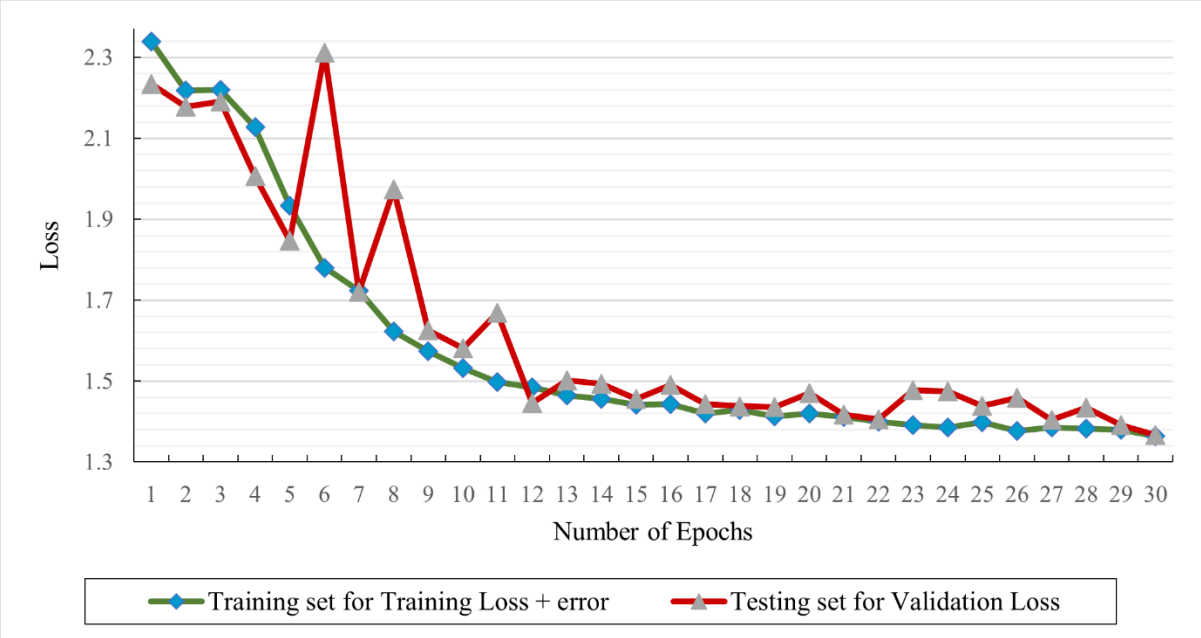

Figure 10: Graph of loss functions for the training and testing sets for Experiment 4.

As shown in Table 2, it can be concluded that Experiment 1 appears to have fewer total parameters and lower average loss as compared to the other experiments, resulting in the best performance with accuracy 76%. The size of filters of 1 x 7 and 1 x 8 working together proved to greatly contribute to the hyperparameter tuning as well as the number of filters per layer of 50, 100 and 220 in the hierarchy layer of the neural network together with the GRUs. Additionally, the findings demonstrate that the training effect of the model is affected by the batch size.

Batch size with the value of 2,000 has the highest precision that can be achieved for the DNNs. The 110,000 samples of data are divided into the 2,000 batch input model for training. Batch sizes will make sure the quantity of 2,000 samples is learned by the algorithm at one iteration at a time for the benefit of taking up less space to the machine's memory. This procedure is repeated until we have propagated all 110,000 samples through the network.

Table 2: Summary of results obtained with the proposed method.

Experiment	Total Trainable Parameters	Batch size	Average loss *J*	Accuracy Performance (%)
1	487,763	2000	1.303	76
2	543,863	2000	1.332	72
3	618,583	2000	1.314	73
4	619,993	2500	1.366	70

With the low performance of the AMD Radeon R5 M330 graphic engine, the AMC is capable to classify the radio signal with a performance accuracy of 70 - 76%, as shown in Table 3.

Table 3: Performance of DNN in AMD Radeon R5 M330 graphics engine.

Low-specification GPU	References	Type of DNN used	Training samples	Type of image data	Classification	Performance accuracy (%)
AMD Radeon R5 M330 graphics engine	(Jena *et al*., 2021)	CNN	11,000	2D images of Malaria Cell	2 classes of image data (parasitised image, uninfected image).	96%
	The proposed method in this paper	CNN + GRU	110,000	2D image of radio signals	11 classes of image data, as follows: Modulation type: WB-FM, AM-SSB, AM- DSB, BPSK, QPSK, 8PSK, 16QAM, 64QAM, BFSK, CPFSK and PAM4 Signal to noise ratio: -20:2:18 (dB) SNR	70 - 76%

5. CONCLUSION

This study has shown both CNN and GRU can minimise the loss function at the initial assessment phase by working on the parameter changes and tuning. Experiment 1 performed the best, with an average loss that was smaller than the other methods. By reducing the total loss function, both CNN and GRU may achieve accurate performance in modulation classification. Overfitting appears to have a greater impact on the loss that occurs during validating the training set. At a given number of epochs in the training method, it demonstrates that they all finally converge to approximately the same place, with different parameters affecting the convergence behaviour. This process is repeated until the system has reached the minimum state of convergence. Experiment 1 was successfully shown to have fewer total trainable parameters and smaller average loss than the other approaches, resulting in the best performance with an overall performance accuracy of 76%. The number of filters per layer of 50, 100 and 220 in the hierarchy layer of the neural networks, as well as the GRUs, has shown to have significant impact on hyperparameter tuning as well as the selection of the batch size of 2,000 to avoid overfitting training and burdening the machine memory.

The two separates studies shown in Table 3 that use the identical concept of DNN but distinct technique configurations have shown that a low-specification and low-performance GPU designed specifically for AMD Radeon R5 M330 graphics engine is capable of recognising 2D image data with a variety of classification of data classes. The results show that using this GPU for network model training hardware resources, it is possible to obtain an overall performance accuracy of 70 to 76%. In short, the measurement of the loss function is critical in deep learning for computing the error of a single training that is utilised for parameter estimation in AMC because it affects overall performance accuracy. In Experiment 1, the best feasible accuracy performance of 76% was demonstrated by using batch size of 2,000, filter sizes of 1 x 7 and 1 x 8, and 50, 100 and 220 filters per layer in the hierarchy layer of the neural network.

ACKNOWLEDGEMENT

The authors would like to thank Universiti Kuala Lumpur British Malaysian Institute (UniKL BMI) for allowing and supporting us to carry out the deep learning research.

REFERENCES

Al-Nuaimi, D.H., Hashim, I.A., Abidin, I.S.Z., Salman, L.B. & Isa, N.A.M. (2019). Performance of feature-based techniques for automatic digital modulation recognition and classification—a review. *Electr*., **8**:1407.

Athira, S., Mohan, R., Poornachandran, P. & Soman, K. P. (2016). Automatic modulation classification using convolutional neural network. *Int. J. Comput. Technol. Appl.*, **9**: 7733–7742.

Chaparro, L. F., & Akan, A. (2019). Sampling Theory. In *Signals and Syst. Using MATLAB (3rd Edition)*. Academic Press.

Chien, J. (2019). *Source Separation and Machine Learning*. Academic Press, Massachusetts, US.

Cho, K., van Merrienboer, B., Bahdanau, D. & Bengio, Y. (2014). On the properties of neural machine translation: encoder–decoder approaches. *Proc. 8th Worksh. Syntax, Semantics Struct. Stat. Transl. (SSST-8)*, pp. 103–111.

Christoffersen, P. & Jacobs, K. (2004). The importance of the loss function in option valuation. *J. Financ. Econ.*, **72**: 291–318.

Chung, J., Gulcehre, C., Cho, K. & Bengio, Y. (2014). Empirical evaluation of gated recurrent neural networks on sequence modelling. *Neural Inf. Process. Syst (NIPS 2014)*, 8-13 December 2014, Montreal, Canada.

Digon, I. & Crippa, M. R. (2018). Cognitive Radio Oriented Wireless Networks. *12th EAI Int. Conf. CrownCom*, (CROWNCOM 2017), 20-21 September 2018, Lisbon, Portugal.

Dobre, O. A., Abdi, A., Bar-Ness, Y. & Su, W. (2007). Survey of automatic modulation classification techniques: classical approaches and new trends. *IET Commun.*, **1**: 137–156.

Frenzel, L. E. (2018). Radio/Wireless: The Invisible Cables of Modern Electronics. In *Electr. Explained: Fund. for Engineers, Technicians, and Makers (2nd Ed.)* pp. 159–194. Newness.

Goodfellow, I., Benglo, Y. & Courville, A. (2016). *Deep Learning.* MIT press.

Haykin, S. (2014). *Digital Communications Systems*. John Wiley & Sons Inc., New Jersey, US.

Hong, D., Zhang, Z. & Xu, X. (2017). Automatic modulation classification using recurrent neural networks. *2nd IEEE Int. Conf. Comput. Commun.(ICCC 2016)*, pp. 695–700.

Jena, Om & Mohanty, Sachi & Nalinipriya, G. & Sarkar, Achyuth. (2021). *Machine Learning for Healthcare Applications.* Scrivener Publishing.

Kim, B., Kim, J., Chae, H., Yoon, D. & Choi, J. W. (2016). Deep neural network-based automatic modulation classification technique. *2016 Int. Conf. Inf. Commun. Tech. Conv. (ICTC 2016)*, pp. 579–582.

Kulin, M., Kazaz, T., Moerman, I. & de Poorter, E. (2018). End-to-end learning from spectrum data: a deep learning approach for wireless signal identification in spectrum monitoring applications. *IEEE Access*, **6**: 18484–18501.

Lee, D., Lim, M., Park, H., Kang, Y., Park, J.S., Jang, G.J. & Kim, J.H. (2017). Long short-term memory recurrent neural network-based acoustic model using connectionist temporal classification on a large-scale training corpus. *China Commun*, **14**: 23–31.

Lee, J. H., Kim, J., Kim, B., Yoon, D. & Choi, J. W. (2017). Robust automatic modulation classification technique for fading channels via deep neural network. *Entropy*, **19**: 454.

Liang, Q., Liu, X., Na, Z. Wang, W., Mu, J. & Zhang, B. (2018). *Communications, Signal Processing and Systems*. Springer, Singapore

Marsland, S. (2011). *Machine Learning: An Algorithmic Perspective*. Chapman and Hall/CRC, Florida, US.

Miller, S. (2013). *Upgrading and Repairing PCs*. Pearson Education Inc., New York, US.

O'Shea, T. J., Corgan, J., & Clancy, T. C. (2016). Convolutional radio modulation recognition networks. *Int. Conf. Eng. Appl. of Neural Netw.*, 2 -5 September 2016, Aberdeen, UK, , pp. 213–226.

Oh, K.S. & Jung, K. (2004). GPU implementation of neural networks. *Pattern Recognit.*, **37**: 1311–1314.

O'Shea, T.J., Pemula, L., Batra, D. & Clancy, T.C. (2017). Radio transformer networks: Attention models for learning to synchronize in wireless systems. *50th Asilomar Conf. Signals Syst. Comput. (ACSSC 2016)*, pp. 662–666.

Peng, S., Jiang, H., Wang, H., Alwageed, H. & Yao, Y. D. (2017). Modulation classification using convolutional neural network based deep learning model. *26th Wireless. Optic. Comm. (WOCC 2017)*, New Jersey, US.

Peng, S., Jiang, H., Wang, H., Alwageed, H., Zhou, Y., Sebdani, M.M. & Yao, Y.D. (2019). Modulation classification based on signal constellation diagrams and deep learning. *IEEE T. Neur. Net. Lear.*, **30**: 718–727.

Pérez-Neira, A.I. & Campalans, M.R. (2009). Cross-*Layer Resource Allocation in Wireless Communications: Techniques and Models from PHY and MAC Layer Interaction*. Academic Press, Massachusetts, US.

Perre, L. van der, Dejonghe, A. & Craninckx, J. (2009). *Green Software Defined Radios: Enabling Seamless Connectivity While Saving on Hardware and Energy*. Springer, Berlin, Germany.

Rao, C. R., Subba Rao, T. & Subba Rao, S. (2012). *Handbook of Statistics 30 Time Series Analysis: Methods and Applications*. Elsevier, Amsterdam, Netherlands.

Schwartz, M. (2005). *Mobile Wireless Communications*. Cambridge University Press. Cambridge, UK.

Steinkraus, D., Buck, I. & Simard, P. Y. (2005). Using GPUs for machine learning algorithms. *Proc. 8th Int. Conf. Doc. Anal. Recognit. (ICDAR 2005)*, pp. 1115–1120.

Tse, D., & Pramod, V. (2005). *Fundamentals of Wireless Communication*. Cambridge University Press.

Vishnukumar, H. J., Butting, B., Muller, C. & Sax, E. (2018). Machine learning and deep neural network - artificial intelligence core for lab and real-world test and validation for ADAS and autonomous vehicles: AI for efficient and quality test and validation. *2017 Intell. Syst. Conf., (IntelliSys 2017)*, pp. 714–721.

Wang, Yan, Zhang, H., Sang, Z., Xu, L., Cao, C. & Gulliver, T. A. (2019). Modulation classification of underwater communication with deep learning network. *Comput. Intel. and Neurosc. 2019*,, pp. 1–12.

Wang, Yu, Liu, M., Yang, J. & Gui, G. (2019). Data-driven deep learning for automatic modulation recognition in cognitive radios. *IEEE T. Veh. Technol.*, **68**: 4074–4077.

West, N. E., & O'Shea, T. (2017). Deep architectures for modulation recognition. *2017 IEEE Int. Symp. Dynam.* (DySPAN 2017), 6-9 March 2017, Maryland, US.

Wu, Y., Li, X., & Fang, J. (2018). A deep learning approach for modulation recognition via exploiting temporal correlations. *19th IEEE Workshop Signal Process. Adv. Wirel. Commun. (SPAWC 2018)*, pp. 1–5.

Yang, C., He, Z., Peng, Y., Wang, Y., & Yang, J. (2019). Deep learning aided method for automatic modulation recognition. *IEEE Access*, **7**: 109063–109068.

Zhang, M., Zeng, Y., Han, Z., & Gong, Y. (2018a). Automatic Modulation Recognition Using Deep Learning Architectures. *19th IEEE Worksh. Signal Process. Adv. Wirel. Commun. (SPAWC 2018)*, pp. 1–5.

Zhang, Q., Xu, Z., & Zhang, P. (2018b). Modulation recognition using wavelet-assisted convolutional neural network. *Int. Conf. Adv. Technol. Commun*. 2018, pp. 100–104.

UNMANNED AERIAL VEHICLES IN SEARCH AND RESCUE OPERATIONS: A REVIEW OF CHALLENGES FOR SEAMLESS ASSISTED WIRELESS COMMUNICATION CONNECTIVITY

Mohd Rizal Jasman & Kamaludin Mohamad Yusof*

Department of Communications Engineering & Communication Networks System Technology (CNets), School of Electrical Engineering, Faculty of Engineering, Universiti Teknologi Malaysia (UTM), Malaysia

*Email: kamalmy@utm.my

ABSTRACT

The utilisation of unmanned aerial vehicles (UAVs) for assisted wireless communications during search and rescue (SAR) operations over land or water, by day or night, requires special attention among operational planners and teams due to the challenges to fulfil the operational demanda. This paper discusses the problems that occur due to UAVs' strengths and weaknesses, as well as environmental features to assist SAR teams in executing their missions efficiently within the specified operational timeframe. The discussion and analysis are based on a few research works via field experimental and simulation results that have been conducted widely. As a result, the correlation between UAV characteristics and the surrounding nature significantly affects the onboard energy management, signal performance and quality during SAR operations. This paper concludes that SAR operational planners and executors must consider UAV capabilities and components, communication systems, as well as environmental features to accommodate seamless communication connectivity.

Keywords: *Search and rescue (SAR); seamless connectivity; unmanned aerial vehicle (UAV) wireless communication; signal performance; handover management.*

1. INTRODUCTION

The entire world has witnessed several natural disasters with vast numbers of death; the Centre for Research via Emergency Events Database (EM - DAT) recorded a death toll of 39,266 lives between 2016 and 2020 worldwide as a result of major natural disasters such as earthquakes, floods and storms (Table 1). During this vital time, search and rescue (SAR) operations are essential to identify and rescue the survivors in the shortest possible time, without any delays that can reduce the victims' chances of survival (Mohamed *et al*., 2015). SAR teams and the survivors depend on the availability of communications for immediate assistance and to obtain a rapid overview of the situation in a critical time. However, disasters also cause damage to communication infrastructure, resulting in difficulty to have proper means of communications in the disaster affected areas, which poses a significant challenge for SAR teams to perform their duties (Sonia & Niki, 2010; Ebtehal, Shahad & Anis, 2019; Kirtan *et al*., 2019). The role of unmanned aerial vehicles (UAVs) during SAR operations have widely brought attention to researchers and various government agencies related to this area. However, a few challenges must be addressed to ensure seamless connectivity between UAVs and ground users as discussed in this paper.

In general, there are two categories of UAVs, which are rotary-wing and fixed-wing. Each class has its strengths and weaknesses. Fixed-wing UAVs can travel at high speed and carry a heavy payload, but they must maintain continuous forward motion to retain on-air altitude and cannot be used for stationary implementation or close inspections. In comparison, rotary-wing UAVs such as quadcopters can travel in any direction and remain stationary in the air, but have limited mobility.

Therefore, the choice of UAV relies critically on the applications during the SAR operation (Matos *et al*., 2013; Luo *et al.,* 2019*;* Ignacio *et al.*, 2021).

Table 1: Total deaths from major natural disasters between 2015 and 2019 as recorded by the Centre for Research via Emergency Events Database (EM-DAT).

Disaster Type	Total Death				
	2016	2017	2018	2019	2020
Flood	4,731	3,331	2,859	5,054	6,171
Storm	1,797	2,510	1,593	2,468	1,722
Earthquake	1,315	1,012	4,321	186	196

As discussed in several research works, the utilisation of UAVs in SAR operations improves signal capacity, and rapidly restores and enhances seamless communication connectivity as relay nodes to establish communication between isolated ground user clusters such as SAR teams and disaster areas survivors. This is due to their rapid and versatile deployment and effective line of sight (LoS) communication links (Sonia & Niki, 2010). Unlike manned aircrafts and helicopters that need time to be fully prepared for missions, UAVs can be launched immediately with less preparation (Hassanalian & Abdelkefi, 2017). In addition, UAVs are mounted with various sensors, such as camera, thermal camera, Wi-Fi and voice signal sensors, which significantly assists SAR teams to detect survivors efficiently.

The deployment of UAVs for communications could be used differently, especially during SAR operations depending on two scenarios. The main purpose of mounting communication transceivers is to assign stationary locations and act as intermediaries for connecting mobile devices to ground base stations (GBS) as well as to form relay networks for data collection and data ferrying, which are commonly referred to as UAV-assisted communications (Mozaffari *et al*., 2017; Chen *et al*., 2018; Azari *et al*., 2019; Zeng *et al*., 2019; Euler *et al*., 2019; Amer *et al*., 2020) as depicted in Figure 1. Secondly, UAV-to-UAV transmissions can occur so that a mobile device linked to one UAV may bind to a mobile device connected to another UAV, which is commonly referred to as cellular-connected UAVs (Chen *et al*., 2018; Azari *et al*., 2019; Zeng *et al*., 2019; Amer *et al*., 2020) as depicted in Figure 2.

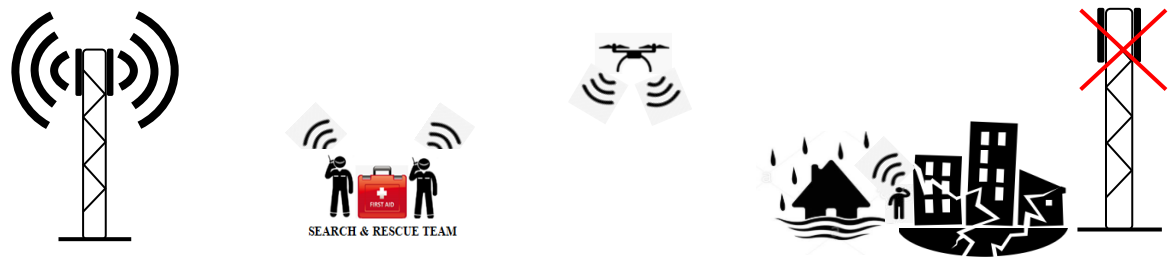

Figure 1: UAV assisted communications.

Figure 2: Cellular connected UAVs.

This paper intends to study the parameters identified by other researchers on the utilisation of UAVs for assisted wireless communications during SAR operations. The parameters covered will include the field of GBS characteristics, UAV flight altitude, energy management, propagation of environmental effects and handover management. It is hoped that this paper will provide some ideas towards the considerations that should be taken into account by the authorities when deploying UAVs for SAR operations.

2. GROUND BASE STATION (GBS) CHARACTERISTICS

The typical height of traditional terrestrial GBS installation is 25 m for urban macro (UMa) and 10 m for urban micro (UMi). At the same time, mounted GBS antennas are positioned primarily to support ground user equipment (UE) and tilted down to provide optimum throughput. Commercial UAVs usually fly without any permit up to an altitude of 120 m (Mozaffari *et al*., 2019). As a result of these limitations, signal performance is significantly influenced by the main and side lobes from the radiation pattern of a down tilted antenna as the UAV is flying and moving in 3D direction (Figure 3). Even though GBS antennas are angled down towards the ground, adequate signal coverage can be achieved up to certain altitudes. For example, based on the results reported by Zeng *et al*. (2019), adequate signal coverage for altitudes up to 122 m can still be achieved, with the UAV able to detect 18 GBS with a maximum range of 18.5 km (Zeng *et al*., 2019). Connection coverage and measurable can be significantly improved conditions through parameters such as antenna tilt, altitude and beamwidth (Azari *et al.*, 2019). By studying the impact of GBS height and antenna tilt angle on UAVs and UE, SAR operation planners can consider dynamic planning considerations such as optimal distance and placement of UAV for desired signal coverage in disaster areas.

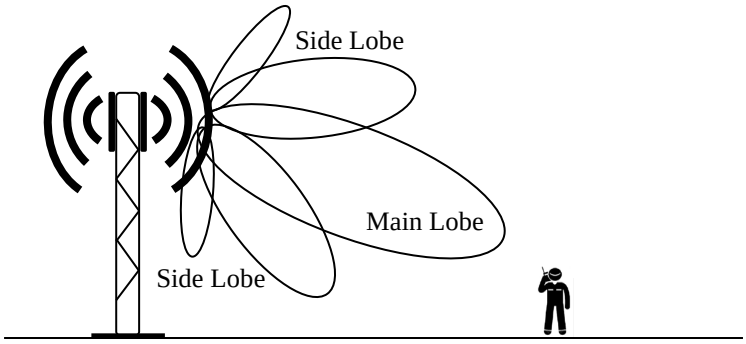

Figure 3: GBS association with UAV connecting to side and main lobes (Angjo *et al*., 2021)**.**

3. UAV ALTITUDE

UAV operations may be a part of an integrated airspace accessed with manned aircrafts, or certain airspace zones may be allocated for UAVs with authorised aerial platforms only. Aerial platforms can be identified based on their height. A structure with a height of 1 km is labelled as a terrestrial platform. Low altitude platform (LAP) systems employ altitudes between 1 and 12 km. Aircrafts flying at 17 to 50 km altitude are identified high altitude platform (HAP). Quasi-stationary aerial platforms, including quadcopters, balloons and helicopters, are usually characterised as troposphere laying altitude (Al-Hourani *et al*., 2014). UAV altitude is defined as the maximum height that UAVs can achieve, irrespective of country-specific rules. The Third Generation Partnership Project (3GPP) Release -15 allows permitted altitude and speed of UAVs of 300 m and 160 km/h respectively, and UAVs of up to 100 m altitude can transmit data from GBS in the radius of 10 km (Amorim *et al.*, 2017; 3GPP, 2019). The association between all the UAV authorised LAP altitudes are shown in Figure 4.

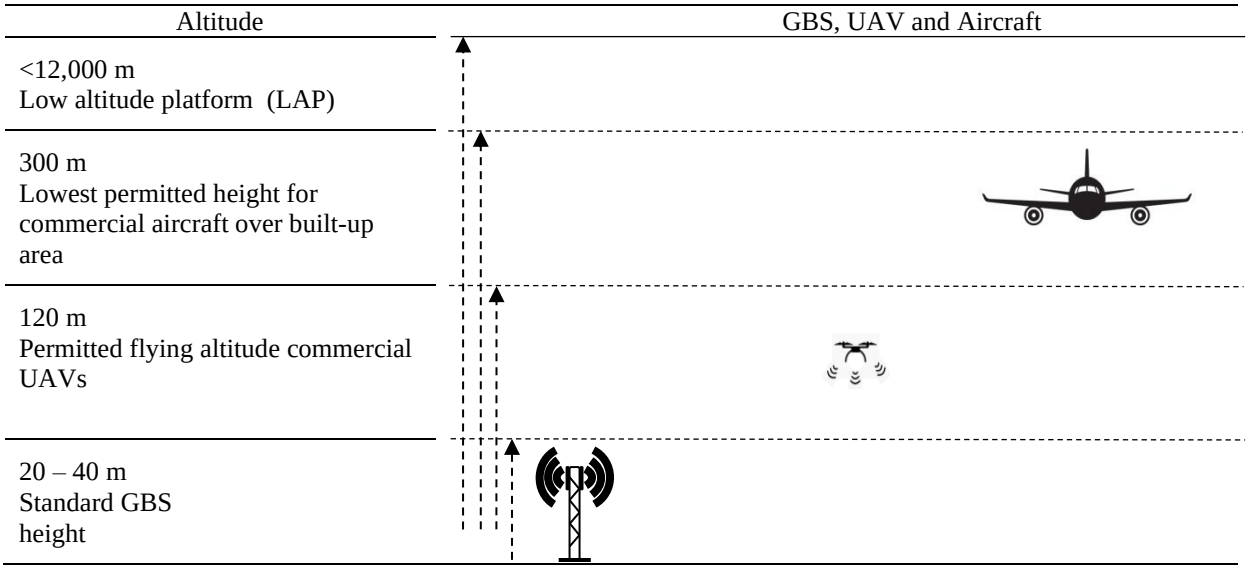

Figure 4: LAP association with UAV altitude.

In addition, for cost-effective and fast rollout, UAV operations at LAP play a crucial role in deriving achievable performance and providing short-range LoS links that can dramatically improve signal quality on the requirements of quality of service (QoS), minimise interference such as signal blockage and multipath scattering, as well as maximise ground coverage (Zeng *et al*., 2016). While communication with LoS is typically feasible with deployment of UAVs, the signal becomes weaker in restricted coverage, such as when blocked by buildings in metropolitan areas, under crowns of trees and indoors. Application of amplification-and-forward (AF), and decode-and-forward (DF) has been proven to be able to reduce the risk of failure, reduce power requirements and improve bit error rate success, which will increase the chance of successful transmission between ground users (Chen *et al*., 2018). In correlation with GBS and drone flying altitude, UAVs of up to 100 m altitude can transmit data from GBSs in a radius of 10 km (Amorim *et al.,* 2017).

4. UAV ENERGY MANAGEMENT

In general, UAVs require effective energy consumption management to maximise their operational period. For a UAV used for communication purposes, energy consumption consists of two principal components, which are communication platform and propulsion. Hence, it is important to properly manage both modules efficiently to allow the UAV to operate for the minimum tolerable period before exhausting its power source (fuel or battery) (Sboui *et al*., 2017; Mozaffari *et al*., 2019). A UAV's energy endurance depends on its role / mission, weather condition, length of operation and distance covered. On the other hand, the energy consumption of the communication platform is focused on multiple tasks such as computation, signal transmission and signal processing (Khan *et al.*, 2019; Angjo *et al.*, 2021).

The communication module of a UAV can be divided into two parts, which are control and non-payload communication (CNPC), and payload communication. The CNPC connection is used to control UAVs remotely and to check telemetry data in real-time. CNPC typically operates at low data rates but has rather stringent requirements for ultra-reliability, high security and low latency (Zeng *et al*., 2019). The communication payload covers mission-related information transmission between UAVs and ground users, such as live video surveillance and wireless relay services, which typically requires much faster bandwidth, such as ultra-high-definition video (UHDV) streaming. When deployed as an essential component during SAR operations, UAVs must transmit or receive mission-related data from different ground agencies, including end-users and UAV operators. Table 2 summarises UAV downlink and uplink specifications for both communication links defined in 3GPP.

Table 2: UAV downlink and uplink communication links specified by 3GPP.

Requirement	Data Rate	Reliability	Latency	Data Type
Uplink	60 – 100 Kbps	Up to 10^{-3} Packet Error Loss Rate	50 ms	Command and Control
	Up to 50 Mbps	-	Similar to terrestrial user	Application Data
Downlink	60 – 100 Kbps	Up to10^{-3} Packet Error Loss Rate	-	Command and Control

The operational endurance of UAVs is based on their energy consumption, which is influenced by multiple factors, such as type of drone, flight conditions, climbing speed, payload, physical parameters (geometrical shape such as wingspan, wing shape and airfoil), as well as weather conditions. The cruise speed of UAVs can be improved by reducing drag and thus reducing the energy used (Otto *et al*., 2018). For example, due to limited onboard energy storage capacity, micro-UAVs (operated with battery) have restricted flight durations of up to 30 min (Hassanalian *et al*., 2014). In addition to the parameters mentioned, energy consumption, especially in multi-rotors, is critical since the batteries that power them have limited endurance.

Flying at LAP exposes UAVs to atmospheric disturbances, particularly turbulence, air density and adverse weather conditions. As a result, UAVs never stop consuming energy because they must maintain their weight in the air the entire time. It is even more critical in rotary-wing UAV since they do not have enough wing surfaces to provide a lifting phenomenon (as in fixed-wing UAV), and the propulsion system must generate all the thrust. In this case, one way to save energy in quadrotors is minimising time in the air. As a consequence, the aircraft has to move as fast as possible. However, if the quadrotor moves faster, a loss of lift is produced due to a greater inclination of its rigid body. This requires more effort from the propulsion system to generate the same weight component in the vertical axis to allow the quadrotor to remain at the same altitude (Daniel *et al*., 2017). The electrical energy consumed by the motors depends on the thrust requirements and includes electrical losses due to heat and friction, and overall propulsion system efficiency (Mohiuddin *et al*., 2019). Therefore, it is paramount for SAR planners to consider these factors as it has significant impacts on UAV performance.

5. HANDOVER MANAGEMENT

Another challenge of UAV deployment as an assisted communication platform in SAR operations is the handover management process. Handovers correspond to the switching between network nodes of services or sessions (Kuklinski *et al*., 2014). Prolonged UAV missions will consume the onboard energy, which entails other faults. They may shut down their communication interfaces to conserve energy. It is essential to identify the trigger to execute the handover process between the inflight UAV and incoming UAV to ensure seamless communication is achieved under the specific criteria established, as presented in Figure 5. Handover enables complete consistency of network connectivity during the handover phase with just a tiny increase in message latency (Ohleger *et al*., 2013). The latency of transmission and the loss of data packets during the handover operation will cause significant impairment of user-perceived device efficiency and QoS (Gupta *et al*., 2016).

In order to achieve seamless communication, the transition protocol will involve a series of data messages exchanged between the mobile user, an in-flight UAV node and the incoming UAV node to which the data transmission of this user will be transferred. As shown in Figures 6 and 7, the transmission process leads to the transition of data packet connectivity through the in-flight UAV to the incoming UAV.

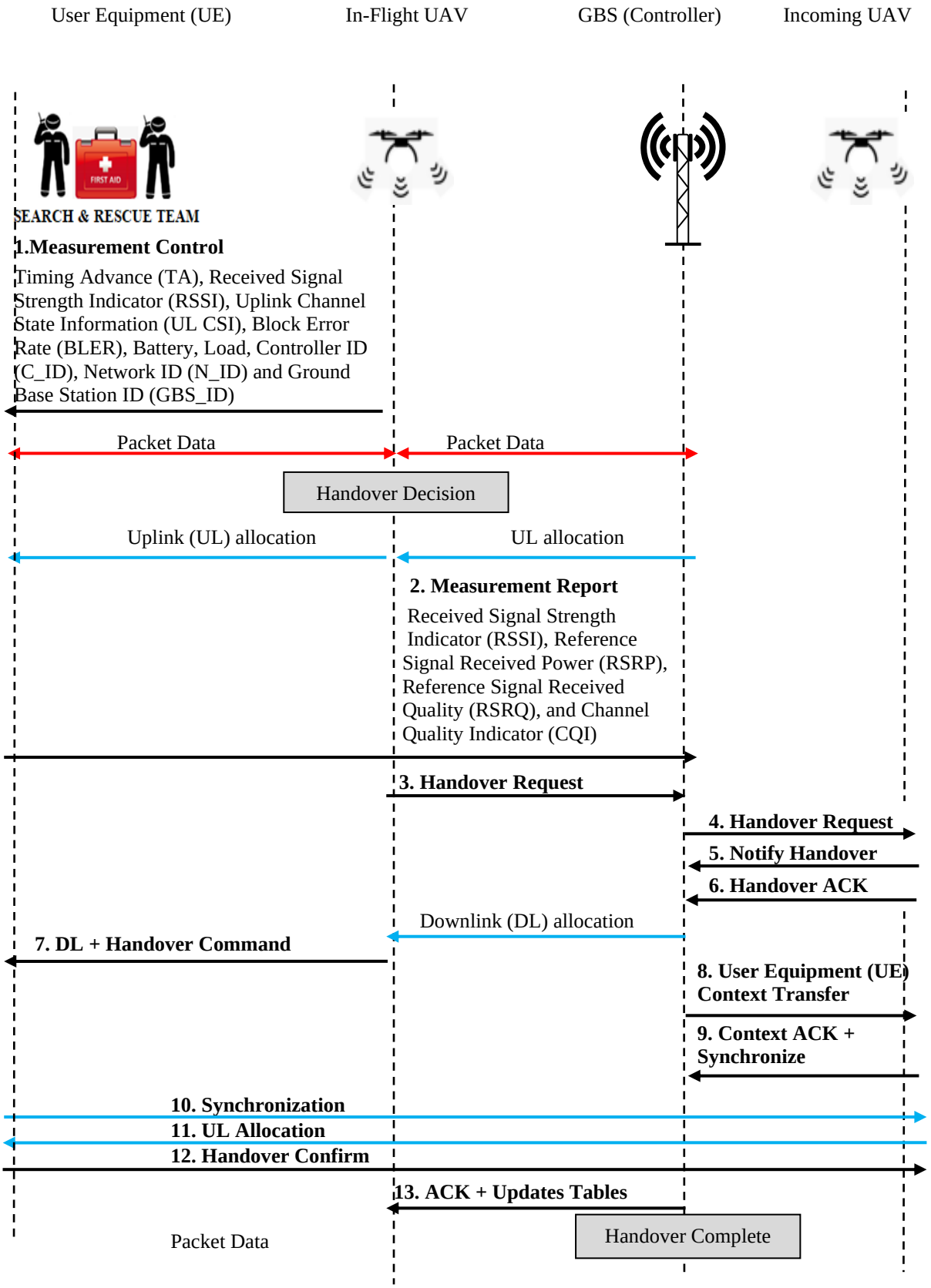

Figure 5: UAV to UAV handover process.

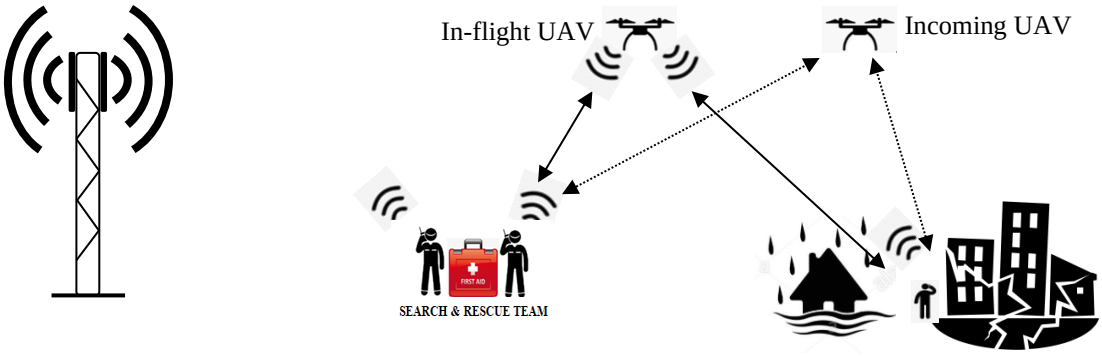

Figure 6: The incoming UAV is deployed and ready before breaking transmission with the in-flight UAV.

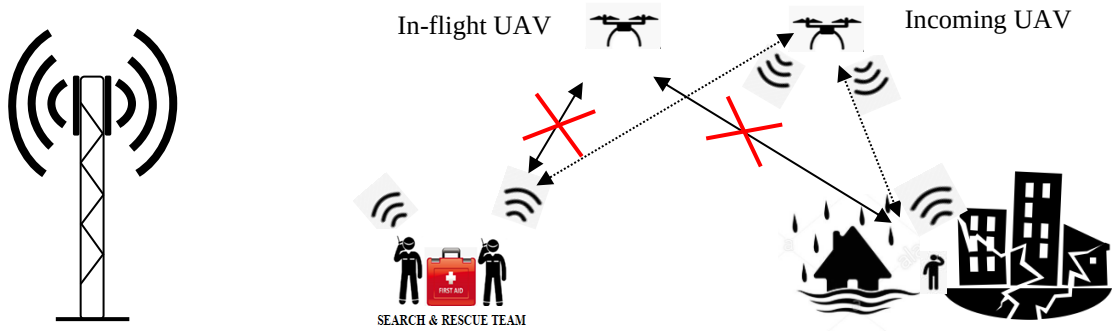

Figure 7: Completed handover between the in-flight and incoming UAVs.

When the transition of the UAV is conducted in this manner, the logical sequence of the process would include a trigger, deployment of the incoming UAV, network discovery and changeover. Before the handover, the deciding factors for the handover are received signal strength (RSS), available bandwidth, altitude and UAV speed (Park *et al*., 2016). The RSS is obtained from each wireless access point, which is continuously assessed, with the transfer of data being evaluated by comparing these values with the threshold set beforehand on both UAVs. In addition, the handover trigger decision is made from a wireless network with the maximum bandwidth available, network load, channel condition, signal-to-interference-plus-noise ratio (SINR) and other factors (Lee *et al.*, 2017).

For high-altitude UAV flights, LoS propagation conditions may cause some interferences to the designated GBS. When this situation occurs, the UAV-UE cannot maintain network links, leading to higher handover failures and frequent handovers to other nearby GBS, interfering with the handover process (Fakhreddine *et al*., 2019). Frequent handovers will cause additional issues, including power consumption, packet losses and communication delays (Lee *et al.*, 2017).

In order to minimise failures, Park *et al*. (2016) proposed the principles of seamless handover performance potential and false handover initiation possibility for optimum coverage and seamless handover efficiency evaluation for UAVs used as a Wi-Fi access point. Hu *et al*. (2019) proposed another method using a deep learning model to analyse and measure multi-pedestrian movement behaviour and positions of mobile users for the handover decision of UAV cellular networks.

6. PROPAGATION ENVIRONMENT EFFECT

The radio signal transmitted from a UAV propagates through free space until reaching the targeted environment, incurring path loss and signal fading due to shadowing, blocking, scattering, reflections, and other effects caused by buildings, structures and geographical features. Furthermore, as radio signals propagate in free space, their energy dissipates, and the amount of energy received per unit area decreases. The longer the distance, the less energy received per unit area. The path loss depends on the physical variability and the angle between the ground user and UAV. Due to the prevalence of LoS and surface reflection components, the two-ray model has mainly been employed for UAVs operating over deserts or seas, while the stochastic Rician fading model is another extensively used model in densely populated areas (Zeng *et al*., 2016). Both models are depicted in Figures 8 and 9 respectively. Achieving dominant LoS is paramount as UAVs are required to transmit and receive data, including images and videos, to the cellular network via the uplink and downlink processes from UAVs to GBS and vice versa. These processes would require multiple devices installed onboard of the UAV and hence, would increase the power consumption (Fu *et al*., 2021). Therefore, consideration of these models to reduce propagation environmental effects would allow UAVs to be effectively deployed during SAR operations and communication connectivity in disaster areas can be significantly improved.

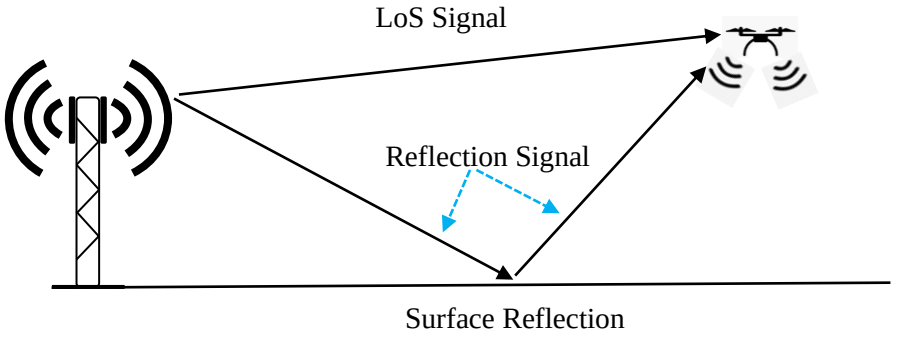

Figure 8: Two-ray model.

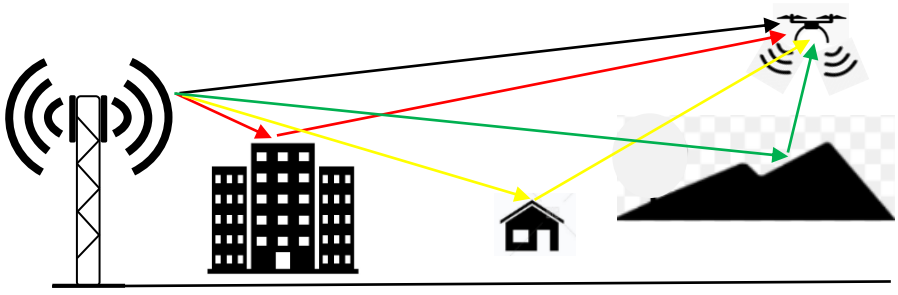

Figure 9: Rician fading model.

CONCLUSION

This paper reviewed the crucial correlation between UAV capabilities, complex telecommunication system characteristics and environmental conditions that significantly affect onboard energy management, as well as signal quality and performance. These elements are very significant in ensuring that seamless wireless communication is achieved. The strengths and weaknesses of the these factors would provide some ideas and guidance for SAR strategic, operational planners and teams to execute the missions with minimum communication interruptions.

REFERENCES

3GPP Technical Report 36.777. *Technical Specification Group Radio Access Network; Study on Enhanced LTE Support for Aerial Vehicles (Release 15)*. Available online at: https://www.3gpp.org/uas-uav (Last access date: 15 May 2020).

Al-Hourani, A., Sithamparanathan, K. & Lardner, S. (2014). Optimal LAP altitude for maximum coverage. *IEEE Wirel. Commun. Le.*, **3**: 569-572.

Amer, R., Saad, W. & Marchetti, N. (2020). Mobility in the sky: performance and mobility analysis for cellular-connected UAVs. *IEEE T. Commun.*, **68**: 3229-3246.

Amorim, R., Nguyen, H.C., Mogensen, P.E., Kovacs, I.Z., Wigard, J. & Sorensen, T.B. (2017). Radio channel modeling for UAV communication over cellular networks. *IEEE Wirel. Commun. Le.*, **6**: 514-517.

Angjo, J., Shayea, I., Ergen, M., Mohamad, H., Alhammadi A. & Daradkeh, Y., (2021). Handover management of drones in future mobile networks: 6G technologies. *IEEE Access.*, **9**: 12803-12823.

Azari, M.M., Rosas, F. & Pollin, S. (2019). Cellular connectivity for UAVs: network modeling, performance analysis, and design guidelines. *IEEE T. Wirel. Commun.*, **18**: 3366-3381.

Azari, M.M., Rosas, F. & Pollin, S. (2018). Reshaping cellular networks for the sky: major factors and feasibility. *2018 IEEE Int. Conf. Comm. (ICC 2018), 20-24 May 2018, Kansas City, Missouri, US.*

Bronz, M., Moschetta, J., Brisset, P. & Gorraz, M. (2009). Towards a long endurance MAV. *Int. J. Micro. Air. Veh.*, **1**: 241-254.

Centre for Research on the Epidemiology of Disasters (2020). *Emergency Events Database (EM-DAT)*. Available online at: https://www.cred.be/projects/EM-DAT (Last access date: 18 June 2020).

Chen, Y., Feng, W. & Zheng, G. (2018). Optimum placement of UAV as relays. *IEEE Commun. Lett.*, **22**: 248-251.

Choi, D.H., Kim, S.H. & Sung, D.K. (2014). Energy-efficient maneuvering and communication of a single UAV-based relay. *IEEE T. Aero. Elec. Sys.*, **50**: 2320-2327.

Civil Aviation Authority of Malaysia (2020). *Frequently Asked Questions (FAQ) on Unmanned Aircraft System (UAS)*. Available online at: https://www.caam.gov.my/aviation-professionals/faq/faq-on-unmanned-aircraft-system-uas/ (Last access date: 15 May 2020).

Daniel, C., Gandolfo. L., R. Salinas., Brandao & Toibero, J.M. (2017). Stable path-following control for a quadrotor helicopter considering energy consumption. *IEEE T. Contr. Sys.T.*, **25**: 1423-1430.

Dorling, K., Heinrichs, J., Messier, G.G. & Magierowski, S. (2017). Vehicle routing problems for drone delivery. *IEEE T. Syst. Man. Cy-S.*, **47**: 70-85.

Ebtehal, T., Shahad, S. & Anis, K.,. (2019). LSAR: multi-uav collaboration for search and rescue missions. *IEEE Access.*, **7**: 55817-5583.

Euler, S., Maattanen, H., Lin, X., Zou, Z., Bergström, M. & Sedin, J. (2019). Mobility support for cellular connected unmanned aerial vehicles: performance and analysis. *IEEE Wcnc.*, pp.1-6.

Fakhreddine, A., Bettstetter, C., Hayat, S., Muzaffar, R. & Emini, D. (2019). Handover challenges for cellular-connected drones. *DroNet'19 Proc. 5th Workshop on Micro Aerial Veh. Sys. and Appl.*, pp. 9-14.

Fotouhi, A., Qiang, H., Ding, M., Hassan, M., Giordano, L.G., García-Rodríguez, A. & Yuan, J. (2018). Survey on UAV cellular communications: practical aspects, standardization advancements, regulation, and security challenges. *IEEE Commun. Surv. Tut.*, **21**: 3417-3442.

Fu, X., Ding, T., Peng, R., Liu, C. & Cheriet, M. (2021). Joint UAV channel modeling and power control for 5G IoT networks. *EURASIP J. Wireless Comm. Netw.*, **Vol, 2021**: 106..

Gupta, L., Jain, R. & Vaszkun, G. (2016). Survey of important issues in UAV communication networks. *IEEE Commun. Surv. Tut.*, **18**: 1123-1152.

Hassanalian, M. & Abdelkefi, A. (2017). Classifications, applications, and design challenges of drones: a review. *Prog. Aerosp. Sci.*, **91**: 99-131.

Hassanalian, M., Radmanesh. M. & Sedaghat, A. (2014). Increasing flight endurance of MAVs using multiple quantum well solar cells. *Int. J. Aeronaut. Space.*, **15**: 212-217.

Hu, B., Yang, H., Wang, L. & Chen, S. (2019). A trajectory prediction based intelligent handover control method in UAV cellular networks. *China Commun.*, **16**: 1-14.

Ignacio, M., Golcarenarenji, G., Wang, Qi. & Alcaraz, J., (2021). Search and rescue operation using UAVs: A case study. *Expert Syst. Appl*., **178**: 114937.

Khan, M., Qureshi, I. & Khanzada, F., (2019). A hybrid communication scheme for efficient and low-cost deployment of future flying ad-hoc network (FANET). *Drones*, **3**: 16.

Kirtan, G., Panda, S., Das., S. & W., Arif. (2019). Design and deployment of uav-aided post-disaster emergency network. *IEEE Access.*, **7**: 102985-102999.

Kuklinski, S., Li, Y. & Dinh, K.T. (2014). Handover management in SDN-based mobile networks. *IEEE Globecom Work. 2014*, pp. 194-200.

Lee, E., Choi, C. & Kim, P. (2017). Intelligent handover scheme for drone using fuzzy inference systems. *IEEE Access.*, **5**: 13712-13719.

Li, B., Fei, Z., Dai, Y. & Zhang, Y. (2018). Secrecy-optimized resource allocation for UAV-assisted relaying networks. *IEEE Glob. Telecomm. Conf. 2018*, pp. 1-6.

Luo C., Miao, W., Ullah, H., McClean, S., Parr, G., & Min, G. (2019). Unmanned aerial vehicles for disaster management. *In*, Durrani T., Wang W., Forbes S. (Eds.), *Geological Disaster Monitoring Based on Sensor Networks*., Springer, Singapore, pp. 83-107.

Matos, A., Silva, E., Cruz, N.A., Alves, J.C., Almeida, D.M., Pinto, M., Martins, A., Almeida, J.M. & Machado, D. (2013). Development of an unmanned capsule for large-scale maritime search and rescue. *2013 OCEANS Conf.*, 23-27 September 2013.

Mohamed, A., Abdulrahim, M., Watkins, S. & Clothier, R. (2015). Development and flight testing of a turbulence mitigation system for micro air vehicles. *J. Field. Robot.*, **33**: 639-660.

Mohiuddin, A., Taha, T., Zweiri, Y. & Dongming, Gan., (2019). UAV payload transportation via RTDP based optimized velocity. *Energies*, **12**: 3049.

Mozaffari, M., Saad, W., Bennis, M., Nam, Y.H. & Debbah, M. (2019). A tutorial on UAVs for wireless networks: applications, challenges, and open problems. *IEEE Commun. Surv. Tut.*, **21**: 2334-2360.

Mozaffari, M., Saad, W., Bennis, M. & Debbah, M. (2017). Wireless communication using unmanned aerial vehicles (UAVs): optimal transport theory for hover time optimization. *IEEE T. Wirel. Commun.*, **16**: 8052-8066.

Mozaffari, M., Kasgari, A.T., Saad, W., Bennis, M. & Debbah, M. (2019). Beyond 5G with UAVs: foundations of a 3d wireless cellular network. *IEEE T. Wirel. Commun.*, **18**: 357-372.

Ohleger, M., Xie, G.G. & Gibson, J.H. (2013). Extending UAV video dissemination via seamless handover: a proof of concept evaluation of the IEEE 802.21 Standard. *IEEE 46th Hawaii Int. Conf. on Syst. Sci.*, 7-10 January 2013.

Otto, A., Agatz, N.A., Campbell, J.F., Golden, B.L. & Pesch, E. (2018). Optimization approaches for civil applications of unmanned aerial vehicles (UAVs) or aerial drones: A survey. *Networks.*, **72**: 411-458.

Park, K., N., Kang, H., Cho, M., Park, J. & Kim, H. (2016). Handover management of net-drones for future internet platforms. *Int. J. Distrib. Sens. N.*, **12**: 5760245.

Qi, X., Li, B., Chu, Z., Huang, K., Chen, H. & Fei, Z. (2019). Secrecy energy efficiency performance in communication networks with mobile sinks. *Phys. Commun.*, **32***:* 41-49.

Sboui, L., Ghazzai, H., Rezki, Z. & Alouini, M. (2017). Energy-efficient power allocation for UAV cognitive radio systems. *IEEE 86th Veh. Technol. Conf.*, 24-27 September 2017.

Sonia, W. & Niki, T (2010), Supporting search and rescue operations with UAVs. *Int. Conf. Emerging Secur. Technol. (EST).*, 6-7 September 2010.

Sun, R. & Matolak, D.W. (2017). Air - ground channel characterization for unmanned aircraft systems part II: hilly and mountainous settings. *IEEE T. Veh. Technol.*, **66**: 1913-1925.

Zeng, Y., Wu, Q. & Zhang, R. (2019). Accessing from the sky: a tutorial on UAV communications for 5G and beyond. *P. IEEE.*, **107**: 2327-2375.

Zeng, Y. & Zhang, R. (2017). Energy-efficient UAV communication with trajectory optimization. *IEEE T. Wirel. Commun.*, **16**: 3747-3760.

Zeng, Y., Zhang, R. & Lim, T.J. (2016). Wireless communications with unmanned aerial vehicles: opportunities and challenges. *IEEE Commun. Mag.,* **54***:* 36-42.

Zeng, Y., Lyu, J. & Zhang, R. (2019). Cellular-connected UAV: potential, challenges, and promising technologies. *IEEE Wirel. Commun.,* **26**: 120-127.

Zorbas, D., Razafindralambo, T., Pugliese, L.D. & Guerriero, F. (2013). Energy efficient mobile target tracking using flying drones. *4th Int. Conf. on Ambient Syst. Net. and Technol. (ANT)*., **19**: 80-87.

EXPERIMENTAL EVALUATION OF SOLAR CHARGE CONTROLLER INSTALLED IN A SOLAR-POWERED UNMANNED AERIAL VEHICLE (UAV)

Shahrul Ahmad Shah*, Sabarina Abdul Hamid, Nadhiya Liyana Mohd Kamal, Nurhakimah Norhashim, Zulhilmy Sahwee, Aiman Rafael Rasha Azaldin & Muhamad Izwan Zolkifli

Universiti Kuala Lumpur, Malaysian Institute of Aviation Technology (UniKL MIAT), Malaysia

*Email: shahrul@unikl.edu.my

ABSTRACT

Electrically powered unmanned aerial vehicle (UAV) flight duration is limited by its capacity to carry the on-board battery. One of the methods to extend flight duration is by installing a string of solar cells into the UAV. Researchers have found that a good electrical connection between solar panels and the on-board electrical networks affects the output efficiency. Poor wiring connectivity and minor damages of solar panels contribute to loss of power and reduce the solar cells' power output. On top of the electrical physical connectivity factor, the type of solar charging system also contributes to the efficiency of the power output. Therefore, this research aims to evaluate two different types of solar charge controllers; maximum power point tracking (MPPT) and pulse width modulation (PWM). Within the on-board solar charging system, a solar charge controller is installed to track the maximum power output of the solar cells and maintain a constant output voltage from the photovoltaic (PV) cell to charge the battery using the battery charging system. From the result of this investigation, by adding the solar charge controller into the system, the voltage output from all terminals (solar panel, battery, and load) were held constant even though the solar intensity varies. These findings conclude that both MPPT and PWM solar charge controllers are able to maintain constant output voltage with varying solar intensity. The results also show that the MPPT charge controller has marginally higher efficiency as compared to the PWM charge controller when used in our UAV platform.

Keywords: *Unmanned aerial vehicle (UAV); solar cell; solar charge controller; maximum power point tracking (MPPT); pulse width modulation (PWM).*

1. INTRODUCTION

In recent years, research on unmanned aerial vehicle (UAV) technology is expanding in many fields. Many optimisations and improvements were studied to improve UAV systems. One of the targets of the UAV community is to enable the aircraft to fly continuously for longer periods (Turk *et al*., 2018). Electric-powered UAVs have few power options, such as batteries, hydrogen fuel cells and solar energy. Studies have found that solar-powered UAV is the best source to be used as compared to batteries and hydrogen fuel cells (Thipyopas *et al*., 2019).

A solar-powered UAV needs solar cells to capture solar energy from the sun. A solar cell is a device that converts light energy into electrical energy, and it is also referred to as photovoltaic or PV. A solar panel is a series of solar cells that generate energy proportionally to the amount of sunlight it receives. There are a few types of materials from which the PV cells are made, such as polycrystalline, monocrystalline and amorphous silicon (Chatta *et al*., 2018).

The monocrystalline solar cell has the highest efficiency, which is around 15-22% (Sendy, 2021). The use of this type of PV is effective in an environment with low light and small space. However, this type of solar cell is expensive and fragile. The polycrystalline solar cell has moderate efficiency of about 10-15% (Energysage, 2019), and has lower production cost and heat tolerance. Thin film is the least expensive option. It is flexible and bendable, but it has the lowest efficiency of around 10-13%

(Sendy, 2021). In this research, polycrystalline silicon solar cells are used for the experiments, with the manufacturer data of the solar cells shown in Table 1.

Table 1: Manufacturer's data of the solar cells used in this study.

Solar Cell Size	156 x 31.2 mm
Average thickness	200 µm ± 20 µm
Crystal type	Grade 'A' polycrystalline silicon
Power at Maximum Power Point (P_{mpp}), W	0.8 W
Voltage at Maximum Power Point (V_{mpp}), V	0.502 V
Current at Maximum Power Point, (I_{mpp})A	1.6 A
Open Circuit Voltage (V_{oc}), V	0.56 V
Short Circuit Current (I_{sc}), A	1.68 A
Testing Condition Irradiance	1,000 W/m^2
Temperature	25 °C

A solar-powered UAV system uses converted solar energy to power up the whole electrical and avionics system. A solar charge controller within the system is crucial as it receives varying input power from the sun throughout the day. It regulates the electrical power coming from the solar panels charging the battery, ensures that the batteries connected to the system are not overcharged during the daytime, as well as prevents reverse current during the night thus draining the batteries (Majaw *et al*., 2018). There are three types of charge controllers that are currently available, which are simple on-off charge controller, pulse width modulation (PWM) and maximum power point tracking (MPPT). Most solar-powered systems use either PWM or MPPT for their operations. PWM and MPPT charge controllers utilise two different techniques of controlling the power delivered to the system from the solar panel that differ in terms of working principle, operation performance and pricing. The conversion efficiency of MPPT is relatively 30% higher as compared to PWM (Svarc, 2020).

The experiment conducted by Nandar (2016) focused on the design of a charge controller under a controlled environment, while this paper focuses on performance analysis under actual conditions. This research aims to compare the effectiveness of using two different solar charge controllers, which are PWM and MPPT. These two types of controllers were chosen as it readily available from the market. However, the price of a MPPT charge controller is approximately ten times of that of a PWM charge controller. Thus, for low power applications, does the use of a MPPT charge controller justify the higher price it demands? The work carried herein aims to answer this question. In this research, the solar panels were installed on the wing of the UAV for measurement. However, the flight test performance of the UAV with the solar panel installed has not been carried out yet.

This paper is organised as follows: the setup of solar cells onto the wing and wiring of the solar charge controller is explained in Section 2. The results of the solar power output from the experiment based on the two types of solar charge controllers is discussed in Section 3. Finally, the concluding remarks of this paper are presented in Section 4.

2. MATERIALS AND METHODS

2.1 Solar Panel and Soldering

A total of 40 polycrystalline solar cells were soldered together using nickel tabbing wires and placed on top of a 2 m UAV wing fixed-wing UAV. Each left and right wing was installed with 20 solar cells and joined together at the centre section. Each of the solar cells has a voltage output of about 0.5 V. Figure 1 shows the solar cells being connected in a series on top of the right wing.

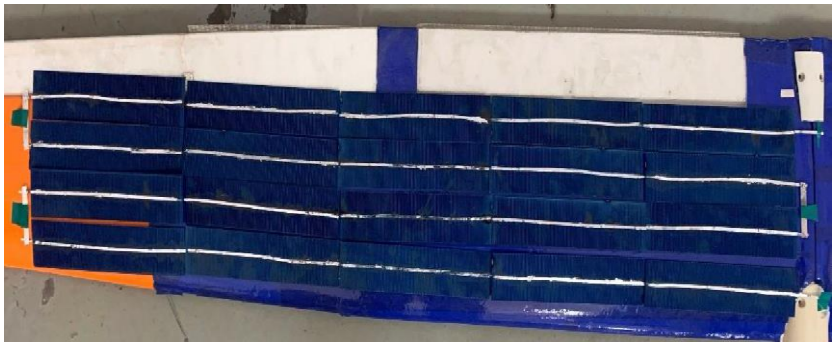

Figure 1: Series connection of the solar cells on top of the UAV wing.

2.2 Component Connection

The positive and negative terminals of both types of the charge controller are connected with the batteries' positive and negative terminals respectively. Meanwhile the solar panel's positive and negative terminals are connected to the positive and negative terminals of the charge controller. The batteries are required to be connected first, followed by the solar panel. This step is to ensure the charge controller is able to measure the voltage of the battery. Finally, the load is connected to the charge controller as seen in Figure 2.

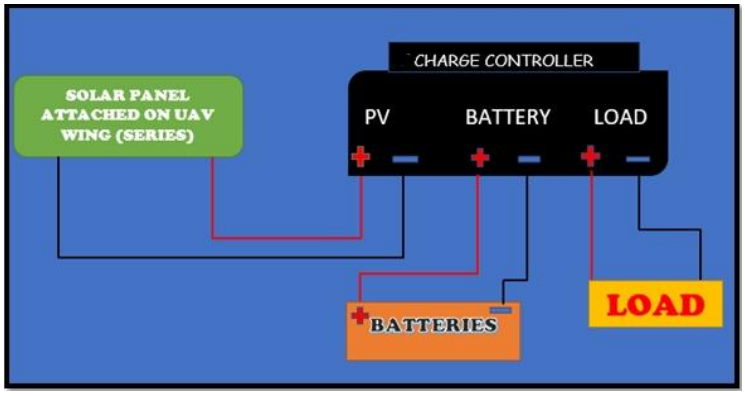

Figure 2: Solar powered UAV system connection.

2.2.1 PWM Charge Controller

A charge controller is a current or voltage regulator that prevents the battery from overcharging. It controls the voltage and current that flow from the solar panels. For example, if a 12 V rated panel produces 16 to 20 V, the batteries will be damaged if there is no regulator. A PWM charge controller reduces the amount of power supplied to the batteries when the batteries are almost fully charged as seen in Figure 3.

A PWM charge controller acts as a switch that connects the solar panel to the battery. When the switch is closed, the panel and battery will be at nearly the same voltage. The voltage increases as the state of charge of the battery is increased (Majaw *et al*., 2018). Some of the characteristics of PWM charge controller are:

a) Be able to acknowledge battery capacity changes
b) Enhance the battery's charge acceptance
c) Maximise the average battery capacity
d) Lower battery heating and gassing
e) Self-regulate for voltage drops and temperature changes in solar systems.

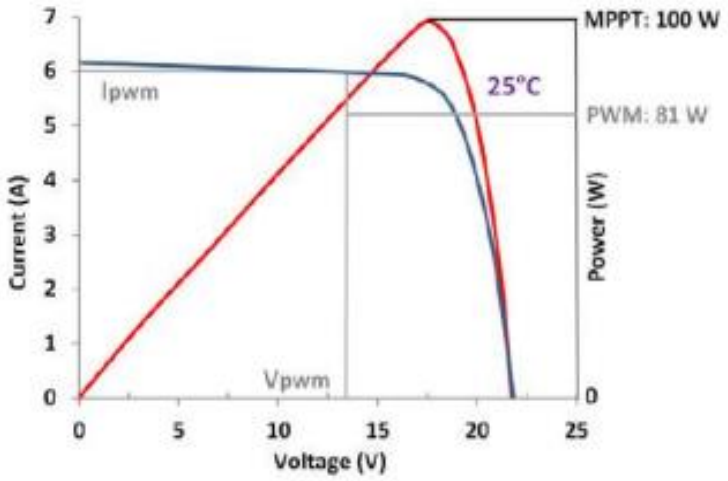

Figure 3: Charging characteristics of a PWM charge controller (Majaw *et al.*, 2018).

2.2.2 MPPT Charge Controller

A MPPT charge controller works by determining the maximum power output of the solar panel, which can be detected based on the maximum solar radiation onto the solar panel. This depends on three factors, which are solar radiation, ambient temperature and solar cell temperature (Majaw *et al.*, 2018). The power output of solar panels can then be improved using the MPPT. According to Liu (2015), a Genasun MPPT charge controller has conversion efficiency of 94 to 99.85 % (Liu, 2015). Yilmaz (2017) highlighted that the most critical step in determining the maximum power output of a PV panel is to determine its power-voltage (P-V) and current-voltage (I-V) characteristic curves. Increasing irradiance will increase the PV panel power and voltage, whereas increasing temperature decreases the power and voltage. Figure 4 shows the P-V and I-V characteristic curves under varied temperature and irradiation (Yilmaz *et al.*, 2017).

The difference between PWM and MPPT charge controllers is that PWM requires the voltage of the battery to match with the voltage of the solar panel and thus, it becomes less flexible as compared to MPPT (Sepulveda *et al.*, 2019). The MPPT controller can charge the battery better because it uses a different circuit that can use the entire output and increase the charging efficiency by 30% as compared to PWM (Svarc, 2020). In this experiment, a Genasun GV-5 MPPT solar charge controller (Figure 5) and a KYZ 10 PWM charge controller (Figure 6) are used to compare the capability to regulate the charging of the on-board batteries. The PWM charge controller has the same rated voltage across the battery bank and PV array, while the MPPT charge controller is more electronically advanced and works best under low temperatures (Ikeh, 2017). Table 2 shows the specifications of the MPPT and PWM charge controllers that were used in this study.

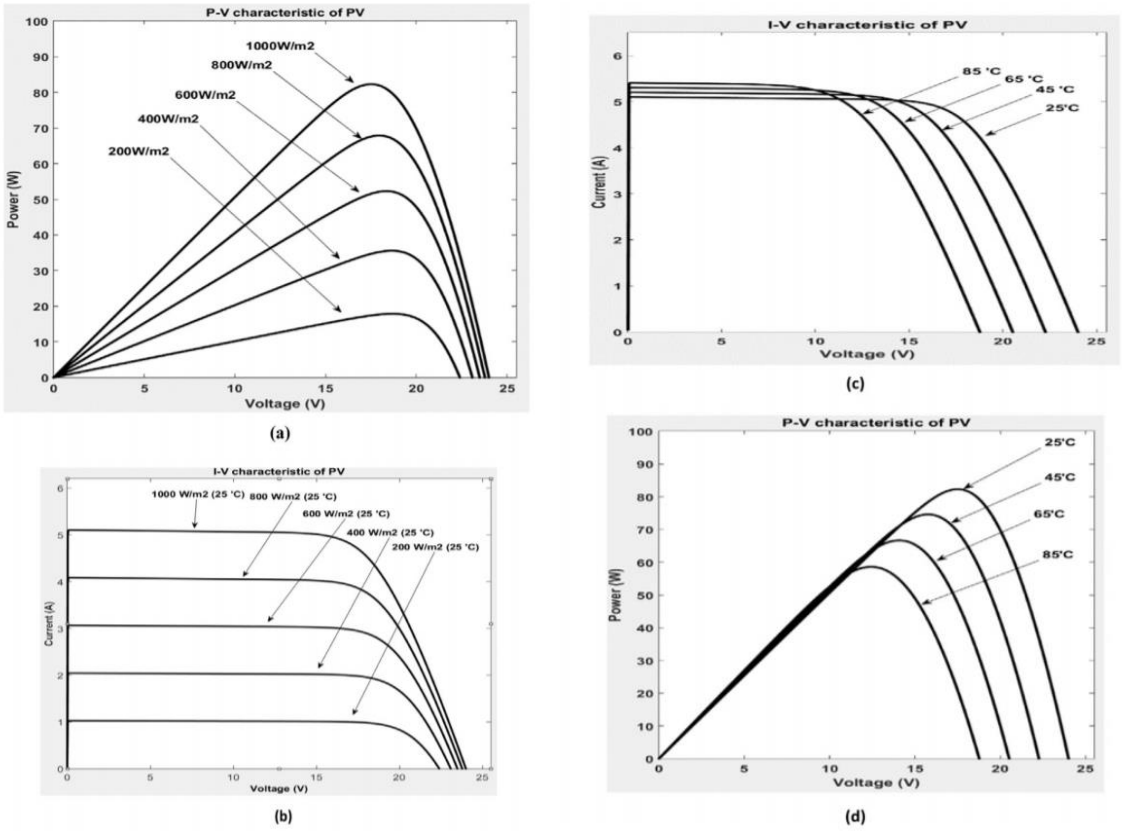

Figure 4: (a) P-V variable irradiance characteristics. (b) I-V variable irradiance characteristics. (c) I-V variable temperature characteristics. (d) P-V variable temperature characteristics (Yilmaz *et al.*, 2017).

Figure 5: The Genasun GV-5 MPPT solar charge controller used in this study.

Figure 6: The KYZ 10 PWM solar charge controller used in this study.

Table 2: Specifications of KYZ 10 PWM and Genasun GV-5 MPPT solar charge controllers used in this study.

Model	KYZ 10 (PWM)	Genasun GV-5 (MPPT)
Battery Voltage	12 / 24 V	16.7 V
Charge Current	10 A	5 A
Discharge Current	10 A	5 A
Max Solar Input	<41 V	27 V
Float	Lead acid battery : 13.7 V (defaults, adjustable range 13-15 V	Not applicable
	Lithium battery: 12.0 V (defaults, adjustable range 11.5-12.8 V)	16.7 V
Under Voltage Protection	Lead acid battery : 10.7 V (defaults, adjustable range 9-11.5 V	Not applicable
	Lithium battery: 10.7 V (defaults, adjustable range 9-11.0 V)	7.2 V
Standby Current	<10 mA	150 µA
Operating Temperature	-35 to +60 °C	-40 to 85 °C
Size / Weight	133 mm x 70 mm x 35 mm /140 g	110 mm x 56 mm x 25 mm / 80 g
Price	USD 7.00	USD 99.00

2.3 Measurement and Analysis of the Output

In this work, experimental measurements are conducted between 11.00 am to 2.00 pm on two consecutive days. Although the light intensities and incident angles on the solar panel differs within this time range, the efficiency analysis of the charge controllers still hold true since it is computed based on normalised values of solar irradiance.

Several output parameters were measured in order to analyse the performance of the solar-powered UAV system. These parameters are as follows:

a. Open-circuit voltage (V_{oc})
b. Short-circuit current (I_{sc})
c. Voltage at maximum power point (V_{mpp})
d. Current at maximum power point (I_{mpp})
e. Maximum power (P_{mpp})

The following equation shows the calculation of the efficiency of the solar-powered UAV system (Karthik Reddy & Poondla, 2017):

$$\text{Efficiency} = \frac{\text{Current } (I) \times \text{Voltage } (V)}{\text{Solar irradiance } \left(\frac{W}{m^2}\right) \times \text{Surface Area } (m^2)} \quad (1)$$

The maximum power can be determined using the following equation, whereby the current and voltage at a maximum point are used:

$$P_{mpp} = I_{mpp} \times V_{mpp} \quad (2)$$

where P_{mpp} is the maximum power, I_{mpp} is the current maximum power and V_{mpp} is the voltage maximum power. The V_{mpp}, I_{mpp}, and P_{mpp} values can be determined after the solar panels are connected to the charge controller, battery and loads respectively. The maximum voltage (V_{mpp}) of the solar panels can be determined using a multimeter. The difference in values from the previous data is expected due to the connection with both the charge controller and battery. The load resistors consist of 0.1, 1.5, 4.6, 7.1, 18, 25.5 and 61.1 Ω.

3. RESULTS AND DISCUSSION

3.1 Open Circuit Voltage and Short Circuit Current

The open circuit voltage (V_{oc}) and short circuit current (I_{sc}) of the solar panels were measured to determine the actual maximum voltage and current output from the solar panel. The V_{oc} measurement was performed by disconnecting the solar panel's positive and negative load terminal while measuring the voltage at the terminals. The light intensity needed to be above 1,000 W/m^2 during the measurement in order to achieve the nominal working voltage of the solar panel. A solar irradiance meter, sometimes referred to as a pyranometer, was used to measure solar radiation flux density, W/m^2 (Njok *et al*., 2020).

As the solar irradiance recorded was higher than 1,000 W/m^2, the open circuit voltage value was taken using a multimeter and the values were recorded as V_{oc}. The average value of the measured V_{oc} was recorded with different light intensities and at different light incidence angles. Based on Table 3, the average V_{oc} value recorded was 21.43 V. However, the factory specification of the V_{oc} was slightly higher, which was 22.4 V for 40 solar cells connected in series.

Table 3: Voltage open circuit (V_{oc}) values for three different solar irradiances.

Time	Voltage, V	Solar irradiance, W/m^2
12.00 pm	21.35	1,119.30
1.00 pm	20.33	1,015.00
2.00 pm	22.62	1,224.20

As for the measurement of I_{sc}, the solar panel's positive and negative terminals were shorted together to produce a maximum current. The total current flow was measured using a digital clamp meter.
Table 4 shows the I_{sc} data collected at different times with different solar irradiance values. Based on this data, the average value of I_{sc} is 1.61 A, which is similar to the factory specifications of the solar cell.

Table 4: I_{sc} values for three different solar irradiances.

Time	Current, A	Solar irradiance, W/m^2
12.00 pm	1.543	1,015.20
1.00 pm	1.653	1,200.70
2.00 pm	1.632	1,059.40

3.2 Solar Cell Output Validation

In order to determine the actual output power of the solar panel, different values of resistive load were connected to the solar panel. The power output was calculated using the measured parameters as shown in Table 5. Each solar cell has size of 0.156 m x 0.0312 m = 0.004867 m^2. The total area of 40 solar cells is 40 x 0.004867 m^2 = 0.19469 m^2. As the rated specification of each of the solar cell is 0.8 W, 40 solar cells should produce maximum power of 32 W.

Table 5: Measurement of solar panel performance.

Load, Ω	Solar irradiance, W/m^2	Voltage, V	Current, A	Power, W	Solar cell efficiency, %
0.1	1,279.50	0.53	1.59	0.843	0.3
1.5	1,177.20	2.44	1.47	3.587	1.6
4.6	1,021.60	5.66	1.33	7.528	3.8
7.1	1,018.60	8.00	1.26	10.080	5.1
18.0	1,008.13	15.3	0.95	14.535	7.4
25.5	1,110.80	18.50	0.84	15.540	7.2
61.1	1,287.50	19.83	0.35	6.941	2.8

From the data in Table 5, it is found that the peak power generated from the solar panel occurred when the load resistance was 25.5 **Ω**, which produced 15.54 W. The output power started to drop when the resistance was increased above this value. That is because the larger the resistor, the more energy is used by the resistor and the more significant the voltage drop across that resistor. It is also found that using load resistance of 18 **Ω**, even with lower light intensity, the solar panels could produce slightly higher efficiency at 7.4 %.

3.3 Solar Powered UAV System Efficiency

The efficiency of the photovoltaic system was obtained by measuring the output power from the solar panel, load and battery. The total output power is equal to the summation of power from solar panel and batteries. As the load draws energy, the solar panel's energy is utilised and starts to recharge the battery. The battery will be used when the solar panel's potential difference is low due to the absence of sunlight. The measurement data for both types of solar charge controllers are recorded in Table 6 and Table 7, which consist of the maximum voltage (V_{mpp}) and maximum current (I_{mpp}) of each terminal (solar panel, battery and load).

Table 6 shows the results of the experiment conducted for the PWM charge controller. The lowest solar irradiance was reported at 11.00 am with value of 1,033 W/m^2, while the highest reported was at 1.00 pm with value of 1,221 W/m^2. On the other hand, the MPPT charge controller results are shown in Table 7. The lowest solar irradiance for the MPPT was reported at 11.00 am with value of 1,145 W/m^2, while the highest was reported at 12.00 pm with value of 1,326 W/m^2. Solar irradiance values were not consistent despite measurements are taken at the same time on different days due to differences in clouds covering the sky.

Table 6: Data of V_{mpp} and I_{mpp} for the PWM charge controller.

Time	Solar Irradiance, W/m^2	V_{mpp}, V (Solar)	I_{mpp}, A (Solar)	V_{mpp}, V (Battery)	I_{mpp}, A (Battery)	V_{mpp}, V (Load)	I_{mpp}, A (Load)
11.00 am	1,033	12.21	0.591	12.21	0.443	12.62	0.987
12.00 pm	1,093	12.36	0.682	12.58	0.450	12.93	1.056
1.00 pm	1,221	13.32	0.843	13.37	0.431	13.40	1.187
2.00 pm	1,210	13.24	0.786	13.51	0.426	13.53	1.126

Table 7: Data of V_{mpp} and I_{mpp} for the MPPT charge controller.

Time	Solar Irradiance, W/m^2	V_{mpp}, V (Solar)	I_{mpp}, A (Solar	V_{mpp}, V (Battery)	I_{mpp}, A (Battery)	V_{mpp}, V (Load)	I_{mpp}, A (Load)
11.00 am	1,145	16.42	0.870	15.90	0.120	16.02	0.967
12.00 pm	1,326	16.75	0.868	14.91	0.170	16.98	1.050
1.00 pm	1,203	16.18	0.876	15.68	0.168	16.40	1.056
2.00 pm	1,244	16.05	0.906	14.91	0.170	16.23	1.082

Tables 8 and 9 show the maximum output power and corresponding power losses for the PWM and MPPT charge controllers respectively. The maximum power losses in these tables were obtained by subtracting the input power (which is the power generated by the solar panel and battery) from the output power of the load.

Based on Table 8, the maximum power obtained from the solar panel using the PWM charge controller varied from 7.216 to 11.229 W as the solar irradiance varied from 1,033 to 1,221 W/m^2. This resulted in variation of maximum power losses reaching up to 1.085 W when the solar irradiance was 1,221 W/m^2.

Table 8: Maximum output power using the PWM charge controller.

Solar Irradiance, W/m^2	Maximum Power (Solar), W	Maximum Power (Battery), W	Input power (Solar + Battery), W	Output power, (Load), W	Maximum power losses, W
1,033	7.216	5.409	12.625	12.456	0.169
1,093	8.429	5.661	14.090	13.654	0.436
1,210	10.407	5.755	16.162	15.235	0.927
1,221	11.229	5.762	16.991	15.906	1.085

On the other hand, based on Table 9, the maximum power obtained from the solar panel using the MPPT charge controller was within 14.17 to 14.54 W. When the MPPT charge controller was used, it could be seen that the maximum power losses only reached up to 0.76 W. This shows that the MPPT charge controller results in relatively smaller losses as compared to the PWM charge controller.

Table 9: Maximum output power using the MPPT charge controller.

Solar Irradiance, W/m^2	Maximum Power (Solar), W	Maximum Power (Battery), W	Input power (Solar + Battery), W	Output power, (Load), W	Maximum power losses, W
1,145	14.28	1.91	16.19	15.49	0.26
1,203	14.17	2.63	16.80	17.32	0.52
1,244	14.54	2.50	17.04	17.60	0.56
1,326	14.54	2.53	17.07	17.83	0.76

Based on Tables 8 and 9, for both charge controllers, as the solar irradiance increases, the power loss is shown to increase accordingly. The losses may be caused by higher temperature exposed to the solar panels as compared to the factory test conditions (De Rose *et al*., 2019). Another reason for the lower power output might be due to cracked or broken solar cells (Gierth *et al*., 2012).

Tables 10 and 11 show the energy conversion efficiency of the solar-powered UAV system for both types of charge controllers calculated using Equation 1. Based on Table 10, the solar-powered UAV's energy conversion efficiency with the PWM charge controller varied from 6.19 to 6.69%. Meanwhile, based on Table 11, the solar-powered UAV's efficiency with the MPPT charge controller was between 6.91 to 7.40%. The two different types of charge controllers showed that the maximum efficiency was achieved at 1.00 pm. However, the MPPT charge controller was able to produce slightly higher efficiency than the PWM charge controller at this time despite the measured solar irradiance being lower compared to when the PWM charge controller was being used.

Table 10: Efficiency of solar-powered UAV using PWM charge controller.

Time	Solar irradiance, W/m^2	Energy conversion efficiency, %
11.00 am	1,033	6.19
12.00 pm	1,093	6.42
1.00 pm	1,221	6.69
2.00 pm	1,210	6.47

Table 11: Efficiency of solar-powered UAV using MPPT charge controller.

Time	Solar irradiance, W/m^2	Energy conversion efficiency, %
11.00 am	1,145	6.95
12.00 pm	1,326	6.91
1.00 pm	1,203	7.40
2.00 pm	1,244	7.27

Based on the results obtained, the solar panel's actual energy conversion efficiency is slightly lower than the factory specification. This is due to several factors, including the imperfect connection of the solar panel. The connectivity of each solar cell must be checked after being soldered. The tabbing wire must be attached correctly to the solar cell terminal to avoid any loss of power. Next, the solar panel must be encapsulated to avoid any damage to the solar panel itself. The solar panel's encapsulation must be done using epoxy resin to ensure the maximum solar irradiance captured by the solar panel can pass through the encapsulate material efficiently (Sahwee *et al*., 2019).

Figures 7 and 8 show the plot of efficiency against solar irradiance when using PWM and MPPT as the charge controller respectively. Comparison of these graphs shows that the efficiency of the solar panel when using the MPPT charge controller was higher as compared to when using the PWM charge controller. This is because MPPT has the ability to auto-switch the charging based on solar irradiance conditions. Thus, the system is more efficient as compared to the technology used in PWM.

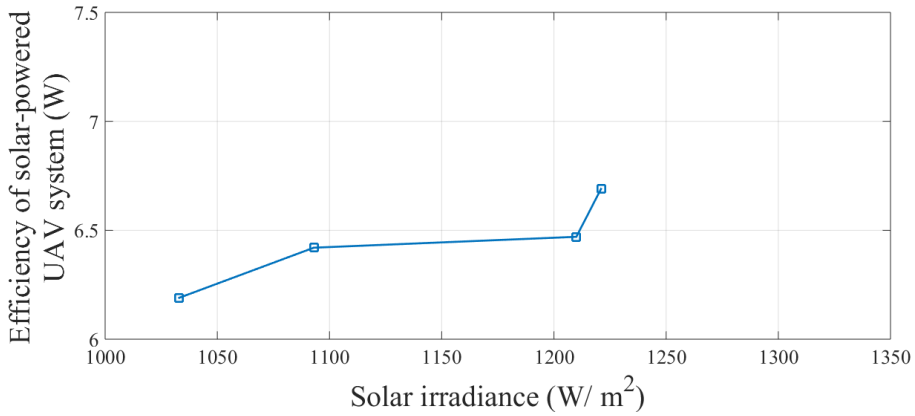

Figure 7: Efficiency using the PWM charge controller.

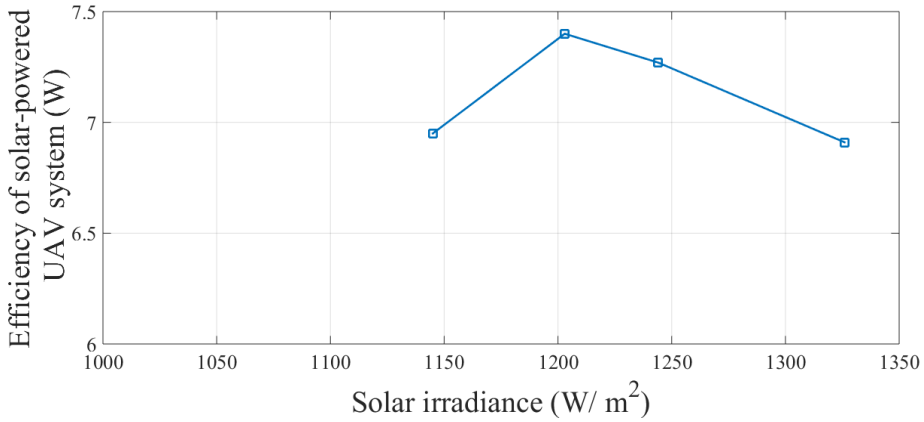

Figure 8: Efficiency using the MPPT charge controller.

The results obtained for both type of charge controllers are comparable although a slightly higher efficiency was observed when using the MPPT charge controller. Figure 9 shows the data of the solar panel characteristics when connected to a variable resistive load while connected to the MPPT charge controller. This data verifies that the MPPT charge controller was able to track the maximum power output of the solar panel and thus provide higher efficiency.

MPPT charge controllers are well known to be more efficient as compared to PWM charge controllers, given that the operating conditions are satisfied, which includes high solar irradiance and low temperature. However, for low power applications, due to the lower complexity and cost of PWM, it is better suited as compared to MPPT. For high power applications, which can take advantage of a larger solar panel arrays, MPPT would be a better option (Grubss, 2019).

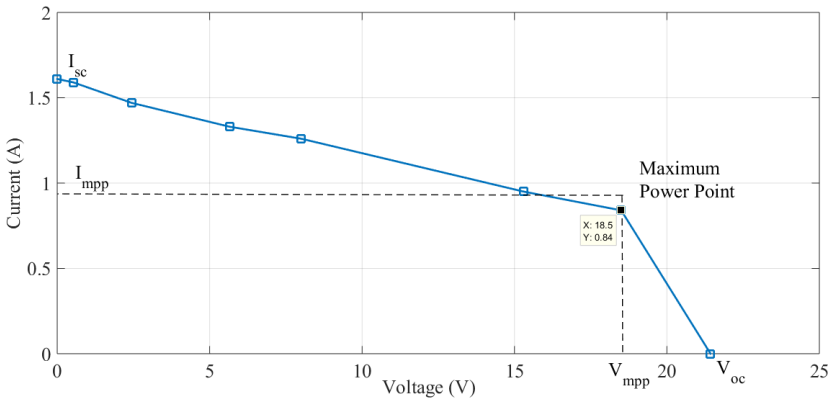

Figure 9: The performance of the MPPT charge controller in tracking the maximum power output.

4. CONCLUSION

This research provided a performance comparison between PWM and MPPT charge controllers used in solar UAV applications. The result showed that the MPPT charge controller provided better efficiency for the entire system as compared to the PWM charge controller. Based on the results obtained, the MPPT charge controller has 1% higher efficiency as compared to the PWM charge controller. That is because the MPPT solar charge controller was able to extract the maximum power from the solar panel regardless of the solar irradiance conditions. It was also found that the output voltage can be maintained as long as the voltage from the solar panel is within its operating range. Further studies on high power applications, which covers up to the maximum rated current of PWM or MPPT is needed to analyse the performance of both charge controllers.

REFERENCES

Chatta, M.B, Hafiz, M.A, Muzaffar, A. & Muhammad, A.B. (2018). Experimental investigation of monocrystalline and polycrystalline solar modules at different inclination angles. *J. Therm. Eng.*, **4**: 2137–2148.

Energysage (2019). *Monocrystalline and Polycrystalline Solar Panels: What You Need to Know. (SunShot).* Available online at https://www.energysage.com/solar/101/monocrystalline-vs-polycrystalline-solar-panels/ (Last access date: 3 March 2020).

Gierth, P., Rebenklau, L. & Michaelis, A. (2012). Evaluation of soldering processes for high efficiency solar cells. *Proc. Int. Spring Sem. Electron. Tech.*, 9-13 May 2012, Austria, pp. 133–137.

Grubss, D. (2019). *How to Select a Solar Charge Controller for Your PV System*. Available online at: https://www.solarpowerworldonline.com/2019/12/how-to-select-a-solar-charge-controller (Last access date: 6 July 2021).

Karthik Reddy, B.S. & Poondla, A. (2017). Performance analysis of solar powered unmanned aerial vehicle. *Renew. Ener.*, **104**, 20–29.

Liu, A. (2015) *Energy-Optimal Flight of a Solar-Assisted Unmanned Aerial Vehicle*, Master Thesis, Department of Aerospace Engineering, University of Toronto, Toronto.

Majaw, T., Deka, R., Roy, S. & Goswami, B. (2018). Solar charge controllers using MPPT and PWM: A review. *ADBU J. Electric. Electron. Eng.*, **2***:* 1-4.

Oo, N., Lwin, K.S. & Tun, H.M. (2016). A charge controller design for solar power system, *Int. J. S&T Research*, 76-79.

Njok, A.O., Kamgba, F.A., Panjwani, M.K. & Mangi, F.H. (2020). The influence of solar power and solar flux on the efficiency of polycrystalline photovoltaics installed close to a river. *Indones. J. Electric. Eng. Comp. Sci.*, **17**: 988-996.

De Rose, A., Geipel, T., Eberlein, D., Kraft, A. & Nowottnick, M. (2019). Interconnection of silicon heterojunction solar cells by infrared soldering - solder joint analysis and temperature study. *36th Eur. PV Solar Ener. Conf. Exh.*, pp. 9–13.

Sahwee, Z., Abdul Hamid, S., Mohd Kamal, N.L. & Norhashim, N. (2019). Experimental evaluation of encapsulated solar cells for unmanned aerial vehicle application. *2019 IEEE Int. Conf. Aero. Electron. Remote Sens. Tech. (ICARES 2019)*, pp. 1-4

Sendy, A. (2021). *What are the Pros and Cons of Monocrystalline, Polycrystalline and Thin Film Solar Panels? (SolarReviews)*. Available online at: https://www.solarreviews.com/blog/pros-and-cons-of-monocrystalline-vs-polycrystalline-solar-panels (Last access date: 8 March 2020)

Mora, S., Basilio, S., Paipa, E.A.L., Serrano, M.A.L. & Márquez, L.F.B. (2019). Performance comparison between PWM and MPPT charge controllers. *Sci. Tech.* Año, **24**: 6-11.

Svarc, J. (2020). *MPPT vs PWM Solar Charge Controllers*. Available online at: https://www. cleanenergyreviews. info/ blog/mppt-solar-charge-controllers (Last access date: 2 March 2021)

Thipyopas, C., Sripawadkul, V. & Warin, N. (2019). Design and development of a small solar-powered UAV for environmental monitoring application. *2019 IEEE Eurasia Conf. IOT, Comm. Eng. (ECICE2019)*, 316–319.

Turk, I., Yazar, I.B., Filik, U. & Karakoc, T.H. (2018). Simulation based mathematical model of a solar powered DC motor for UAV applications. 7th *Global Conf. Global Warming (GCGW-2018)*, 24-28 June 2018, Turkey.

Yilmaz, U., Kircay, A. & Borekci, S. (2017). PV system fuzzy logic MPPT method and PI control as a charge controller. *Renew. Sust. Ener. Rev.*, **81**: 994–1001.

EVALUATION OF ACCURACY OF GLOBAL POSITIONING SYSTEM (GPS) RECEIVERS

Dinesh Sathyamoorthy

Science & Technology Research Institute for Defence (STRIDE), Ministry of Defence, Malaysia

Email: dinesh.sathyamoorthy@stride.gov.my

ABSTRACT

In this study, Global Positioning System (GPS) simulation is used to evaluate the accuracy of GPS receivers. The study is conducted for two scenarios: 1) Open area scenario with full range of available GPS satellites; 2) obstructed area scenario with only four GPS satellites with the highest elevations. Three GPS receivers are used for the study: 1) R1: Garmin GPSmap 78s receiver; 2) R2: GM1-86UB receiver that uses a u-blox 6 GPS chipset; 3) R3: VK-172 receiver that uses a u-blox 7 GPS chipset. It is found that with decreasing GPS signal power level, position errors increase due to decreasing carrier-to-noise density (C/N_0) levels for GPS satellites tracked by the receiver, which is the ratio of received GPS signal power level to noise density. For the obstructed area scenario, the position errors increase due to reduced availability of GPS satellites. In addition, varying position error patterns are observed for the each of the readings. This is due to the GPS satellite constellation being dynamic, causing varying GPS satellite geometry over location and time, resulting in GPS accuracy being location / time dependent It is found that the R3 receiver provided the lowest position errors for both the open area and obstruction area scenarios due to it having higher receiver sensitivity and lower receiver noise, which allows it track higher C/N_0 levels for the available GPS satellites.

Keywords: *Global Positioning System (GPS) simulation; open and obstructed area scenarios; position errors; GPS signal power level; GPS satellite geometry.*

1. INTRODUCTION

With Global Navigation Satellite Systems (GNSS) being widely used for various applications, the evaluation of accuracy of GNSS receivers has received increasing attention (McMinn *et al*., 2012; Zhang *et al*., 2014; Yanchuk *et al*., 2017; Rychlicki *et al*., 2020). Ensuring high accuracy of GNSS receivers is important in ensuring effective and safe operation in fields such as navigation, agriculture and public safety & disaster relief. Low accuracy of GNSS receivers can lead to hazardous situations (Laskowski *et al*., 2015; Hadavi *et al*., 2018; Rychlicki *et al*., 2020).

In this study, Global Positioning System (GPS) simulation is used to evaluate the accuracy of GPS receivers. GPS simulation allows for the tests to be conducted with various repeatable conditions, as defined by the users. As the tests are conducted in controlled laboratory environments, they are not be inhibited by unintended signal interferences and obstructions (Aloi *et al*., 2007; Kou & Zhang, 2011; Pozzobon *et al*., 2013; Arul Elango & Sudha, 2016). In our previous studies, GPS simulation was used to evaluate the vulnerabilities of GPS to radio frequency interference (RFI) (Dinesh *et al*., 2012a, 2017a, 2020), multipath (Dinesh *et al*., 2013, 2014), GPS satellite clock error (Dinesh *et al*., 2015a, 2019), varying speeds (Dinesh *et al*., 2015b), power consumption (Dinesh *et al*., 2016) and GPS antenna orientation (Dinesh *et al*., 2017b).

In a previous study, Dinesh *et al*. (2012b) employed GPS simulation to evaluate the accuracy of GPS receivers using probable error, which a measure of uncertainties of the positions solution based on

dilution of precision (DOP) and user equivalent ranging error (UERE) (DOD, 2001; USACE, 2011; Kaplan & Hegarty, 2017). However, a number of GPS receivers do not provide probable error readouts. Furthermore, the study was only conducted for open area scenario with full range of available GPS satellites. In actual practice, GPS receivers are often used in conditions of obstruction that limit the number of available satellites, such as in built up areas and forests.

To this end, for this study, GPS accuracy is evaluated using position error, which is the distance between the position of a location determined by the GPS receiver and the actual position. The study is conducted for two scenarios: 1) Open area scenario with full range of available GPS satellites; 2) obstructed area scenario with only four GPS satellites with the highest elevations.

Three GPS receivers are used for the study: 1) R1: Garmin GPSmap 78s receiver (Garmin, 2010); 2) R2: GM1-86UB receiver that uses a u-blox 6 GPS chipset (u-blox, 2011); 3) R3: VK-172 receiver that uses a u-blox 7 GPS chipset (u-blox, 2014). All three GPS receivers employ the GPS L1 coarse acquisition (C/A) signal, which is an unencrypted civilian GPS signal widely used by various GPS receivers. The signal has a fundamental frequency of 1,575.42 MHz and a code structure which modulates the signal over a 2 MHz bandwidth (DOD, 2001; USACE, 2011; Kaplan & Hegarty, 2017).

2. METHODOLOGY

The apparatus used in the study are an Aeroflex GPSG-1000 GPS simulator (Aeroflex, 2010) and a notebook running GPS Diagnostics v1.05 (CNET, 2004) The study is conducted in STRIDE's mini-anechoic chamber (Kamarulzaman, 2010) to avoid external interference signals and unintended multipath errors. The test setup employed is as shown in Figure 1. Simulated GPS signals are generated using the GPS simulator and transmitted via the coupler. The following assumptions are made for the tests conducted:

i) No ionospheric or troposheric delays
ii) Zero unintended GPS satellite clock or ephemeris error
iii) No obstructions or multipath
iv) No interference signals.

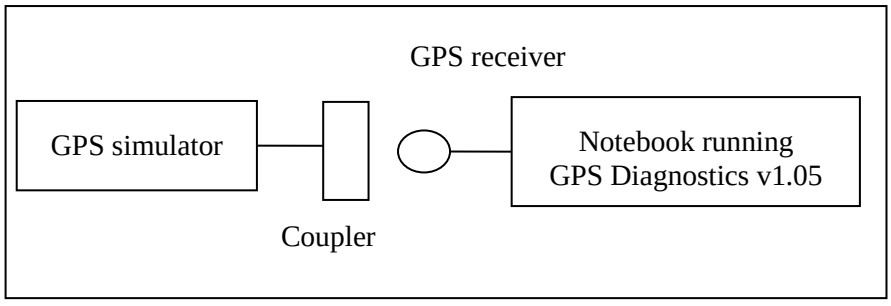

Figure 1: The test setup employed.

The tests are conducted for coordinated universal time (UTC) times of 0000, 0300, 0600 and 0900, with the location set at Teluk Intan, Perak (N 2° E 101°, 0 m). The almanac data for the periods is downloaded from the US Coast Guard's web site (USCG, 2021) and imported into the GPS simulator.

For each test, transmission is started at GPS signal power level of -130 dBm and reduced to -180 dBm at decrements of 5 dBm and intervals of 5 min. At each power level, the GPS receiver's position error is recorded.

3. RESULTS & DISCUSSION

For the tests conducted, the recorded position errors are shown in Figures 2-3. With decreasing GPS signal power level, position errors increase due to decreasing carrier-to-noise density (C/N_0) levels for GPS satellites tracked by the receiver, which is the ratio of received GPS signal power level to noise density. Lower C/N_0 levels result in increased data bit error rate when extracting navigation data from GPS signals, and hence, increased carrier and code tracking loop jitter. This, in turn, results in more noisy range measurements and thus, less precise positioning (DOD, 2001; Petovello, 2009; USACE, 2011; Kaplan & Hegarty, 2017). In addition, for the obstructed area scenario, the position errors increase due to reduced availability of GPS satellites.

It is found that the R3 receiver provided the lowest position errors for both the open area and obstruction area scenarios due to it having higher receiver sensitivity and lower receiver noise, which allows it track higher C/N_0 levels for the available GPS satellites.

Varying position error patterns are observed for the each of the readings. This is due to the GPS satellite constellation being dynamic, causing varying GPS satellite geometry over location and time, resulting in GPS accuracy being location / time dependent (DOD, 2001; Huihui *et al.*, 2008; Dinesh *et al.*, 2010; USACE, 2011; Kaplan & Hegarty, 2017).

It should be noted that the tests conducted in this study were for only three GPS receivers. Additional tests using a wider range of GPS receivers are needed to further validate the findings of this study. Furthermore, a limitation faced in this study was that the GPS simulator used only allows the transmission of the GPS L1 C/A signal. The proposed future work is for the procurement of a GNSS simulator that will allow transmission of other GPS signals, in particular L2C and L5, along with signals of other GNSS systems (GLONASS, BeiDou and Galileo).

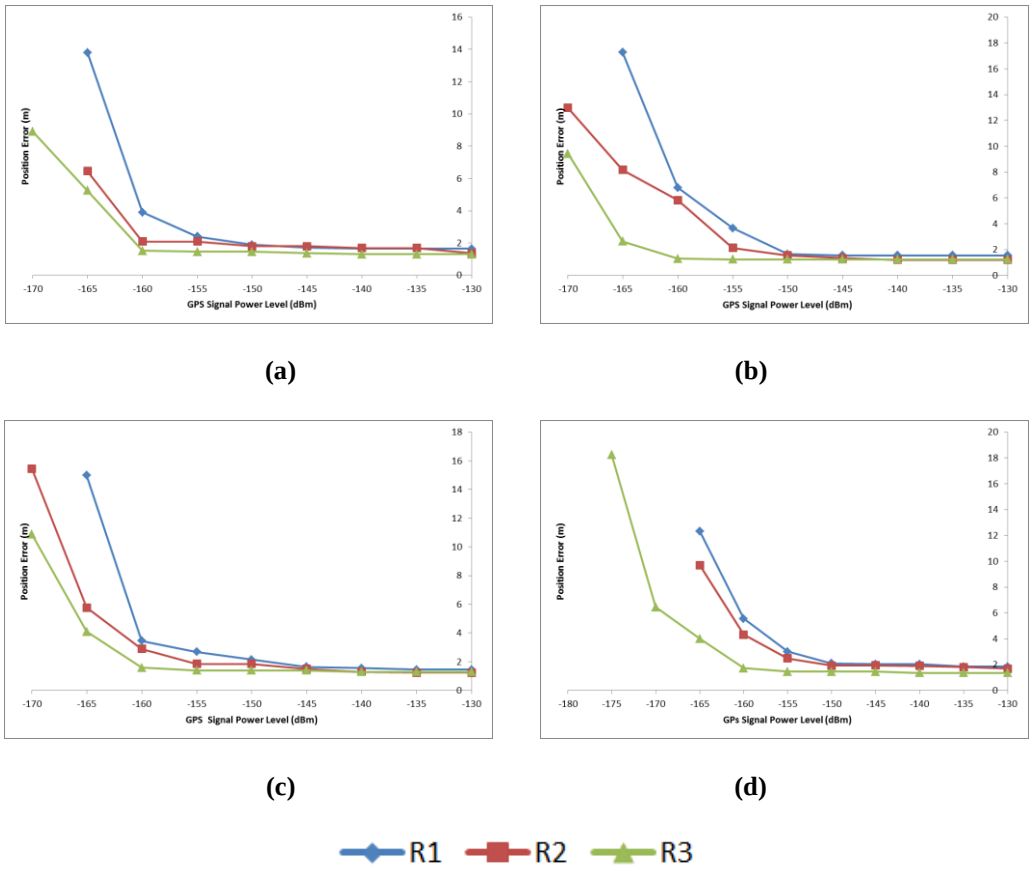

Figure 2: Recorded position errors for the open area scenario for UTC times of: (a) 0000 (b) 0300 (c) 0600 (d) 0900.

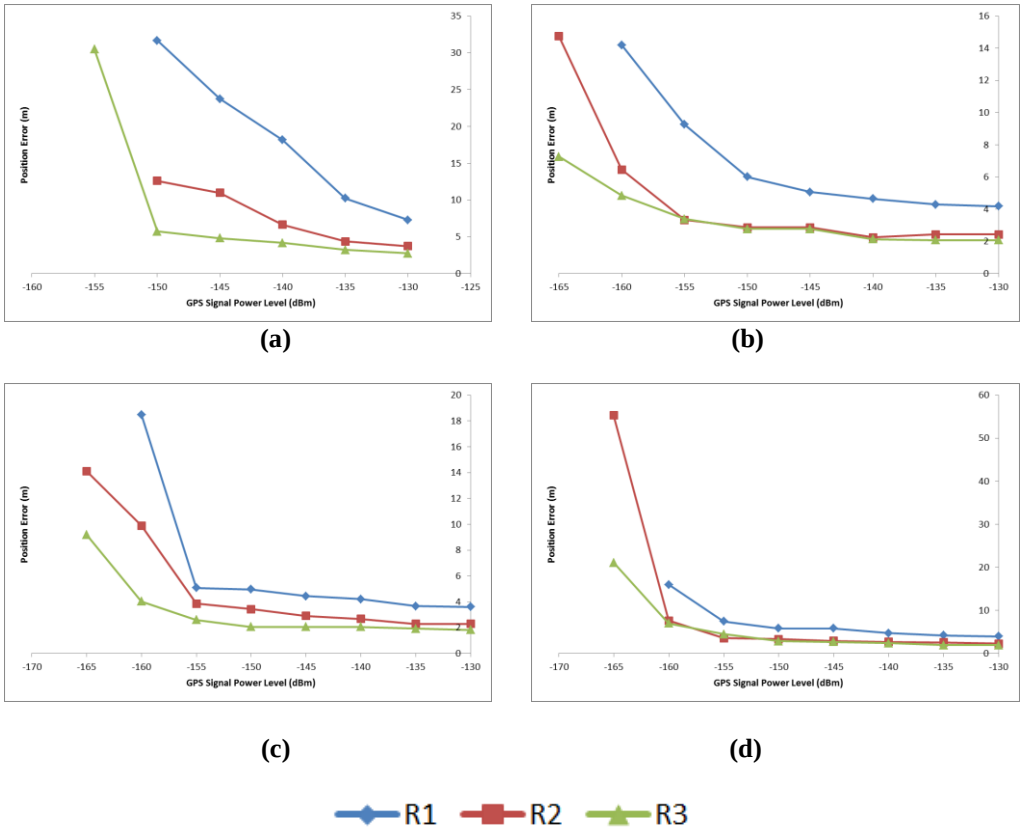

Figure 3: Recorded position errors for the obstructed area scenario for UTC times of: (a) 0000 (b) 0300 (c) 0600 (d) 0900.

4. CONCLUSION

From this study, it was found that with decreasing GPS signal power level, position errors increase due to decreasing C/N_0 levels for GPS satellites tracked by the receiver, which is the ratio of received GPS signal power level to noise density. For the obstructed area scenario, the position errors increased due to reduced availability of GPS satellites. In addition, varying position error patterns were observed for the each of the readings. This is due to the GPS satellite constellation being dynamic, causing varying GPS satellite geometry over location and time, resulting in GPS accuracy being location / time dependent It was found that the R3 receiver provided the lowest position errors for both the open area and obstruction area scenarios due to it having higher receiver sensitivity and lower receiver noise, which allows it track higher C/N_0 levels for the available GPS satellites.

REFERENCES

Aeroflex (2010). *Avionics GPSG-1000 GPS / Galileo Portable Positional Simulator*. Aeroflex Inc., Plainview, New York.

Aloi, D.N., Alsliety, M. & Akos, D.M. (2007). A methodology for the evaluation of a GPS receiver performance in telematics applications. *IEEE T. Instrum. Meas.*, **56**: 11-24.

Arul Elango, G. & Sudha, G.F. (2016). Design of complete software GPS signal simulator with low complexity and precise multipath channel model. *J. Electr. Syst., Inform. Tech.*, **3**: 161-180.

CNET (2004). *GPSDiag 1.0*. Available online at: http://download.cnet.com/GPSDiag/3000-2130_4-4951103.html (Last access date: 19 April 2021).

Dinesh, S., Wan Mustafa, W.H., Mohd Faudzi, M., Kamarulzaman, M., Hasniza, H., Nor Irza Shakhira, B., Siti Robiah, A., Shalini, S., Jamilah, J., Aliah, I., Lim, B.T., Zainal Fitry, M.A.,

Mohd Rizal, A.K., Azlina, B. & Mohd Hasrol, H.M.Y. (2010). Evaluation of the effect of radio frequency interference (RFI) on Global Positioning System (GPS) accuracy. *Defence S&T Tech. Bull.*, **3**: 100-118.

Dinesh, S, Mohd Faudzi, M. & Zainal Fitry, M.A. (2012a). Evaluation of the effect of radio frequency interference (RFI) on Global Positioning System (GPS) accuracy via GPS simulation. *Defence. Sci. J.*, **62**: 338-347.

Dinesh, S., Mohd Faudzi., M., Rafidah, M., Nor Irza Shakhira, B., Siti Robiah, A., Shalini, S., Aliah, I., Lim, B.T., Zainal Fitry, M.A., Mohd. Rizal, A.K., & Mohd Hasrol, H.M.Y. (2012b). Evaluation of the effect of varying Global Positioning System (GPS) signal power levels on GPS accuracy. *Defence S&T Tech. Bull.*, **5**: 57-71.

Dinesh, S., Shalini, S., Zainal Fitry, M.A. & Siti Zainun, A. (2013). Evaluation of the repeatability of Global Positioning System (GPS) performance with respect to GPS satellite orbital passes. *Defence S&T Tech. Bull.*, **6**: 130-140.

Dinesh, S., Shalini, S., Zainal Fitry, M.A., Siti Zainun, A., Siti Robiah, A., Mohd Idris, I. & Mohd Hasrol Hisam, M.Y. (2014). Evaluation of the effect of commonly used materials on multipath propagation of Global Positioning System (GPS) signals via GPS simulation. *Adv. Mil. Tech.*, **9**: 81-95.

Dinesh, S., Shalini, S., Zainal Fitry, M.A., Asmariah, J. & Siti Zainun, A. (2015a). Evaluation of the effect of Global Positioning System (GPS) satellite clock error via GPS simulation. *Defence S&T Tech. Bull.*, **8**: 51-62.

Dinesh, S., Shalini, S., Zainal Fitry, M.A., Asmariah, J. & Siti Zainun, A. (2015b). Evaluation of the accuracy of Global Positioning System (GPS) speed measurement via GPS simulation. *Defence S&T Tech. Bull.*, **8**: 121-128.

Dinesh, S., Shalini, S., Zainal Fitry, M.A., Asmariah, J. & Siti Zainun, A. (2016). Evaluation of trade-off between Global Positioning System (GPS) accuracy and power saving from reduction of number of GPS receiver channels. Appl. Geomatics, **8**: 67-75.

Dinesh, S., Zainal Fitry, M.A. & Shahrudin, A.H. (2017a). Evaluation of Global Positioning System (GPS) adjacent band compatibility via GPS simulation. *Defence S&T Tech. Bull.*, **10**: 229 – 235.

Dinesh, S., Shalini, S., Zainal Fitry, M.A., Mohamad Firdaus, A., Asmariah, J. & Siti Zainun, A. (2017b). Evaluation of the effect of Global Positioning System (GPS) antenna orientation on GPS performance. *Defence S&T Tech. Bull.*, **10**: 33-39.

Dinesh, S., Zainal Fitry, M.A & Esa, S. (2019). Evaluation of the effectiveness of receiver autonomous integrity monitoring (RAIM) in Global Positioning System (GPS) receivers. *Defence S&T Tech. Bull.*, **12**: 295-300.

Dinesh, S., Zainal Fitry, M.A, Esa, S.,Shahrudin, E.S., Ahmad Firdaus, A.K & Zaherudin, Z. (2020). Evaluation of the vulnerabilities of unmanned aerial vehicles (UAVs) to Global Positioning System (GPS) jamming and spoofing. *Defence S&T Tech. Bull.*, **13**: 333-343.

DOD (Department of Defence) (2001). *Global Positioning System Standard Positioning Service Performance Standard, Command, Control, Communications, and Intelligence*. Department of Defence (DOD), Washington D.C.

Eastlack, H. (2004). *SVN-23/PRN-23 Integrity Failure of 1 January 2004*. Second Space Operations Squadron, US Air Force, Washington, D.C.

Garmin (2010). *GPSmap 78s Owner's Manual*. Garmin International Inc., Olathe, Kansas.

Hadavi, S., Verlinde, S., Verbeke,W., Macharis, C. & Guns, T. (2018). Monitoring urban-freight transport based on GPS trajectories of heavy-goods vehicles. *IEEE Trans. Intell. Transp. Syst.*, **20**: 3747–3758.

Huihui, W., Xingqun, Z. & Yanhua, Z. (2008). Geometric dilution of precision for GPS single-point positioning based on four satellites. *J. Syst. Eng. Electr.*, **19**: 1058-1063.

Kamarulzaman, M. (2010). *Technical Specification for STRIDE's Mini-Anechoic Chamber*. Science & Technology Research Institute for Defence (STRIDE), Ministry of Defence, Malaysia.

Kaplan, E.D. & Hegarty, C.J. (2017). *Understanding GPS / GNSS: Principles and Applications*. Artech House, Norwood, Massachusetts.

Kou, Y. & Zhang, H. (2011). Verification testing of a multi-GNSS RF signal simulator. *Inside GNSS*, **6**: 52-61.

Lavraks, J.W. (2005). *An Overview of Civil GPS Monitoring.* Institute of Navigation (ION), Manassas, Virginia.

Laskowski, D., Lubkowski, P., Pawlak, E. & Stanczyk, P. (2015). Anthropotechnical systems reliability. *Proc. Eur. Safety Reliability Conf.*, 7-10 September 2015, Zurich, Switzerland, pp. 399–407.

McMinn, D., Row, D.A. & Cuk, I. (2012). Evaluation of the Trackstick™ Super GPS Tracker for use in walking research. *Res. Q. Exer. Sport.* **83**: 108-113.

Ober P.B. (2003). *Integrity Prediction and Monitoring of Navigation Systems*. Integricom Publishers, Leiden, Netherlands.

Petovello, M. (2009). Carrier-to-noise density and AI for INS / GPS integration. *Inside GNSS*, **4:** 20-29.

Pozzobon, O., Sarto, C., Chiara, A.D., Pozzobon, A., Gamba, G., Crisci, M. & Ioannides, R. (2013). Developing a GNSS position and timing authentication testbed: GNSS vulnerability and mitigation techniques. *Inside GNSS*, **8**: 45-53.

Rychlicki, M., Kasprzyk, Z. & Rosinski, A. (2020). Analysis of accuracy and reliability of different types of GPS receivers. *Sensors*, **20**: 6498.

u-blox (2011). *u-blox 6 GPS Modules*. u-blox, Thalwil, Switzerland.

u-blox (2014). *u-blox 7 GPS Modules*. u-blox, Thalwil, Switzerland.

USACE (US Army Corps of Engineers) (2011). *Engineer Manual EM 1110-1-1003: NAVSTAR Global Positioning System Surveying.* US Army Corps of Engineers (USACE), Washington D.C.

USCG (US Coast Guard) (2018). *GPS NANUs, Almanacs, & Ops Advisories*. Available online at: http://www.navcen.uscg.gov/?pageName=gpsAlmanacs (Last access date: 19 April 2021).

Yanchuk, O., Roman, S., Dets, T. & Struk, S. (2017). Evaluation of GPS observations accuracy within limited visibility basing on empiric data. *Geodesy Cartogr.*, **43**: 105-110.

Zhang, H., Zheng, J., Dorr, G., Zhou,H. & Ge., Y. (2014). Testing of GPS accuracy for precision forestry applications. *Earth Sci.*, **39**: 237-245.